12-1-2017

Design and Construction of a High-Current Femtosecond Gas-Phase Electron Diffraction Setup

Omid Zandi
University of Nebraska-Lincoln, omid.zandi@huskers.unl.edu

Zandi, Omid, "Design and Construction of a High-Current Femtosecond Gas-Phase Electron Diffraction Setup" (2017). *Theses, Dissertations, and Student Research: Department of Physics and Astronomy*. 40.
http://digitalcommons.unl.edu/physicsdiss/40

DESIGN AND CONSTRUCTION OF A HIGH-CURRENT FEMTOSECOND GAS-PHASE ELECTRON DIFFRACTION SETUP

by

Omid Zandi

A DISSERTATION

Presented to the Faculty of
The Graduate College at the University of Nebraska
In Partial Fulfillment of Requirements
For the Degree of Doctor of Philosophy

Major: Physics and Astronomy

Under the Supervision of Professor Martin Centurion

Lincoln, Nebraska

November, 2017

DESIGN AND CONSTRUCTION OF A HIGH-CURRENT FEMTOSECOND GAS-PHASE ELECTRON DIFFRACTION SETUP

Omid Zandi, Ph.D.

University of Nebraska, 2017

Advisor: Martin Centurion

We designed and constructed a state-of-the-art high current ultrafast gas electron diffraction experimental setup, which resolved two main challenges that constraint temporal resolution in previous setups. These aforementioned bottlenecks were: the space charge effect due to the Coulomb expansion, and the velocity mismatch between the sub-relativistic electrons (probe) and the exciting laser pulse (pump). In our setup, the problem of space charge effect was ameliorated by compressing 90 keV photo-emitted electron pulses using a radio-frequency electric field. The compression allowed us to increase the beam current by almost two orders of magnitude higher than previously reported. We developed a laser-activated streak camera with a streak velocity of 1.89 mrad/ps to evaluate the compression by measuring the electron pulse duration in situ with a resolution of 100 fs. Electron pulses composed of half a million electrons with a duration of 350 fs were obtained. The velocity mismatch problem, on the other hand, was resolved by employing the technique of laser intensity front tilting. We also constructed a setup to measure the duration of the tilted front laser pulses by an interferometric technique. The timing between the pump and the probe was determined either by photo-ionization induced lensing of the electrons in the gas for normal front laser pulses, or by a transient space charge/surface polarization creation in a copper foil that deflected the electron pulses. The change in the timing between the laser and the electrons was measured by the streak camera with a resolution of 70 fs RMS.

To Bahar, my beloved wife, my best friend.

Acknowledgements

I would like to pay special thankfulness, warmth and appreciation to the persons below who made my research successful and assisted me throughout my PhD journey:

My adviser, Professor Martin Centurion for his vital support and remarkable supervision. Thank you for believing in me and encouraging me to learn and grow. You were a great inspiration for me to expand and develop my knowledge and intuition. I am sincerely indebted for all moments you devoted to teach me.

My dissertation committee, Professor Timothy J. Gay, Professor Herman Batelaan, Professor Bradley A. Shadwick and Professor Christos Argyropoulos. I am greatly indebted for consenting to be my dissertation committee members. I extend my special thanks to Dr. Gay for his support and suggestions during my research, and to Dr. Batelaan and Dr. Shadwick whose lectures were one of the most instructive and encouraging resources for me to learn physics.

My colleagues Dr. Jie Yang, Kyle J. Wilkin and Yanwei Xiong for their kind, passionate and generous help and support during this project. I want to specifically thank Kyle for all the time he worked with me to accomplish this project.

Dr. Matthew S. Robinson and Kyle J. Wilkin for reading my dissertation with care and patience and providing me with their great suggestions.

To people with whom I worked in the mechanic shop and electronic shop in particular, Dr. John Kelty, Bob Rhynalds, Mike Thompson and Brian Farleigh who helped me in an enormous number of projects.

All the other faculty and staff members whose services assisted me in my academic training and research accomplishment.

My beloved wife, Dr. Bahar S. Shahsavarani, whose constant love, care, and encouragement have made me and will keep me strong to persist in the pursuit of my dreams.

My mother Paridokht Sharifi, father, Mohammadhassan Zandi and my family whose love, support, and positive energy paved the way to completion.

Table of Contents

List of Figures

List of Tables

Chapter 1

Introduction to the Theory of Time-Resolved Gas Phase Electron Diffraction

1.1 Introduction

In this chapter, we will briefly review the history, development and theory of ultrafast electron diffraction (UED) techniques for studying atoms and molecules in the gas phase. The chapter starts with a description of the wave-like behavior of electrons and continues to the physics of the diffraction from atoms and molecules. We explain the first Born approximation and its validity and review the analytic formalism of diffraction patterns. Inelastic scattering and scattering from non-stationary potentials will be included in this chapter as well. We give a comparison between electron diffraction experiments versus those with x-rays and neutrons to show why electrons are preferred for gas phase diffraction experiments. Finally, we review the history of electron diffraction experiments in general with a focus on setups that generate ultrafast electron pulses.

1.2 The wave nature of electrons

As Louis de Broglie proposed for the first time in his PhD dissertation, electrons, like all quantum particles, exhibit the properties of waves [1]. In fact, there is a wave function associated to an electron with a wavelength λ related to its momentum p as

$$\lambda = \frac{2\pi\hbar}{p}, \tag{1.1}$$

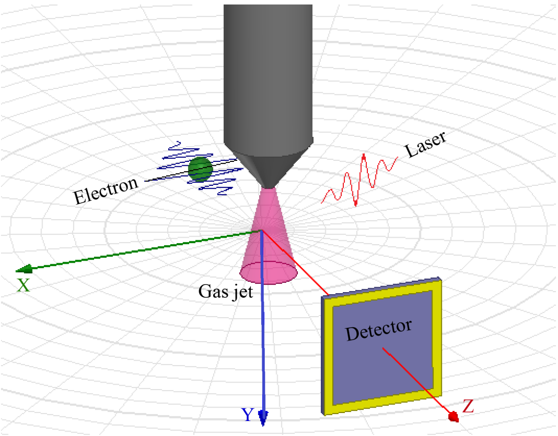

Figure 1.1: Molecules in gas phase come out of a nozzle. An ultrafast laser pulse excites the molecules. An ultrafast electron pulse probes the molecules and reveals the laser induced dynamics.

where $\hbar$ is the reduced Planck's constant. The wave-like nature of electrons can cause an interference pattern resulting from its interaction with other objects. An example of which is a single electron diffraction from a double slit, which is discussed nicely in the first chapter of [2]. In that example, a single electron passing through the double slit will interfere with itself due to its wave-like nature. Consequently, if we repeat the experiment many times, with many single electrons passing through the slits, and record where electrons land on a far distance detector, a diffraction pattern will form. From this pattern, we can extract information about the slits. This is the whole idea behind all electron diffraction experiments: to gain knowledge about the scatterer from the diffraction pattern.

The schematic of a gas phase electron diffraction experiment is shown in Figure1.1. Molecules in the gas phase are ejected from a nozzle into the path of the electrons. In the gas phase, molecules are almost completely isolated from each other's potentials. The electron wave function is diffracted by all of the atoms inside the molecule and shows an interference pattern on the detector. That interference reveals important information about the structure of the molecule. The molecules can be excited by laser pulses, and all the deformations caused by the laser will be reflected in the electron diffraction pattern, allowing us to observe the dynamical evolution of the molecule. The relativistic energy of an electron with mass of m_e and momentum p is

$$E = \sqrt{p^2c^2 + m_e^2c^4}. \tag{1.2}$$

The total energy of an electron with the kinetic energy of $E_k = eV$, where V is the electron accelerating voltage, is

$$E = E_k + m_ec^2. \tag{1.3}$$

Replacing E in equation (1.2) by equation (1.3) and solving the result for p and plugging it in equation (1.1) gives

$$\lambda = \frac{2\pi\hbar}{\sqrt{\frac{E_k^2}{c^2} + 2m_eeV}}. \tag{1.4}$$

Figure 1.2 shows the electron wavelength as a function of its kinetic energy. The wavelength should be short enough in comparison to the size of the scatterer for a good resolution and it is obtained by increasing the accelerating voltage V. An electron with a kinetic energy of E_k has a velocity

$$v = c\sqrt{1 - \left(\frac{m_ec^2}{E_k + m_ec^2}\right)^2}, \tag{1.5}$$

which as a function of E_k is plotted in Figure 1.3.

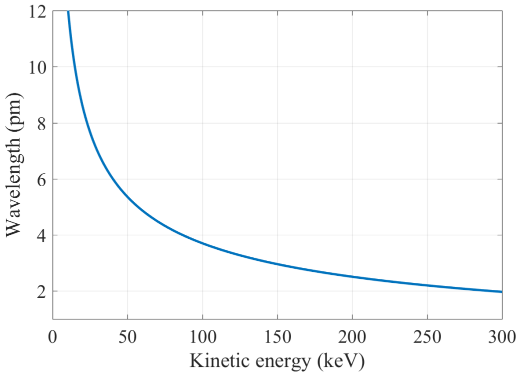

Figure 1.2: de Broglie wavelength of a free electron as a function of its kinetic energy.

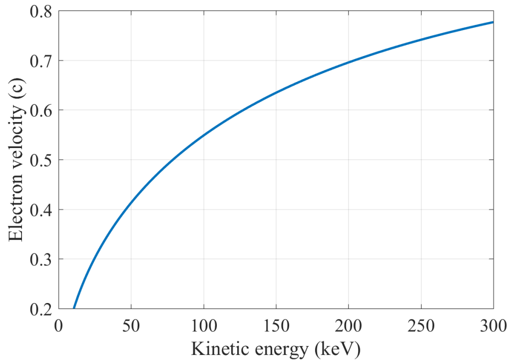

Figure 1.3: Velocity of a free electron in units of c as a function of its kinetic energy.

1.3 Electron scattering by a potential

Suppose an electron is traveling toward an atom or a molecule which we will refer to as the target. The electron will be affected by the target potential $V(\vec{r})$, where $\vec{r}$ is the position vector of the electron. The Schrödinger equation for the electron wave function Ψ will be

$$i\hbar\frac{\partial\Psi}{\partial t} = \left[\frac{-\hbar^2}{2m_e}\nabla^2 + eV(\vec{r})\right]\Psi, \tag{1.6}$$

where e and m_e are the charge and the mass of the electron, respectively. By use of the Schrödinger equation for a real-valued potential, the time derivative of the probability density $\rho = |\Psi|^2$ will be

$$\frac{\partial\rho}{\partial t} = \Psi^*\frac{\partial\Psi}{\partial t} + \Psi\frac{\partial\Psi^*}{\partial t} = -\frac{\hbar}{2m_e}\nabla\cdot(\Psi\nabla\Psi^* - \Psi^*\nabla\Psi), \tag{1.7}$$

where "*" indicates the complex conjugate. The probability current density (PCD) is defined as

$$\vec{J} = \frac{\hbar}{2m_e}(\Psi\nabla\Psi^* - \Psi^*\nabla\Psi), \tag{1.8}$$

which inserted into equation (1.7) gives

$$\frac{\partial\rho}{\partial t} + \nabla\cdot\vec{J} = 0. \tag{1.9}$$

This is a continuity equation for the probability density and current. In the quantum theory of diffraction, the PCDs determine the scattering process. For a better illustration, let us write the wave vector of an electron that is scattered by a potential of a target located at the coordinate origin as

$$\Psi = \Psi_i + \Psi_s = A\left[e^{ikz} + f(\theta,\phi)\frac{e^{ikr}}{r}\right], \tag{1.10}$$

where $\Psi_i = Ae^{ikz}$ is a plane wave moving along the z axis and represents the incident and unscattered part of the wave function and $\Psi_s = Af(\theta,\phi)\frac{e^{kr}}{r}$ is a spherical wave and represents the scattered part of the wave function; k is the electron wave number. As we will see, $f(\theta,\phi)$ is the scattering amplitude and A is the normalization constant and is set equal to one if $|f(\theta,\phi)/r| \ll 1$. In this equation, we have assumed that the scattering is elastic, i.e., after the scattering, the energy and hence the wave number of the electron are the same as they were before the scattering. We can show that equation (1.10) satisfies the Schrödinger equation outside of the potential region and for $kr \gg 1$. The PCD corresponding to the wavefunction in equation (1.10) for $kr \gg 1$ is

$$\vec{J} = \vec{J}_i + \vec{J}_s \approx \frac{\hbar k}{m_e}\hat{z} + \frac{\hbar k}{m_e}|f(\theta,\phi)|^2\frac{\hat{r}}{r^2}, \tag{1.11}$$

where we have used the approximation

$$\nabla\Psi_s \approx \frac{\partial\Psi_s}{\partial r}\,\hat{r} \tag{1.12}$$

for $kr \gg 1$. The differential scattering cross section is the probability current crossing a differential area over the incident beam PCD, i.e.:

$$d\sigma(\theta,\phi) = \frac{\vec{J}_s(\theta,\phi)}{|\vec{J}_i|}\cdot r^2\hat{r}d\Omega = |f(\theta,\phi)|^2 d\Omega, \tag{1.13}$$

where $d\Omega$ is shown figuratively in Figure 1.4. What we detect on the screen is proportional to $|f(\theta,\phi)|^2$. The goal is to relate $f(\theta,\phi)$ to the potential function of

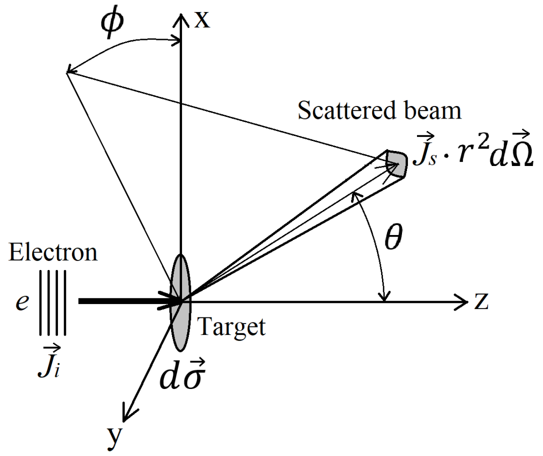

Figure 1.4: Concept of cross section for an electron hitting a target. The incoming electrons that fall into the differential cross section $d\sigma$ are scattered to all space. A detector, extended over the differential solid angle of $d\vec{\Omega}$ far from the target, will detect the probability current $\vec{J}_s \cdot r^2 d\vec{\Omega}$.

the target so that by measuring $|f(\theta, \phi)|^2$, we find information about $V(\vec{r})$.

We demand that Ψ satisfies the time-independent Schrödinger's equation that describes the scattering process. We have

$$-\frac{\hbar^2}{2m_e}\nabla^2\Psi(\vec{r}) + eV(\vec{r})\Psi(\vec{r}) = E_k\Psi(\vec{r}), \tag{1.14}$$

or

$$(\nabla^2 + k^2)\Psi(\vec{r}) = U(\vec{r})\Psi(\vec{r}), \tag{1.15}$$

for

$$U(\vec{r}) = \frac{2em_e}{\hbar}V(\vec{r}); \quad k^2 = \frac{2m_eE_k}{\hbar^2} = \frac{4\pi^2}{\lambda^2}, \tag{1.16}$$

where E_k is the kinetic energy of the electron and λ its wavelength. A solution to equation (1.15) is

$$\Psi(\vec{r}) = \Psi_0(\vec{r}) + \int d^3\vec{r}\,'G(\vec{r} - \vec{r}\,')U(\vec{r}\,')\Psi(\vec{r}\,'), \tag{1.17}$$

where $\Psi_0(\vec{r})$ satisfies the homogeneous equation $(\nabla^2 + k^2)\Psi(\vec{r}) = 0$ and $G(\vec{r})$ is the Green's function satisfying

$$(\nabla^2 + k^2)G(\overrightarrow{r} - \overrightarrow{r}') = \delta(\overrightarrow{r} - \overrightarrow{r}'), \tag{1.18}$$

where $\delta(\overrightarrow{r})$ is the Dirac delta function. It can be shown that the Green's function

$$G(\overrightarrow{r} - \overrightarrow{r}') = -\frac{1}{4\pi}\frac{e^{i\overrightarrow{k}\cdot(\overrightarrow{r}-\overrightarrow{r}')}}{|\overrightarrow{r} - \overrightarrow{r}'|} \tag{1.19}$$

satisfies equation (1.18) [3]. Therefore, we have

$$\Psi(\overrightarrow{r}) = \Psi_0(\overrightarrow{r}) - \frac{1}{4\pi}\int d^3\overrightarrow{r}'\frac{e^{i\overrightarrow{k}\cdot(\overrightarrow{r}-\overrightarrow{r}')}}{|\overrightarrow{r} - \overrightarrow{r}'|}U(\overrightarrow{r}')\Psi(\overrightarrow{r}'). \tag{1.20}$$

The distances over which the potential is extended is usually much smaller than the distance between the potential location and the detector, i.e., $r \gg r'$. Thus, we make the approximations

$$|\overrightarrow{r} - \overrightarrow{r}'| \approx r; \quad \overrightarrow{k}\cdot(\overrightarrow{r} - \overrightarrow{r}') \approx k(r - \hat{r}\cdot\overrightarrow{r}'), \tag{1.21}$$

where $\hat{r}$ is a unit vector in the direction of $\overrightarrow{r}$. By these approximations, the integral equation (1.20) becomes

$$\Psi(\overrightarrow{r}) = \Psi_0(\overrightarrow{r}) - \frac{e^{ikr}}{4\pi r}\int d^3\overrightarrow{r}'e^{-i\overrightarrow{k}\cdot\overrightarrow{r}'}U(\overrightarrow{r}')\Psi(\overrightarrow{r}'). \tag{1.22}$$

By comparing this equation to equation (1.10), we find

$$\Psi_0(\overrightarrow{r}) = e^{ikz}; \quad f(\theta,\phi) = -\frac{1}{4\pi}\int d^3\overrightarrow{r}'e^{-i\overrightarrow{k}\cdot\overrightarrow{r}'}U(\overrightarrow{r}')\Psi(\overrightarrow{r}') \tag{1.23}$$

for $A = 1$. By use of equation (1.16), the scattering amplitude is related to the target potential as

$$f(\theta,\phi) = -\frac{1}{2\pi}\frac{em_e}{\hbar^2}\int d^3\overrightarrow{r}'e^{-i\overrightarrow{k}\cdot\overrightarrow{r}'}V(\overrightarrow{r}')\Psi(\overrightarrow{r}'), \tag{1.24}$$

and the differential cross section will be

$$d\sigma(\theta,\phi) = \frac{e^2 m_e^2 d\Omega}{4\pi^2\hbar^4}\left|\int d^3\vec{r}' e^{-i\vec{k}\cdot\vec{r}'} V(\vec{r}')\Psi(\vec{r}')\right|^2. \tag{1.25}$$

Altough equation (1.25) relates the differential cross section to the target potential, it is not practical since the electron wave function is not known in general. To proceed, we need to apply an approximation known as the Born approximation.

1.3.1 The Born approximation

The Born approximation begins by assuming a simple wave function for $\Psi(\vec{r}')$ and inserting it in equation (1.22) to get an updated function for $\Psi(\vec{r}')$. This process should be repeated till the wave function converges to its final form. The electron wave function, in the $N-$th Born approximation is written in the series of

$$\Psi_N(\vec{r}) = \sum_{n=0}^{n=N} \phi_n(\vec{r}) \tag{1.26}$$

where

$$\phi_0(\vec{r}) = e^{ikz}; \tag{1.27}$$

and

$$\phi_n(\vec{r}) = \int G(\vec{r} - \vec{r}')U(r')\cdots G(\vec{r}^{(n-1)} - \vec{r}^{(n)})U(\vec{r}^{(n)})\phi_0(\vec{r}^{(n)})d^3\vec{r}'\cdots d^3\vec{r}^{(n)}. \tag{1.28}$$

The Green's functions in equation (1.28) are given by equation (1.19) [4]. Then, the $N-$th Born approximation scattering amplitude will be

$$f_N(\theta,\phi) = -\frac{1}{2\pi}\frac{em_e}{\hbar^2}\int d^3\vec{r}' e^{-i\vec{k}\cdot\vec{r}'} V(\vec{r}')\Psi_{N-1}(\vec{r}'). \tag{1.29}$$

The scattering amplitude f_N converges if the wave function Ψ_N converges [4]. For a high-energy electron and a confined potential with a finite integral over all space, Ψ_N and hence f_N converge [4]. In many applications, the first Born approximation suffices. By writting $f = f_1$ and dropping the primes, we have

$$f(\theta, \phi) = -\frac{1}{2\pi}\frac{em_e}{\hbar^2}\int d^3\vec{r}e^{-i(\vec{k}\cdot\vec{r}-kz)}V(\vec{r}). \tag{1.30}$$

The argument of the exponential inside the integral in equation (1.30) can be rewritten as

$$\vec{k}\cdot\vec{r} - kz = k(\hat{r}-\hat{z})\cdot\vec{r} = \vec{s}\cdot\vec{r}, \tag{1.31}$$

where the vector $\vec{s}$:

$$\overrightarrow{(}s) = k(\hat{r}-\hat{z}) \tag{1.32}$$

is the momentum transferred to the electron by the scattering potential. Equation (1.30), using the momentum transfer function, will be

$$f(\theta, \phi) = -\frac{1}{2\pi}\frac{em_e}{\hbar^2}\int d^3\vec{r}e^{-i\vec{s}\cdot\vec{r}}V(\vec{r}). \tag{1.33}$$

Equation (1.33) shows that the scattering amplitude is in fact the Fourier transform of scattering potential. Consequently, by taking the inverse Fourier transform from the scattering amplitude, we can find the scattering potential. However, in practice, the intensity that we can detect $I(s)$, is

$$I(s) = |f(s)|^2, \tag{1.34}$$

which means the phase of f is lost. For obtaining the scattering potentials in general, we need to assign a phase to the scattering amplitude so we can perform the inverse Fourier transform. Properties of the Born approximation are discussed in detail in [5] and [6].

1.3.2 Scattering amplitude from a charge distribution

Let us go back to equation (1.33) and express it in terms of the target charge distribution instead of the scattering potential. The potential of a charge distribution with a charge density of $\rho(\vec{r})$ is

$$V(\vec{r}) = \frac{1}{8\pi\epsilon_0}\int d^3\vec{r}'\frac{\rho(\vec{r}')}{|\vec{r}-\vec{r}'|}, \tag{1.35}$$

where the integral is taken over the charge distribution. We insert this equation into equation (1.33), giving

$$f(\vec{s}) = -\frac{em_e}{16\pi^2\epsilon_0\hbar^2}\int d^3\vec{r}e^{-i\vec{s}\cdot\vec{r}}\int d^3\vec{r}'\frac{\rho(\vec{r}')}{|\vec{r}-\vec{r}'|}. \tag{1.36}$$

By changing the the order of integration, we find

$$f(\vec{s}) = -\frac{em_e}{16\pi^2\epsilon_0\hbar^2}\int d^3\vec{r}'\rho(\vec{r}')\int d^3\vec{r}\frac{e^{-i\vec{s}\cdot\vec{r}}}{|\vec{r}-\vec{r}'|}. \tag{1.37}$$

We define a vector $\vec{x} = \vec{r} - \vec{r}'$, by use of which the second integral in equation (1.37) can be written as

$$\begin{aligned}\int d^3\vec{r}\frac{e^{-i\vec{s}\cdot\vec{r}}}{|\vec{r}-\vec{r}'|}\\ &= e^{-i\vec{s}\cdot\vec{r}'}\int d^3\vec{x}\frac{e^{-i\vec{s}\cdot\vec{x}}}{x}\\ &= 2\pi e^{-i\vec{s}\cdot\vec{r}'}\int_{x=0}^{\infty}x^2dx\int_{\alpha=0}^{\pi}\sin\alpha\,d\alpha\,\frac{e^{-isx\cos\alpha}}{x}\\ &= \frac{4\pi}{s}e^{-i\vec{s}\cdot\vec{r}'}\int_{x=0}^{\infty}\sin(sx)dx.\end{aligned} \tag{1.38}$$

To evaluate the last integral, we use the following trick:

$$\int_{x=0}^{\infty}\sin(sx)dx = \lim_{\kappa\to 0}\int_{x=0}^{\infty}e^{-\kappa x}\sin(sx)dx = \frac{1}{s} \tag{1.39}$$

for κ being an arbitrary real and positive number. Now, equation (1.37), by dropping the primes, becomes

$$f(\vec{s}) = -\frac{em_e}{4\pi\epsilon_0\hbar^2}\frac{1}{s^2}\int d^3\vec{r}\rho(\vec{r})e^{-i\vec{s}\cdot\vec{r}}. \tag{1.40}$$

This equation shows that the scattering amplitude is proportional to the Fourier transform of the target charge density distribution. For an atom with an atomic number Z, the charge distribution will be

$$\rho(\overrightarrow{r}) = Ze\delta(\overrightarrow{r}) - \rho_e(\overrightarrow{r}), \tag{1.41}$$

where $Ze\delta(\overrightarrow{r})$ and $\rho_e(\overrightarrow{r})$ are the nuclear and electronic charge densities, respectively, where the nucleus charged is localized at the origin. By plugging equation (1.41) in 1.40, we have

$$f(\overrightarrow{s}) = -\frac{em_e}{4\pi\epsilon_0\hbar^2}\frac{Ze - g_e(s)}{s^2}, \tag{1.42}$$

where

$$g_e(\overrightarrow{s}) = \int d^3\overrightarrow{r}\rho_e(\overrightarrow{r})e^{-i\overrightarrow{s}\cdot\overrightarrow{r}}. \tag{1.43}$$

1.3.3 Scattering from atoms

An atom can be modeled as a localized charge at the nucleus screened by a cloud of electrons. The potential of an atom, in this regard, can be approximated by the Yukawa Potential [6]

$$V(\overrightarrow{r}) = \gamma\frac{e^{-\mu r}}{r}, \tag{1.44}$$

for $\gamma = -\frac{Ze}{4\pi\epsilon_0}$, where Z is the atomic number of the scatterer, ϵ_0 is the permittivity of free space, and μ is a constant characterizing the spatial extent of the potential. This potential is spherically symmetric, so the scattering amplitude corresponding to it is

$$f(\overrightarrow{s}) = -\gamma\frac{em_e}{\hbar^2}\int drr^2\frac{e^{-\mu r}}{r}\int d\alpha\sin(\alpha)e^{-i\overrightarrow{s}\cdot\overrightarrow{r}}. \tag{1.45}$$

For the argument of the exponential, we may write

$$\overrightarrow{s}\cdot\overrightarrow{r} = k(\hat{r} - \hat{z})\cdot\overrightarrow{r} = 2k\sin\frac{\theta}{2}/, r\cos\alpha, \tag{1.46}$$

where α is the angle between $\overrightarrow{s}$ and $\overrightarrow{r}$ and θ is the angle between unit vectors $\hat{r}$ and $\hat{z}$. By inserting equation (1.46) into equation (1.45), we get

$$\begin{aligned} f(s) &= -\gamma \frac{e m_e}{\hbar^2} \int dr r'^2 \frac{e^{-\mu r}}{r} \int d\alpha \sin(\alpha) e^{-i2k \sin\frac{\theta}{2} r \cos\alpha} \\ &= -\gamma \frac{2 e m_e}{\hbar^2 s} \int_0^\infty dr \sin(sr) e^{-\mu r} = -\gamma \frac{2 e m_e}{\hbar^2} \frac{1}{\mu^2 + s^2}. \end{aligned} \tag{1.47}$$

where

$$s = |\overrightarrow{s}| = 2k \sin\frac{\theta}{2}. \tag{1.48}$$

By plugging equation (1.48) into equation (1.47) and inserting the result in equation (1.25), the scattering cross section will be obtained as:

$$\frac{d\sigma}{d\Omega} = \left(\frac{\beta}{(\frac{4\pi}{\lambda})^2 \sin^2(\frac{\theta}{2}) + \mu^2} \right)^2, \tag{1.49}$$

where $\beta = \gamma \frac{e m_e}{\hbar^2}$ is a constant and has a dimension of L^{-1}. The accuracy of this result can be evaluated by comparing the second Born approximation scattering amplitude to the first Born approximation one. The result is [6]

$$\left| \frac{f_2}{f_1} \right|_{\theta=0} = \left| \frac{\gamma m_e}{\hbar^2 \sqrt{(4\pi/\lambda)^2 + \mu^2}} \right|. \tag{1.50}$$

In case of high energy electrons, their wavelength is much shorter than $1/\mu$; hence, the convergence condition becomes

$$\frac{|\gamma| m_e \lambda}{4\pi\hbar^2} \ll 1. \tag{1.51}$$

By plugging $\gamma = -\frac{Ze}{4\pi\epsilon_0}$ into equation 1.51, we find

$$Z \ll \frac{(4\pi)^2 \epsilon_0 \hbar^2}{m_e \lambda e^2} \approx 168 \tag{1.52}$$

for an electron with a kinetic energy of 90 keV. The atomic number condition in equation (1.52) holds for all atoms and that is the reason why the first Born approximation provides fairly accurate results in electron diffraction experiments.

Here, we give two examples of scattering of an electron with a kinetic energy of 90 keV from helium and from neon atoms. For each example, we used the analytical data from [7] together with a function in equation (1.49) fit to it. The cross section data was obtained by using the relativistic Dirac partial-wave analysis [7]. Figures 1.5a and 1.5b show the cross sections for helium and neon, respectively. From the fit curves we can obtain the atomic potentials, and hence the charge distribution.

The Yukawa potential corresponds to the charge density distribution

$$\rho(r) = 4\pi\gamma\epsilon_0\left(\delta(\vec{r}) - \frac{\mu^2}{4\pi}\frac{e^{-\mu r}}{r}\right), \tag{1.53}$$

where the delta function represents the localized nucleus charge and the second term represents the electron cloud around the nucleus. This charge distribution can model the structure of some atoms accurately for the purpose of high energy electron scattering, like the two examples we provided here, but should be replaced by a more accurate descriptions for many other atoms. More accurate charge distribution densities have been obtained from their wave functions by the Hartree-Fock or other methods [7, 8].

In the Yukawa model, the charge density and hence the scattering potential of the atoms is linearly proportional to the atomic number Z. The Fourier transform is linear which means the scattering factor is also linearly proportional to Z. The total scattering cross section can be obtained by integrating equation (1.49) over all angles and is equal to $\frac{1}{\mu^2}\frac{4\pi\beta^2}{(\frac{4\pi}{\lambda})^2+\mu^2}$ which increases proportionally to $\frac{Z^2}{\mu^2}$.

A more rigorous analysis of the scattering process, by use of partial wave analysis, provides functions for $f(s)$ that are not real and hence in the literature they are called the “scattering factors” instead of the “scattering amplitudes” [4, 6]. For scattering from isolated atoms, the complex nature of functions of $f(s)$ do not change the detected intensity. However, the phases of $f(s)$ becomes important if we consider scattering from a molecule.

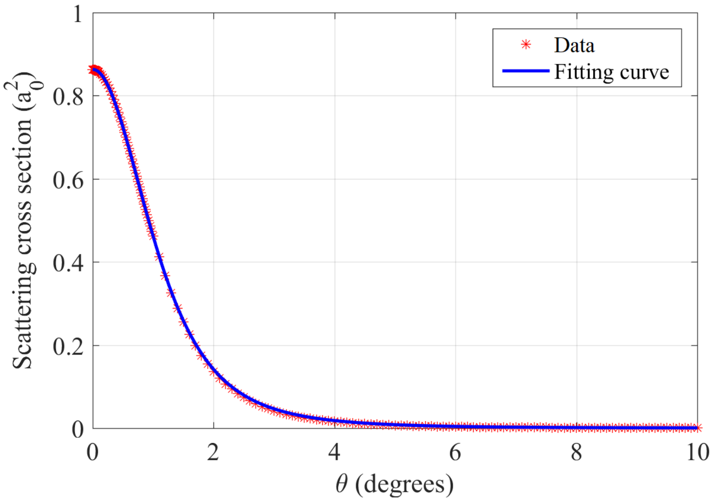

(a)

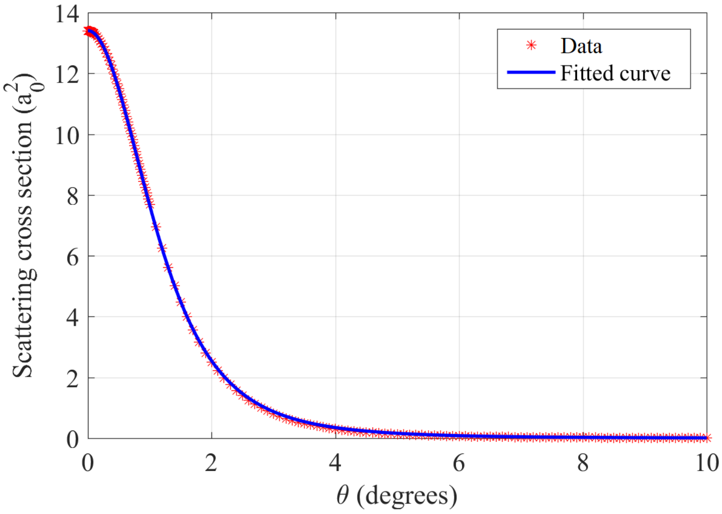

(b)

Figure 1.5: Scattering cross section of atomic (a) helium and (b) neon for an electron with 90 keV kinetic energy in units of square of Bohr radius. The data are taken from [7]. We fit the function in equation (1.49) to both measurements. For helium we got $\mu = 4.6\mathring{A}^{-1}$ and for neon $\mu_{Ne} = 4.9\mathring{A}^{-1}$.

The phase of $f(s)$, can be obtained analytically for a high energy electron scattered by the Yukawa potential as [9]

$$\eta(s) = \frac{Ze^2 m_e \lambda}{8\pi^2 \epsilon_0 \hbar^2} \frac{\mu^2 + s^2}{s\sqrt{(2\mu)^2 + s^2}} \ln\left(\frac{\sqrt{(2\mu)^2 + s^2} + s}{\sqrt{(2\mu)^2 + s^2} - s}\right). \tag{1.54}$$

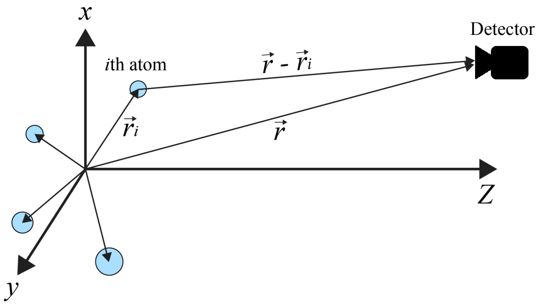

Figure 1.6: Scattering of an electron from a molecule.

1.3.4 Scattering from randomly-oriented isolated molecules

Suppose there is a molecule composed of N atoms where the $i-$th atom is located at $\vec{r}_i$ as shown in Figure 1.6. The scattering factor of the $i-$th atom will be $f_i(\theta)e^{i\vec{k}\cdot\vec{r}_i}$ since it gains an extra phase because of its distance from the origin. The total scattering factor of the molecule will be

$$F(\theta,\phi)=\sum_{i=1}^{N} f_i(\theta)e^{i\vec{s}\cdot\vec{r}_i}. \tag{1.55}$$

The differential scattering cross section of the molecule will be

$$\begin{aligned}\frac{d\sigma}{d\Omega}=FF^*&=\sum_{i=1}^{N}\sum_{j=1}^{N}|f_i|e^{i\eta_i}e^{i\vec{s}\cdot\vec{r}_i}|f_j|e^{-i\eta_j}e^{-i\vec{s}\cdot\vec{r}_j}\\&=\sum_{i=1}^{N}\sum_{j=1}^{N}|f_i||f_j|e^{i(\eta_i-\eta_j)}e^{i\vec{s}\cdot(\vec{r}_i-\vec{r}_j)},\end{aligned} \tag{1.56}$$

where η_i is the phase of f_i. For an ensemble of M randomly-oriented molecules we have to average FF^* over all angles between $\vec{s}$ and $(\vec{r}_i-\vec{r}_j)$, or

$$
\begin{aligned}
\langle\frac{d\sigma}{d\Omega}\rangle &= M\sum_{i=1}^{N}\sum_{j=1}^{N}|f_i||f_j|e^{i(\eta_i-\eta_j)}\frac{1}{4\pi}\int_{\beta=0}^{2\pi}\int_{\alpha=0}^{\pi}e^{i|\vec{s}||\vec{r}_i-\vec{r}_j|\cos\alpha}\sin\alpha d\alpha d\beta \\
&= M\sum_{i=1}^{N}\sum_{j=1}^{N}|f_i||f_j|e^{i(\eta_i-\eta_j)}\frac{1}{4\pi}\int_{\beta=0}^{2\pi}\int_{\alpha=0}^{\pi}e^{isr_{ij}\cos\alpha}\sin\alpha d\alpha d\beta \\
&= M\sum_{i=1}^{N}\sum_{j=1}^{N}|f_i||f_j|e^{i(\eta_i-\eta_j)}\frac{\sin sr_{ij}}{sr_{ij}} \\
&= M\sum_{i=1}^{N}\sum_{j=1}^{N}|f_i||f_j|\cos(\eta_i-\eta_j)\frac{\sin sr_{ij}}{sr_{ij}},
\end{aligned}
\tag{1.57}
$$

where $r_{ij} = |\vec{r}_i - \vec{r}_j|$. The last equality in equation (1.57) can be separated in two terms as

$$
\langle\frac{d\sigma}{d\Omega}\rangle = M\sum_{i=1}^{N}|f_i|^2+M\sum_{i=1}^{N}\sum_{j\neq i}^{N}|f_i||f_j|\cos(\eta_i-\eta_j)\frac{\sin sr_{ij}}{sr_{ij}}. \tag{1.58}
$$

The first term on the right hand side of 1.58 is just a summation of the scattering cross section from each atom of the molecule and we label it as

$$
I_{atom} = M\sum_{i=1}^{N}|f_i|^2. \tag{1.59}
$$

This term has no information about the molecule's structure, and by finding the scattering factors from available tables, it can be determined and subtracted from the measured diffraction pattern.

However, the second term has interference terms $\frac{\sin sr_{ij}}{sr_{ij}}$ that depend on the distances between the atoms and we label it as

$$
I_{molecule} = M\sum_{i=1}^{N}\sum_{j\neq i}^{N}|f_i||f_j|\cos(\eta_i-\eta_j)\frac{\sin sr_{ij}}{sr_{ij}}. \tag{1.60}
$$

In all electron diffraction experiments, this term is used to extract the structural information. In this model, we ignore multiple scattering which means that an electron which is scattered from an atom will not be rescattered from another atom. Furthermore, we assume that the atomic bonds inside the molecule have a negligible contribution to the scattering signal as if the atoms are independent from each other. This assumption is regarded as the independent atom model in the literature [10]. The other assumption that we have made is that the scattered electrons from atoms of two different molecules do not add coherently. This assumption is true if the distance between adjacent molecules in the ensemble is larger than the coherence length of the electron wave function. In a gas phase experiment, if the gas density is in order of 10^{17} molecules per cm^3 or less, the average distance between molecules will be of the order of 20 nm or more, which is larger than a typical transverse coherence of the electron beam that is of order of 4 nm (see Section 2.7.)

1.4 Inelastic scattering

The theory developed with the Born approximation assumes elastic scattering of electrons from a target. In elastic scattering, the energy of the incoming and scattered electrons are the same but their momenta differ and all the information about the structure of the target is encoded in that momentum difference. Nonetheless, not all the electrons are scattered elastically. In fact, if the incident electron penetrates deeply into the atom, there will be a significant chance to lose energy [11]. The total intensity $I(s)$ for the first Born approximation, by including the inelastic electron scattering from an atom, is [8]

$$I(s) \propto |f(s)|^2 + \frac{4S(s)}{a_0^2 s^4}, \tag{1.61}$$

where $f(s)$ is the elastic scatting factor, $S(s)$ is called the inelastic scattering factor, and a_0 is the Bohr radius. The values of $S(s)$ for different atoms are tabulated in [8] and used in Figure 1.7 to illustrate $|f(s)|^2$ and $\frac{4S(s)}{a_0^2 s^4}$ for a 90 keV electron scattered from a neon atom. As we see, the inelastic scattering cross section is bigger than the elastic scattering cross section for $s < 1.6\mathring{A}^{-1}$, but it

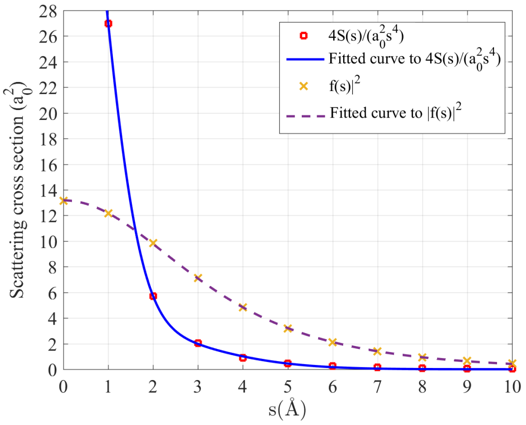

Figure 1.7: Functions $|f(s)|^2$ and $\frac{4S(s)}{a_0^2s^4}$ for a 90 keV electron scattered from a neon atom. The data points are taken from [8]. The curve fit to $|f(s)|^2$ is a squared Lorentzian and the curve fit to $\frac{4S(s)}{a_0^2s^4}$ is a summation of two zero-centered Gaussians.

drops quickly. For $s > 2\mathring{A}^{-1}$ most of the detected signal is due to the elastically scattered electrons. The curve fit to $|f(s)|^2$ is a squared Lorentzian function (see equation (1.49)) and the curve fit to $\frac{4S(s)}{a_0^2s^4}$ is a summation of two Gaussians, both centered at $s = 0$. The inelastic electron wave functions do not add coherently and hence they do not show interference patterns in diffraction from molecules [8]. Instead, they form a smooth background signal that, together with the atomic scattering cross section in equation (4.2a), can be subtracted from the measured diffraction pattern as we will discuss it in more details in Section 4.4.1.

1.5 Electron momentum spread and blurred diffraction patterns

An actual electron beam may have a finite momentum spread that can be due to the creation, acceleration, compression or the space charge effect. This is in contrast to a plane wave model with a single wavelength that we considered in the previous sections. The incident electron pulse can be decomposed into its plane wave components as

$$\Psi_i = \int dkA(k)e^{ikz}, \tag{1.62}$$

where each component has its own wavelength and the integral is over all electron momenta. Now, it is possible that two components with different wavelengths gain momenta such that they are deflected to the same angle. This process will blur the diffraction pattern on the detector. To explain this blurring effect consider the momentum transfer in equation (1.48). The differential of s is

$$ds = \frac{\partial s}{\partial \lambda} d\lambda + \frac{\partial s}{\partial \theta} d\theta. \tag{1.63}$$

Suppose we are looking at the diffraction pattern from a fixed angle θ, so $d\theta$ is zero. From equation (1.63), we have

$$ds = -\frac{4\pi}{\lambda^2} d\lambda \sin(\frac{\theta}{2}). \tag{1.64}$$

This equation means that two plane-wave components with wavelengths λ and $\lambda + d\lambda$ that gain the momenta s and $s + ds$ from the scattering potential respectively, will be deflected to the same angle, where ds is determined by equation (1.64). Therefore, there is an ambiguity for the detected signal at angle θ in the sense that we do not know if it is because of the electron pulse wavelength spread or the scattering potential. As a result, the wavelength (or momentum) spread of the electron pulse should be as small as possible. This problem can be ameliorated if the detector has a narrow bandwidth around the wavelengths of interest.

The same argument holds for the transverse momentum spread of the electron pulse, since the angle θ is measured from the initial direction of the electron to the angle of scatter. For this reason, a collimated electron beam on the target is preferred.

1.6 Scattering from non-stationary potentials

So far, we assumed that the target is in a stationary state which means that the scattering potential is not a function of time. We also assumed that the wave function of the incident electron is a plane wave. In time-resolved experiments, these assumptions are not true. The target can be excited and put into a non-stationary state. The incident electron beam is composed of highly-charged electron bunches with a femtosecond duration which cannot be described by a single wavelength plane wave function that exists everywhere and in all time.

For non-stationary targets, if we assume that 1) the time scale over which the target evolves is longer than the duration of the electron pulse such that the target is temporally frozen while the collision process takes place [12] and 2) the electron pulse is a passive probe meaning that it does not change the state of the target, we may generalize equation (1.33) to

$$f(\vec{s};t) = -\frac{1}{2\pi}\frac{m_e}{\hbar^2}\int d^3\vec{r}e^{-i\vec{s}\cdot\vec{r}}V(\vec{r};t). \tag{1.65}$$

However, these assumptions do not hold in general, and equation (1.65) is not a valid description. A valid description can be obtained through the Hamiltonian that describes the whole quantum system, not just the electron. In other words, the true Hamiltonian has three terms due to the target H_{target}, the electron $H_{electron}$ and the interaction between the two eV:

$$H = H_{target} + H_{electron} + eV. \tag{1.66}$$

This equation should be used instead of the Hamiltonian in equation (1.6), where H_{target} was absent. Also the electron should not be described by a plane wave, for such an assumption prevents the probe-induced dynamics in the calculations. Instead, the whole quantum system, including the target, should be modeled by a wave packet [13]. This problem was first addressed in ultrafast x-ray experiments on isolated molecules [14–18]. The treatment has been based on quantum electrodynamics. Nevertheless, the results are generalizable to electrons if we replace the scattering operator for x-rays by the electron scattering operator [19].

1.7 Electrons *vs.* x-rays and neutrons

In this section, we compare the diffraction experiments done with electrons, x-rays and neutrons. Electrons interact with the target molecules and atoms through the Coulomb potential and are affected by both the nuclei and all the electrons of the target. The probability of multiple scattering is highest for electrons. Electrons that are used in diffraction experiments have a typical kinetic energy of 10 keV or higher corresponding to de Broglie wavelengths of 12 pm or shorter by which a good spatial resolution can be achieved. Electrons are charged particles and because of the Coulomb repulsion it is difficult to make bright electron pulses. Nevertheless, as we discuss in this dissertation, there are techniques to overcome the space charge effect and to generate ultrafast bright electron pulses to observe ultrafast dynamics at the level of atoms and molecules.

X-rays interact mostly with the electron cloud around the nuclei since the nuclei themselves are much heavier than the electrons and have negligible induced dipole moments due to the x-ray field. Hence, the atoms have a much weaker interaction with x-rays than with electrons. The elastic scattering cross section of x-rays is around 10^6 times smaller than that of electrons [20] and similar to electrons it increases drastically with Z. The typical wavelengths of x-ray photons for diffraction experiments are around $1-10\AA$ and are sufficient to observe atomic structure. By use of a free electron laser, ultrafast x-ray pulses have been achieved [21]. So similar to electrons, x-rays are suitable for gas phase ultrafast diffraction experiments [22, 23]. Nonetheless, if we can generate bright ultrafast electron pulses, then the electron diffraction will be superior to the x-ray diffraction for gas phase samples due to their higher scattering cross section. A comparison between ultrafast electron and x-ray diffraction experiments on molecules is given in [19].

The other particles used for diffraction experiments are neutrons. Neutrons interact with both the nucleus of each atom through the short range strong force and the magnetic moment of unpaired electrons. The neutrons scattering cross section due to the nuclei interactions is not a smooth function of Z and does not vary too much among different atoms [24]. In contrast to both electrons and x-rays, the scattering signal from a single atom is not a function of angle since the size of the nucleus is around five orders of magnitude smaller than the typical wavelength of a neutron ($\sim 1\mathring{A}$) [24]. Therefore, neutrons can reveal more information on fine details of the molecular structures than electrons or x-rays. Moreover, neutrons can be used to divulge magnetic properties of materials. The neutron beams have low density and cannot be used for gas phase experiments due to the dilute nature of the sample. There is no ultrafast neutron source for time resolved diffraction experiments.

1.8 History of gas phase electron diffraction experiments

So far we reviewed the theory of electron diffraction. Now we will review the history of electron diffraction experiments. The history of gas phase electron diffraction experiments begins in the 1930s [25–39]. Figure 1.8 shows the schematic of the first electron diffraction apparatus [26]. The electrons were generated by a cold cathode of a gas discharge tube, with a kinetic energy of 43 ± 0.2 kV. The gas molecules were injected to the path of the electrons (from the bottom in the figure) by a nozzle and went up to a liquid air trap. There was a fluorescent screen that detected the electrons. The design was adapted by many other researchers afterwards and became the basis for almost all modern gas phase static electron diffraction apparatuses. However, there have been significant improvements in the electron gun and hence the beam profile and stability, the vacuum, and specially in the detection techniques [40]. Another type of apparatus was also developed during the same period for lower energy electrons (below 800 V) but with a beam current of around 10 mA [41]. In that design, shown in Figure 1.9, the electron gun could rotate around the gas steam and the scattered electrons were trapped by a fixed Faraday cup. The current of scattered electrons at a particular angle was directly measured by a galvanometer. A review on the history, development and applications of static electron diffraction experiments both in crystallography and in gas phase can be found in [42].

The continuous electron beam was later used to observe formation of molecules by heating an ensemble of their parent species where both coexist in a reversible

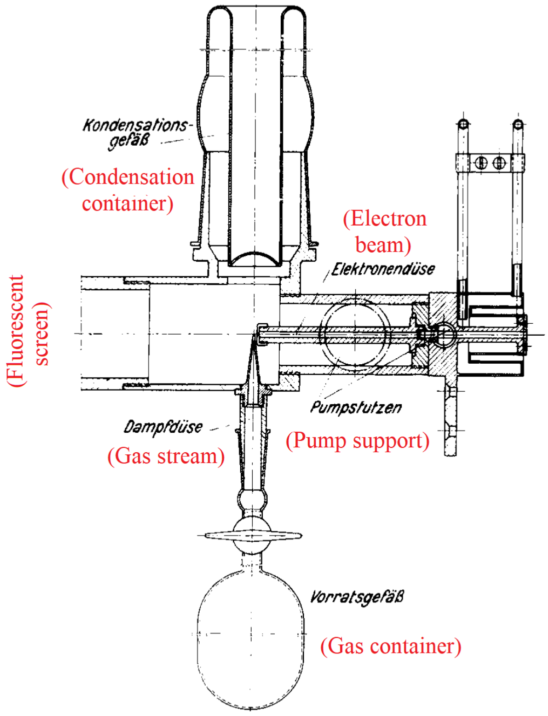

Figure 1.8: Schematic of the first gas phase electron diffraction apparatus. (Figure courtesy of [26]; used with permission.)

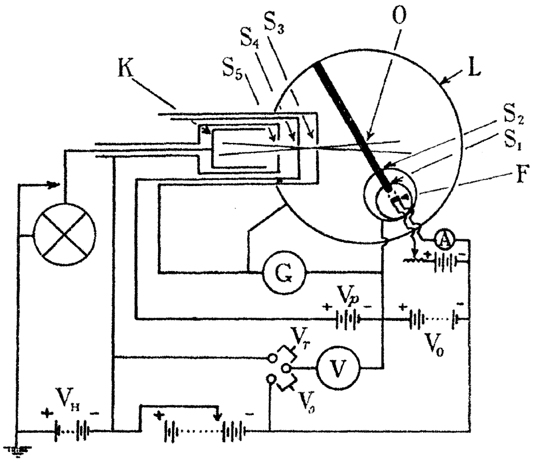

Figure 1.9: Schematic of the other type of gas phase electron diffraction experiment. Electrons are generated by tungsten filament F located inside two cylinders and go out through holes S_1 and S_2. The gun could rotate around the axis O where gas was injected by a capillary. sceterred electrons were trapped by the Faraday cup K. The potential of concentric cylinders around the Faraday cup were chosen to filter inelastically scattered electrons. (Figure courtesy of [43]; used with permission.)

equilibrium [44–46]. The first time-resolved electron diffraction with pulsed electrons was done by synchronizing the electron pulses to either a flash lamp to photo-excite the gas phase target [47] or to a microsecond laser pulse [48]. In 1992, the group of Professor Ahmed Zewail reported their first results using UED of isolated molecules [49]. They used ultrafast laser pulses for both generation of the electrons by photo-emission and excitation of the gas molecules. Figure 1.10 shows their electron diffraction apparatus. In that setup, the electron photo-gun and the charged-couple device (CCD) camera were all in the same high vacuum chamber. They used a homemade femtosecond laser at 620 nm (or 310 nm by use of a frequency doubler) to pump the gas molecules. Another optical setup was designed to convert a part of the 620 nm laser pulses to 258 nm to generate electrons. The electrons were generated by back illumination of a photo-cathode that was a 25 nm layer of gold deposited on a glass disk and kept at -15 kV to accelerate the electrons. A series of electrostatic lenses with an electrostatic deflector were used to focus and direct the beam to the sample. The electrons were detected directly by a CCD camera in the direct electron bombardment mode. The photo-electron pulses had the same duration as the laser pulse on the surface of the photo-cathode. But as the electron pulses left the cathode, the space charge effect increased their duration in traveling to the target. The number of electrons were kept low (under 10,000) to minimize that effect. With the repetition rate of 30 Hz, the average beam current was lower than 100 fA. More details on the setup are provided in [50].

The proximity of the electron gun and the gas source made their first UED setup prone to arcing, and inspired them to develop their second generation UED setup [51]. In 1997, the Zewail group introduced their second generation UED setup: UED-2 [52]. In that design, the electron gun, the scattering site, and the detector were in three different and differentially pumped chambers with small apertures between them. The schematic of UED-2 is shown in Figure 1.11. Beside using three chambers instead of one, the diffraction pattern was now detected by

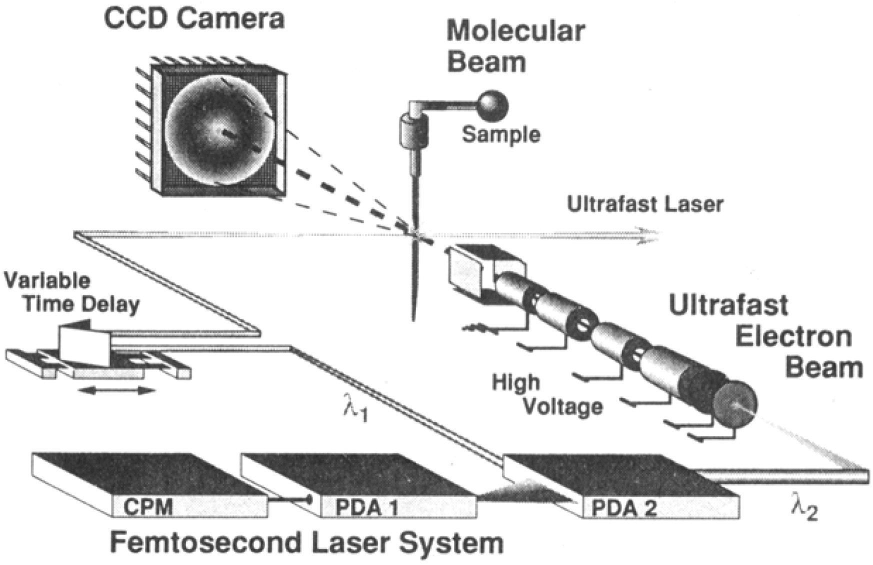

Figure 1.10: Schematic of the first UED setup. The homemade laser setup, composed of a colliding-pulse mode-locked (CPM) ring dye laser and a four stage pulse dye amplifier (PDA), was used to generate 620 nm, 60 fs, 0.3-0.5 mJ pulses at the repetition rate of 30 Hz. Part of the laser was converted to 258 nm to generate electrons in a photo-emission process and the rest of it was sent to the sample. This method introduced a minimum jitter between the pump and the probe. The timing between the excitation and probe was controlled by a moving stage. (Figure courtesy of [50]; used with permission.)

a phosphor scintillator together with an image intensifier connected to a CCD camera. With this configuration, they were able to detect a single electron hitting the phosphor screen. This produced diffraction patterns of higher quality. The new setup was a source of inspiration for other researchers in the field [53, 54]. In 2001, the Zewail's group revealed their third generation UED setup, dubbed UED-3. It was equipped with a time-of-flight spectrometry chamber. Also the phosphor screen was coated with a 500 nm layer of aluminum to filter out the laser photons without affecting the electrons. For this setup, the electron pulse duration could reach 1 ps for a significantly higher number of electrons per pulse in comparison to UED-2, due to a higher accelerating electric field (6 kV/mm in UED-3 vs. 2.7 kV/mm in UED-2) as well as a narrower photo-electron energy spread [51].

However, there were two barriers for reaching a femtosecond resolution for the setup. The first was the space charge effect: the number of electrons had

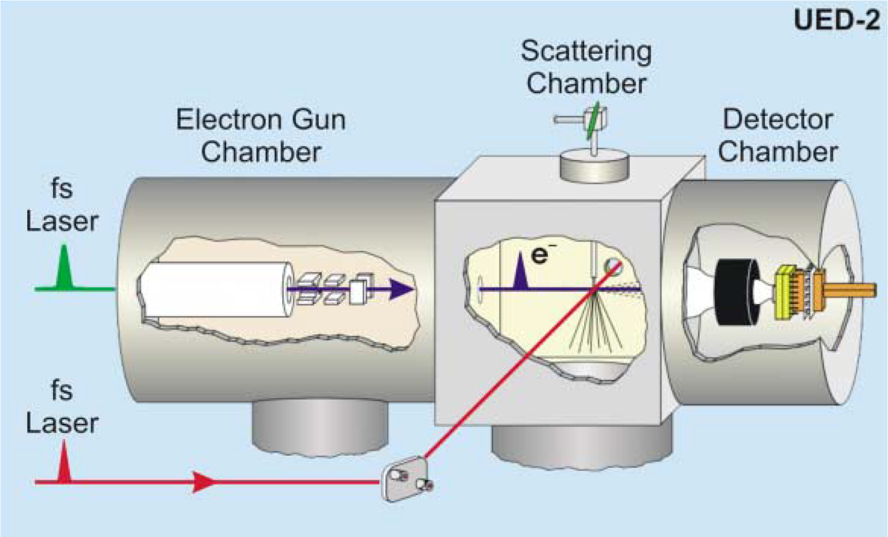

Figure 1.11: Schematic of UED-2 setup. (Figure courtesy of [51]; used with permission.)

to be kept low to prevent Coulomb expansion. This would in turn reduce the number of scattering events. It was also not possible to get the target close to the electron gun, in order to reduce the amount of pulse expansion, due to the arcing problem. One idea was to use relativistic electrons [55–57], which was implemented later [58]. However, this solution is limited to a few large facilities which can produce relativistic electrons. For table-top setups, it was suggested to compress the electrons in their path [59–61]. Radio-frequency electric field compression has been the most reported [62–65]. However, all UED experiments using radio-frequency compression were on condensed samples. We reported the first implementation of the radio-frequency compression technique for gas phase targets [66].

The other barrier was the pump-probe velocity mismatch. In 1993, Williamson and Zewail investigated the effect of velocity mismatch between the laser and the electrons, since the two do not propagate with same velocity unless the electrons are accelerated to velocities close to that of light [67]. This problem was solved later by the use of a laser front-tilting technique [68, 69]. We used the same technique to minimize the total temporal resolution of the setup.

This dissertation is organized in the following way to describe the gas phase

UED setup that we implemented: In Chapter 4, we explain the generation and compression of electrons in our setup, measurement of beam current, numerical simulation of the electron beam, the pump-probe velocity mismatch problem, and the laser intensity tilting technique. In Chapter 3, we review the electron pulse duration measurement by use of a homemade laser activated streak camera. Finally, in Chapter 4, we review the gas line, the setup calibration, the diffraction experiments and the temporal overlap of the pump and the probe.

Chapter 2

Table-Top High Current Ultrafast Gas Electron Diffraction Setup

2.1 Introduction

The major elements of a gas phase ultrafast electron diffraction experiment are: 1) electron pulses of femtosecond duration and high kinetic energy for temporally and spatially resolved observation, respectively; 2) ultrafast laser pulses to excite the sample under study; and 3) the target that is a gas jet coming out of a nozzle in the path of the electrons and the laser. In gas phase experiments, a typical density of the gas jet is around $10^{16} - 10^{17}$ atoms or molecules per cm^3 for small molecules and even lower for bigger molecules. A condensed sample has a typical density around 10^{23} atoms or molecules per cm^3. Usually the path length through a gas jet is about 1000 times that of a condensed sample, so there are about 10^3 to 10^4 fewer scattering events in gas phase experiments, with a concomitantly lower signal. Furthermore, if the condensed sample has a crystalline structure, the total diffraction signal will be a coherent superposition of diffraction signals from each of its cells (over the transverse coherence of the electron beam) and will be much brighter than the total diffraction signal from molecules in the gas phase, which is an incoherent superposition of diffraction signals from each molecule, since they are randomly spread. Therefore, in gas phase experiments, we need to increase the charge density of the electron pulses to compensate the low level diffraction signal. However, increasing the charge density, while maintain the pulse duration, is not feasible since the space charge expands the pulse size in all directions, resulting in a low temporal resolution, and a large transverse size of the beam. For relativistic electrons, the rest frame dynamics of the electron pulse are slower in the lab frame. Thus, for ultrafast photo-emitted relativistic electron pulses, no relevant dynamics is usually observed in the lab frame and consequently, the electron pulse preserves its temporal width between the source and the target. Successful ultrafast gas phase electron diffraction experiments have been reported which use relativistic electron pulses [58, 70–72]. For sub-relativistic electron pulses, however, we should either put the target close to the electron gun to reduce the travel time or use a device to temporally compress the electron pulse. Previous experiments have obtained a temporal resolution of between 850 fs and 1 ps when a 10 cm distance between the electron source was used (with only a few thousands of electrons per pulse) [53, 54, 73]. However, issues arise when one attempts distances shorter than this, as the gas density cannot be too high around the accelerating stage. Alternatively, the electron pulses can be recompressed by radio-frequency (RF) electric fields [59, 62, 63, 65, 74–77] or by static fields [61], and can therefore allow for the distance between the electron gun and the target to be increased, whilst keeping the number of electrons in the pulse in the order of 10^5. In our setup, we generate ultrafast electron pulses by femtosecond ultraviolet (UV) laser pulses in a photo-emission process, and accelerate them to 90 keV kinetic energy. Radio-frequency compression technology is then used to compensate the space charge broadening and temporally focus the beam on the target. There are magnetic lenses to compress the beam transversely and magnetic deflectors to guide the beam to the target. Sections 2.3, 2.4, 2.5 and 2.6 of this chapter will concentrate on these components of the electron gun, and provide insight into how the electron beam is manipulated. A simulation of the electron beam, as it passes through the apparatus, using General Particle Tracer, will be given in Section 2.7.

The other topic of this chapter is the pump laser preparation. Sub-relativistic electron pulses travel at velocities smaller than that of light leading to a discrepancy in the pump and probe timings, i.e. different parts of the sample will be excited and observed at different time intervals. Such mistiming depends on the size of the electron beam, laser beam and gas jet, as well as the angle between the pump and probe [67]. This problem will increase the overall temporal resolution of the experiment and will not be completely solved if we do not manipulate the laser beam such that its velocity matches the electrons velocity, by a technique called "laser front tilting" [68, 69]. In Section 2.8 we explain the mismatch velocity problem and its effect on the experiment and then provide details about the laser front tilting technique employed in our setup.

2.2 Overview of the experimental setup

In this section, we will give a brief review on the whole UED setup and its elements that are shown in Figure 2.1. In the next sections, we will provide more details on each part. Using this setup, we generate ultrafast laser and electron pulses to do pump-probe experiments on molecules in the gas phase. The beginning point of the setup is a Ti:Sapphire laser oscillator (Coherent, Mantis) that generates femtosecond laser pulses with a repetition rate of $\sim$75 MHz, a power of 400 mW, a central wavelength of 795 nm and a bandwidth of 60 nm. The output of the oscillator then goes to a laser amplifier (Coherent, Legend Elite Duo) to output 10 W, 5 KHz, 40 fs laser pulses with a central wavelength of 800 nm and a bandwidth of 30 nm. The amplifier output is split into three paths to generate the electrons, to pump the sample and to trigger the streak camera, a device that measures the electron pulse duration and timing. The streak camera will be the topic of Chapter 3.

The part of the laser that is used to generate electrons is first converted a UV wavelength by a frequency tripler and sent to a copper cathode to photo-emit the electrons. The cathode is held at -90 kV with respect to the grounded anode plate in front of it. The generated electrons will be accelerated electrostatically in the region between the cathode and anode, and leave that region through a small hole on the center of the anode plate. By use of two magnetic deflectors, the electron beam is centered and guided to the gas target and detector. The electron pulses

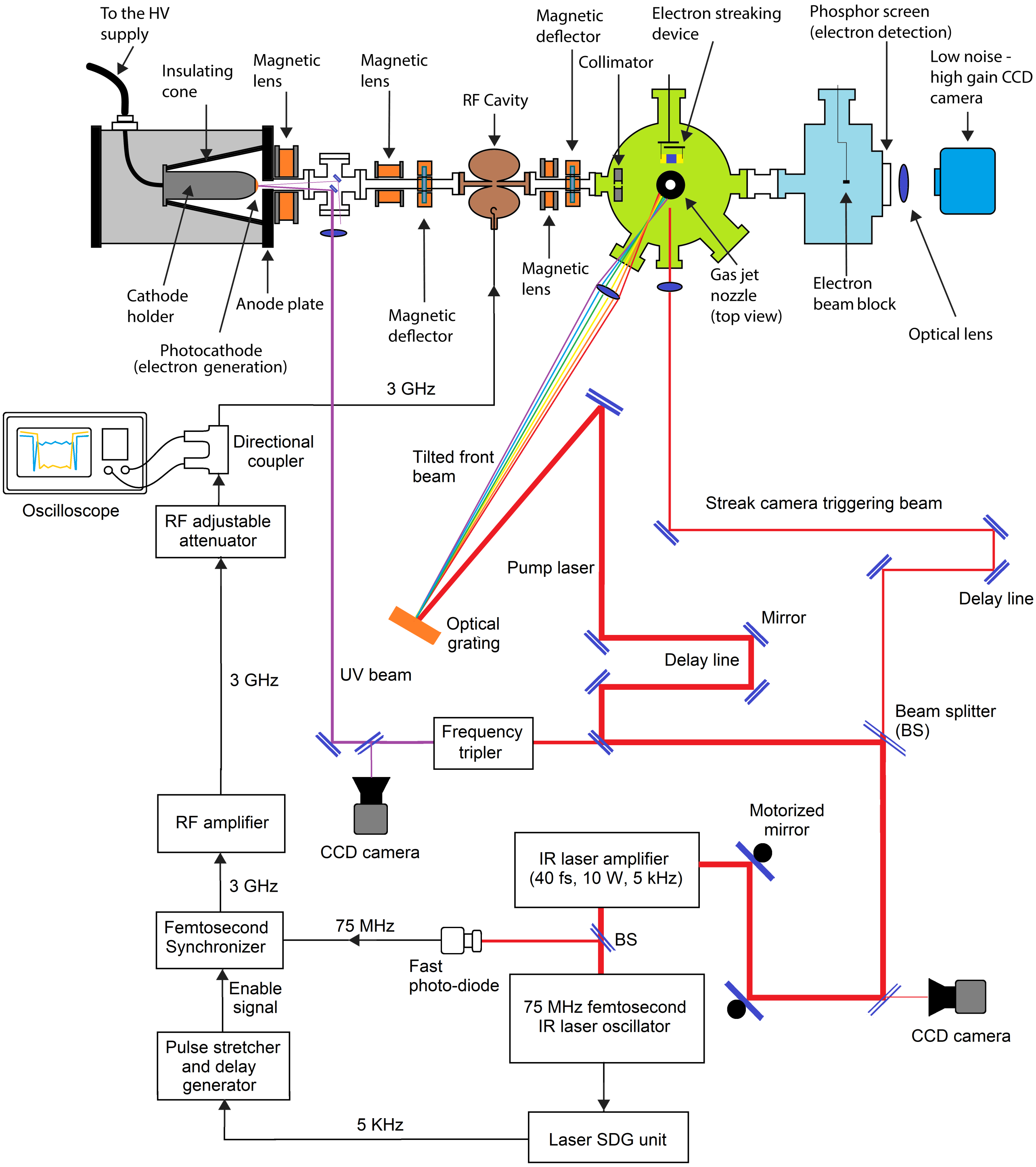

Figure 2.1: UED setup layout. (Adapted from Structural Dynamics, Vol. 4, 044022, (2017); used in accordance with the Creative Commons Attribution (CC BY) license.)

are compressed transversely by magnetic lenses and longitudinally by a ∼ 3 GHz microwave cavity whose compressing field is synchronized to the arrival time of electrons. The synchronization is done by a fast photo-diode that generates a ∼75 MHz electric signal by sampling the laser oscillator output and feeding it to a femtosecond synchronizer that generates the ∼3 GHz signal, which is amplified and fed to the cavity.

The other part of the laser is used to excite the sample under study and is referred to as the pump laser. We made an angle of 58.3° between the pump and probe so the laser velocity component in the direction of electrons motion have the same value as the speed of electrons. By use of an optical grating, we tilt the intensity front of a laser pulse to match the electrons.

2.3 Electron photo-gun

We generate electron pulses in a photo-emission process, by use of UV laser pulses. We accelerate the electrons in a static electric filed. In this section, we will review the optical setup used to generate the electrons, the high voltage chamber that accelerate the electrons and the way we measure the beam current.

2.3.1 UV laser setup

The ultraviolet laser pulses are generated from the infrared laser pulse by use of a frequency tripler setup shown in Figure 2.2. A beam splitter is used to separate off 10% of the laser amplifier output, which is sent to a frequency tripler, which consists of four optical crystals: 1) a BBO crystal that generates the second harmonic at 400 nm, from the 800 nm input laser; 2) a calcite group velocity delayer that overlaps the fundamental and second harmonics in time; 3) a zero-order wave plate (half-wave for 800 nm and full-wave for 400 nm laser) that rotates the polarization of the second harmonic to match it to that of the fundamental harmonic; and 4) a second BBO crystal that makes the third harmonic at 267 nm by combining the the fundamental and second harmonics. After these four crystals, we use three harmonic separators to filter the fundamental and second harmonics. Since a high intensity is needed in the BBO crystals to induce the nonlinear responses necessary for the harmonic generations, a telescope with a demagnification of 4 is used to make the IR beam intense enough. The IR beam has maximum fluence of 8.5 mJ/cm^2 on the first crystal.

The generated UV beam is first trimmed by a 400 μm pinhole and then truncated by a 200 μm pinhole, which is 10 cm away from the first pinhole. By this method, the beam would be uniform on the second pinhole in spite of fluctuations in the beam pointing, and has a smaller divergence in comparison to the case of using only one pinhole. There is an adjustable UV filter between the two pinholes to set the UV laser intensity for a desired number of photo-emitted electrons, and hence the beam current. The second pinhole is imaged onto the cathode surface by a demagnification of 4. By this method, we get a stable beam on the cathode, which is necessary to get a stable electron beam.

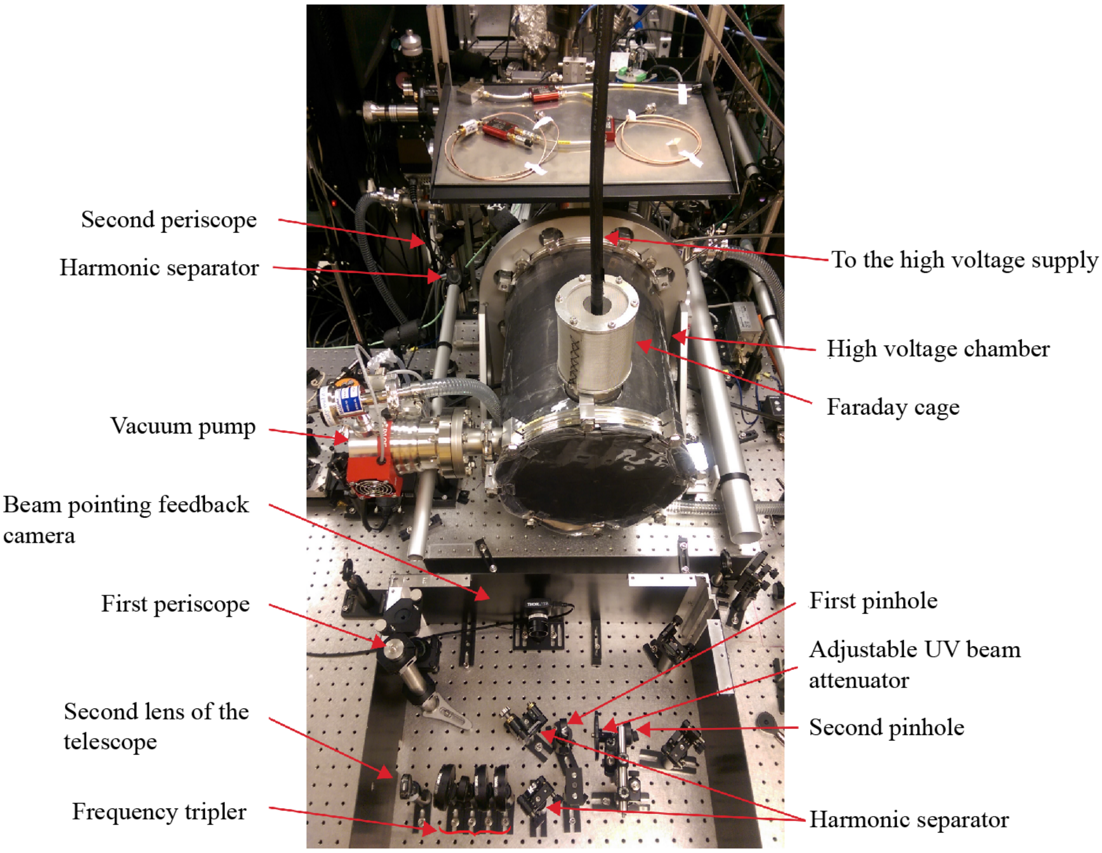

Figure 2.2: Optical setup for electron photo-emission.

2.3.2 High voltage chamber

Figure 2.3 shows the UV beam setup by which the electrons are created. By use of two periscopes, the beam is brought up to the center of the high voltage accelerator chamber. Then, the beam passes through a lens that images the second pinhole discussed in Section 2.3.1 to a photo-cathode by a demagnification of 4. The beam goes inside the vacuum chamber through a UV window and is guided to a photo-cathode by a mirror. The photo-cathode is made of pure copper with a work function of 4.7 eV. The energy of a 266.6 nm photon is 4.65 eV; therefore, one electron is released by absorbing one photon. The 50μm UV beam cannot be observed directly on the cathode. To make sure that the UV laser is hitting the center of the cathode, we first remove the imaging lens so the laser beam becomes large on the cathode. There is a small reflection from the surface of the cathode which is directed out by another mirror (see Figure 2.3). The cathode is made on a lathe with a flat center that has a diameter of $100\mu m$ so the grooves can be seen in the reflected beam. We change the beam pointing until the eccentric circles are observed in the reflected beam. At this point, electrons should be detected on the phosphor screen with all electron optics (the magnetic lenses and the RF cavity) being off except for the first electron beam deflector. We turn on the magnetic lenses to make the electron beam transversely small to avoid beam clipping. Then, we adjust the laser beam pointing to make the electron beam brightest and the most symmetric. Working with the reflection from the cathode is difficult since the beam is too dim and has a big divergence. However, there is another small reflection from the vacuum chamber window. After we were sure that the laser is hitting the center of the cathode, we put two distant pinholes centered on that reflected beam. The pinholes help to steer the laser beam to the center of the cathode quickly, in the case of any change in the UV beam pointing and loss of the electron beam. The beam steering is done mostly by the two mirrors on the second periscope. Once the laser pointing is fixed, we put the imaging lens back. The lens is mounted on a tube with one pinhole at each end. The aim of pinholes

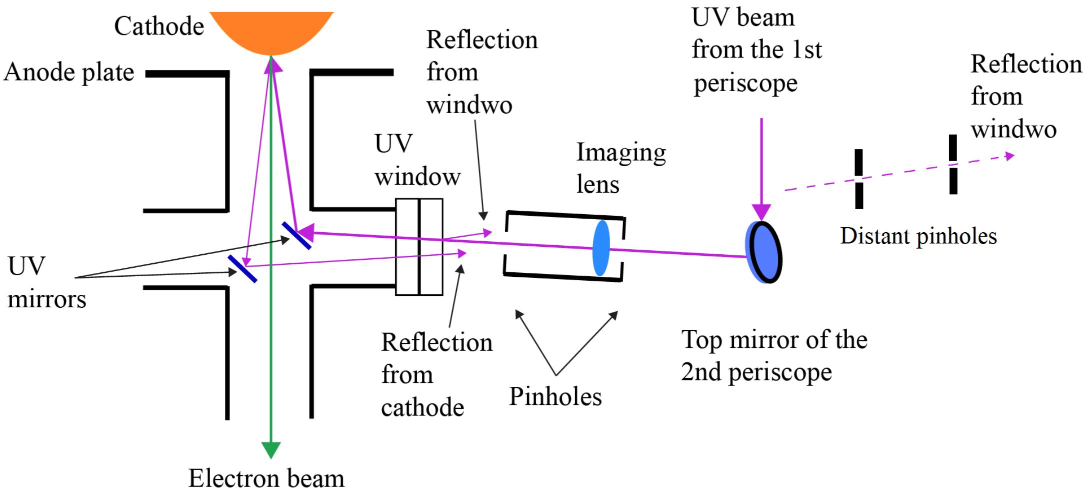

Figure 2.3: Electron pulse creation by illuminating the cathode by UV laser pulses.

is to mount the lens such that the UV beam is at its center and perpendicular to it to avoid aberrations and deflections. Both of the discussed reflections are blocked by the lens mount and cannot be used any more. However, only very small adjustments may be needed in the UV beam pointing to get the brightest and the most symmetric electron beam.

The schematic of the high voltage chamber is shown in Figure 2.4. The cathode is connected to a piece of metal that itself is held by an isolating cone. The cone is made of PEEK (Polyetheretherketone) and is designed to withstand voltages over 100 kV. The cathode is connected to a high voltage supply (Matsusada, AU-100N 1.5). We set the cathode at -90 kV as we found that at this voltage the chamber was the most stable regarding the number of breakdowns. The chamber was purchased from AccTec BV and more details about its structure and design can be found in [78]. The electrons are accelerated between the cathode and the anode plate, and they leave the acceleration stage through a 8 mm hole on the anode plate in front of the cathode tip. The distance between the cathode and the anode is around 1 cm resulting in an accelerating field of around $E_0 = 9$ MV/m. The shape of the cathode and anode is designed so that the electric filed is radially uniform in the acceleration region (around the cathode axis). An electron pulse that is generated by this technique has a profile of a uniformly charged spheroid

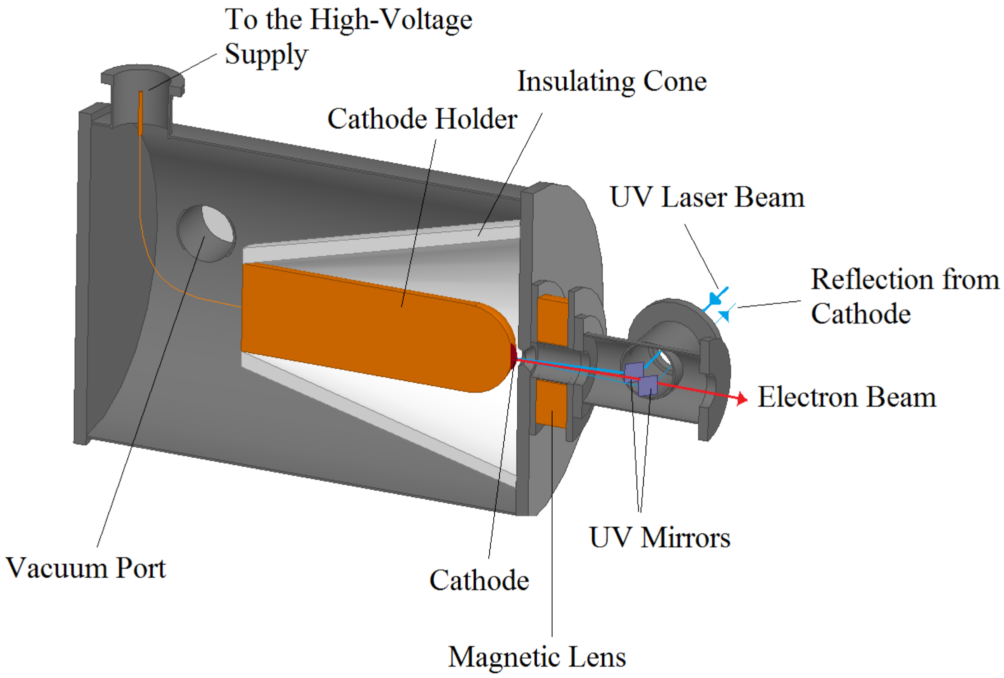

Figure 2.4: The high voltage chamber. The photo-created electrons are accelerated by the electric field across the cathode and anode. (Reproduced from [79].)

[80]. The idea comes from the fact that an oblate spheroid with a uniform mass density collapses into a disk under its own gravity force. Hence, if we generate a surface charge with a density of

$$\rho(r,z) \approx \sigma_0 \sqrt{1-\left(\frac{r}{b}\right)^2}\,\delta(z) \tag{2.1}$$

on the surface of the cathode (z=0), where σ_0 is the surface charge density at the center of the pulse and b is the lateral semiaxis and $r = \sqrt{x^2+y^2}$, it will evolve into a uniformly charged spheroid because of the linear Coulomb repulsion force inside the bunch [80]. The approximation sign is used since in reality the beam has some initial thickness that comes from the laser pulse duration τ and that thickness is necessary since a two dimensional object will not evolve into a three dimensional object. However, that finite creation time as well as the image charge on the cathode surface prevent the linear force inside the bunch that is essential for obtaining a uniformly charged spheroid. The condition for which a uniform spheroid charge distribution evolves from equation (2.1) in spite of the image charge force and the finite creation time is given by [80]

$$\frac{eE_0\tau_l}{m_e c} \ll \frac{\sigma_0}{\epsilon_0 E_0} \ll 1 \tag{2.2}$$

for $m_e = 9.11 \times 10^{-31}$kg the electron mass, $e = 1.6 \times 10^{-19}$C the electron charge, E_0=9 MV/m the accelerating field, $c = 3 \times 10^8$m/s the light velocity in vacuum, $\tau_l = 100$ fs the laser pulse duration, and $\epsilon_0 = 8.85 \times 10^{-12}$ F/m the permittivity of vacuum. For a 16 fC electron pulse (a pulse of 10^5 electrons) with a radius of $b = 25\mu$m, we will have $\frac{eE_0\tau_l}{m_e c} = 5.3 \times 10^{-6}$ and $\frac{\sigma_0}{\epsilon_0 E_0} = 0.1$, which fulfill the condition. The UV beam truncation by the pinhole that we described above results in an electron beam distribution very close to equation (2.1). Consequently, the electron pulse will be a uniformly charged spheroid. For the spheroid pulse with a longitudinal semi-axis a and transverse semi-axis b, the electrostatic potential inside the bunch in its rest frame and measured from the bunch center is [81]

$$\phi(r,z) = -\frac{3Q}{16\pi\epsilon_0}\int_0^\infty ds \frac{\frac{z^2}{a^2+s} + \frac{r^2}{b^2+s}}{(b^2+s)\sqrt{a^2+s}} = -\frac{3Q}{16\pi\epsilon_0 a^3}(C_z z^2 + C_r r^2), \tag{2.3}$$

where $-Q$ is the total charge of the pulse, and C_r and C_z are two constants that depend only on the ratio b/a:

$$C_z = \int_0^\infty \frac{ds}{[(\frac{b}{a})^2 + s][1+s]^{\frac{3}{2}}}; \quad C_r = \int_0^\infty \frac{ds}{[(\frac{b}{a})^2 + s]^2[1+s]^{\frac{1}{2}}}. \tag{2.4}$$

Figure 2.5 shows the value of C_z and C_r as functions of b/a obtained numerically [79]. The resultant electric field of the pulse inside the bunch will be

$$\vec{E}(r,z) = -\nabla\phi(r,z) = \frac{3Q}{8\pi\epsilon_0 a^3}[C_z z\hat{z} + C_r r\hat{r}). \tag{2.5}$$

The Coulomb force inside such pulses is linear with respect to the distance from the pulse center. Equation (2.5) gives the electric field at one time instant where generally the force is not equal in $\hat{r}$ and $\hat{z}$ directions; therefore, the aspect ratio b/a changes and subsequently do C_r and C_z. However, the force remains linear

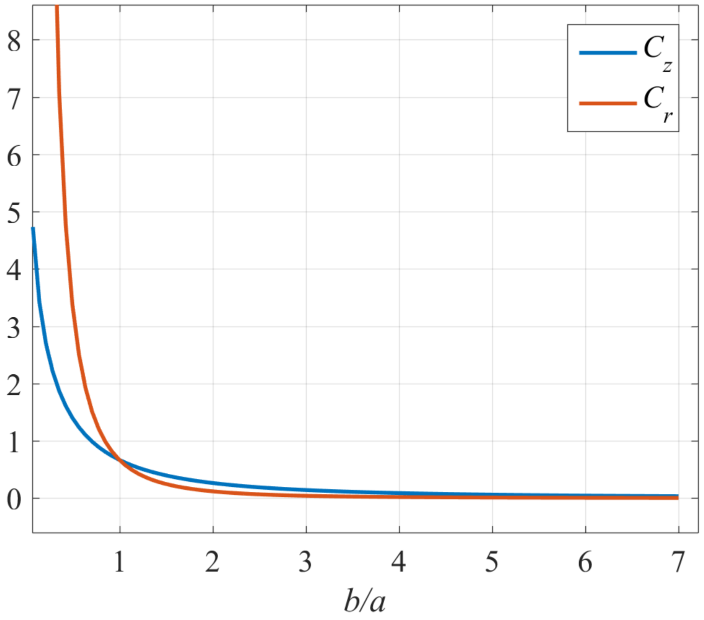

Figure 2.5: C_r and C_z in equation (2.4) as functions of the aspect ratio b/a of a uniformly charged spheroid. (Reproduced from [79].)

and consequently the charge distribution remains a uniformly charge spheroid, in spite of changes in the aspect ratio. The main outcome of this property is that we can reversibly compress the electron pulse in both directions by use of linear forces without changing its spheroid profile. In other words, we can theoretically compress such a pulse to its original dimensions at the cathode by use of linear forces. The detail of temporal evolution of such pulses in their rest frame can be found in [82].

2.3.3 Beam current measurement

We measured the electron beam current by use of a homemade copper Faraday cup as seen in figures 2.6a and 2.6b. The cup contains a recess that is ten times longer than its opening diameter, with a curved end to minimize electron back scattering. To measure the beam current, we focused the electron beam using magnetic lenses (discussed in detail in Section 2.5), on the Faraday cup entrance. The Faraday cup is connected to a picoameter (Keithley, 6485) through a vacuum feedthrough and a low noise coaxial cable [83]. Figure 2.7 shows the number of electrons in each pulse for a given UV laser power. That number almost linearly

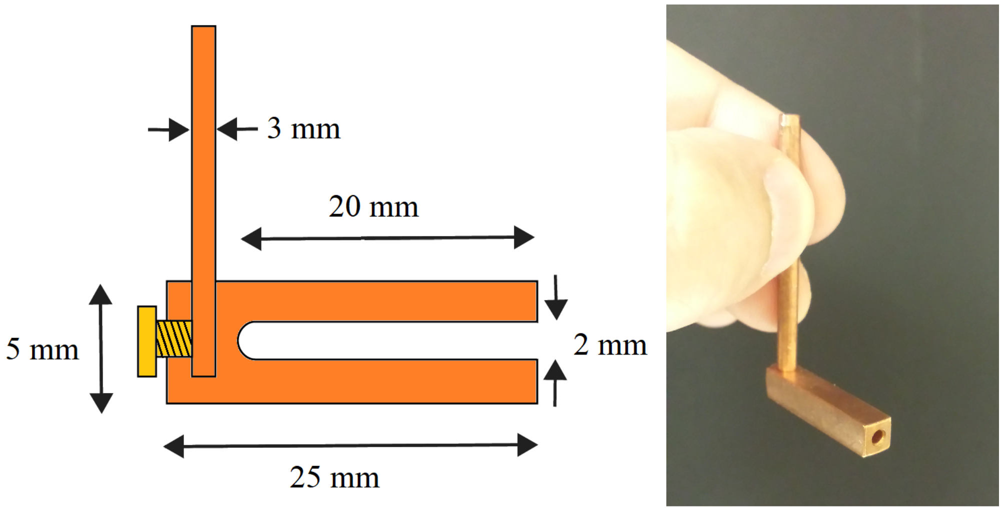

(a) (b)

Figure 2.6: (a) Faraday cup dimension (b) Photograph of the Faraday cup.

increases with the laser energy as is expected for a one-photon photo-emission.

2.4 Electron pulse deflection

As is shown in Figure 2.1, we use two magnetic deflectors, one commercial and one homemade, to guide the electrons and keep the beam centered on different components, such as the magnetic lenses and the RF cavity. Each deflector is composed of two pairs of coils sitting on the sides of a square magnetic core. Each pair of coils are on opposite sides of the square and generate equal magnetic field in the same direction at the center of the square core and deflects the electrons that are going through that center. In Figure 2.8, one pair of coils is shown that can deflect electrons moving on the z-axis along the $\hat{y}$ direction. For a small angle of deflection Θ, we have

$$\tan\Theta = \frac{p_y}{p_z} \approx \frac{2ev_zB_x\Delta t}{m_e\gamma v_z} = \frac{2eB_xl}{m_e\gamma v_z}, \tag{2.6}$$

where, e and m_e are the charge and mass of an electron, respectively, p_y is the momentum that the electrons with longitudinal velocity v_z and momentum p_z gain in the y direction due to the Lorentz magnetic force, Δt is the time the electrons spend in the field region, l is the length of the field region and is approximately

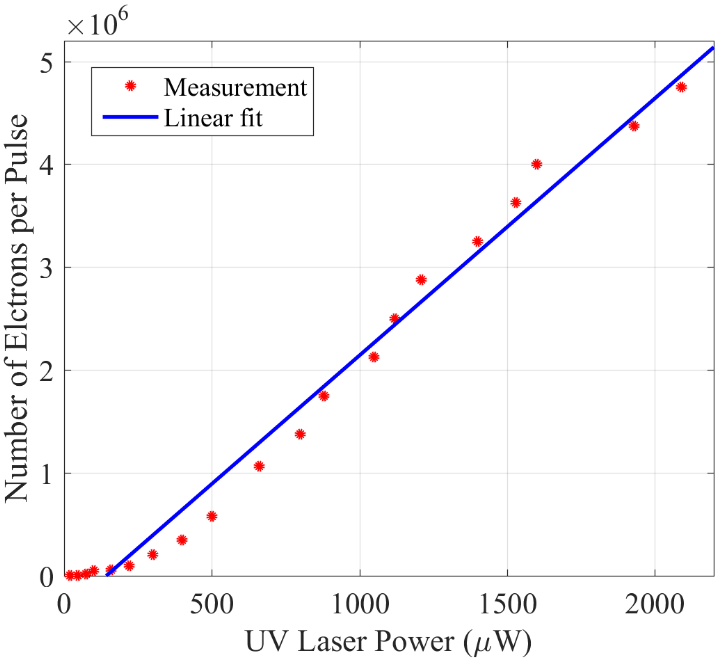

Figure 2.7: Number of electrons per pulse vs the UV laser power. The red dots show the measured values and the blue line a linear fit to the points. (Reproduced from [83].)

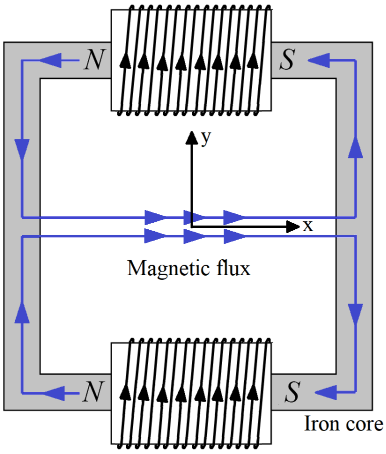

Figure 2.8: Magnetic field of a pair of coils sitting on a magnetic square core. An electron beam moving toward the plane of the page and through the center of the square core will be deflected upward. With another pair of coils on the other sides of the square, the electrons can be deflected horizontally.

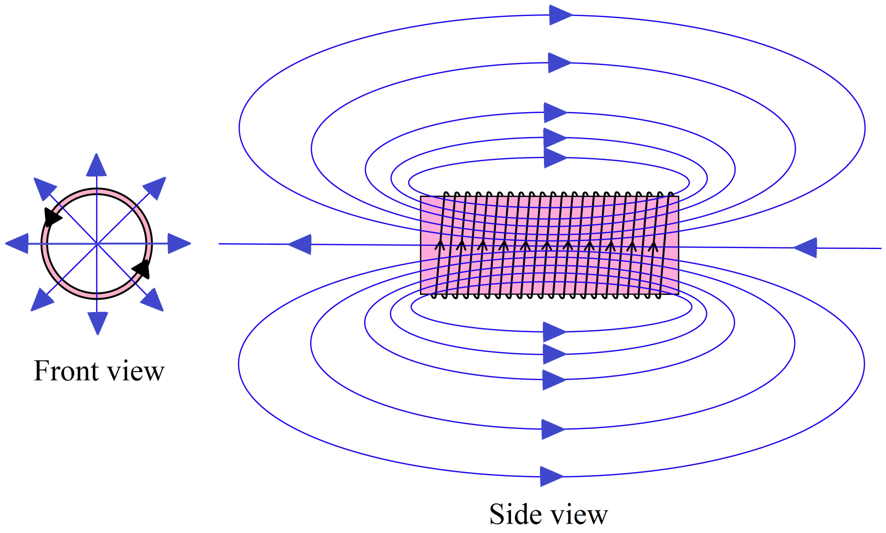

Figure 2.9: A magnetic lens is a coil whose field transversely compress the electrons.

equal to the magnetic core thickness, γ is the relativistic gamma factor, and B is the magnetic field produced by one of the coils. For example, for a deflection of $\Theta = 2^{\text{o}}$, and $l = 1$cm each coil should produce a magnetic field of $B_x = 1.8$mT, which is feasible for a 100 turn coil with a length of 5 cm and a diameter of 3.9 cm, an iron core and a current in the order of 100 mA.

2.5 Transverse compression of the electron pulses: Magnetic lenses

We control the transverse size of the electron beam by three magnetic lenses that are shown in Figure 2.1. Each magnetic lens is a coil through which the electrons traverse. As is shown in Figure 2.9, at the entrance of each coil, the magnetic field has a radial component that exerts an azimuthal force on the electron bunch so it starts to rotate around the coil axis. Inside the coil, the magnetic field is along the coil axis and exerts an inward radial force to the electrons and hence compresses them transversely. Note that the electrons will not have a net azimuthal velocity after the lens, since the radial forces at the entrance and exit of the coil cancel the effect of each other; however, the electron pulse will be rotated azimuthally with the same amount for each electron, neglecting the momentum spread of the pulse. The equation of motion of an electron inside a paraxial electron pulse at the radial distance r is

$$\gamma m_e \frac{dv_r}{dt} = -ev_\phi B_z + \frac{\gamma m_e v_\phi^2}{r} + \frac{3Q}{8\pi\epsilon_0 a(t)^3} C_r(t) r, \tag{2.7}$$

where v_r is the radial velocity of the electron and v_ϕ is the azimuthal velocity that it gained at the entrance of the coil and B_z is the axial magnetic field which is assumed uniform in the radial direction. The first, second and third terms on the righ-hand-side of equation (2.7) show the Lorentz force on the electron in a magnetic filed, the relativistic centripetal force because of the electron azimuthal velocity, and a radial force due to the space charge effect in equation (2.5), respectively.

From the conservation of angular momentum, it can be shown that [84]

$$v_\phi = \frac{erB_z}{2\gamma m_e}. \tag{2.8}$$

By inserting equation (2.8) into equation (2.7) we get

$$\frac{d^2 r}{dt^2} = \left\{ -\frac{eB_z}{2\gamma m_e} + \frac{3Q}{8\pi\epsilon_0 a(t)^3 \gamma m_e} C_r(t) \right\} r. \tag{2.9}$$

This equation shows that by a large enough value of B_z, we can overcome the space charge effect and radially compress the pulse. Note that the compressing force is linear so the electron pulse retains its spheroid profile. Finding the focus point from equation(2.9) is not straightforward because $a(t)$ and $C_r(t)$ are functions of time. However, by ignoring the space charge effect, the focus point can be easily obtained [84].

In our setup, we used three magnetic lenses to make the beam size small on the compressing RF cavity, at the target and at the detector. The coils are depicted in Figure 2.1 and their parameters are summarized in Table 2.1. The RF electric field, which we use to longitudinally compress the electron pulses, diverges the beam transversely. The aim of the third coil that is placed after the RF cavity is

Table 2.1: Parameters of three magnetic lenses

	Coil 1	Coil 2	Coil 3
Inner diameter (mm)	85	40	43
Outer diameter (mm)	140	70	94
Length (mm)	60	60	25
Number of turns	360	935	216
Distance from cathode (mm)	43.9	275	650
Current range (A)	7.5–8.5	1.2–1.3	1–3
Axial magnetic field (mT)	~ 60	~ 20	~ 10

to compensate that effect.

After all the electron optics and around 10 cm before the target position, we use a an electron collimator with a diameter of 400 μm to cut the stray electrons and to give the most symmetric beam profile.

2.5.1 Transverse profile of the electron beam

By use of magnetic coils, we have a control over the beam transverse radius at different positions. The beam size can be measured on the detector directly. If the electron pulses are uniformly charged spheroids with the transverse semi-axes b_s, the detected intensity on the phosphor screen at (x, y) plane, $A_s(x, y)$, will be

$$A_s(x,y) = A_s\sqrt{1 - \frac{(x-x_0)^2 + (y-y0)^2}{b_s^2}}, \tag{2.10}$$

where (x_0, y_0) is the center of the beam on the detector, A_s is a constant and we have ignored the finite resolution of the detector that can blur the signal. On the other hand, if the beam has a Gaussian profile on the detector with a radial standard deviations of σ_r, the detected signal on the phosphor screen will be

$$A_g(x,y) = A_g \exp^{-\frac{(x-x_0)^2+(y-y0)^2}{2\sigma_r^2}}, \tag{2.11}$$

where A_g is a constant. Figures 2.10a, 2.10b and 2.10c show the detected electron beam on the CCD camera, and its projection onto the x and y axes, respectively. We fitted a Gaussian and spheroid functions to the measured profiles. The spheroid functions had slightly less fitting errors in both directions. The standard deviation of the Gaussian fit was 20.11 and 19.4 pixels in x and y directions, corresponding to around 860 μm and 850 μm on the phosphor screen, respectively. The full width half maximum (FWHM) of the beam is around 2 mm in both directions. The standard deviation for the spheroid fit is equal to $b_s/\sqrt{5}$ and is equal to 17.4 and 16.8 pixels in x and y directions, respectively.

At the target (or anywhere else in the beam line), the transverse size of the beam can be measured indirectly by first blocking the beam completely by a grounded conductor plate and then gradually unblocking it from one side (for instance, moving the plate away in x direction while z is the direction of propagation) and measuring the beam current by the Faraday cup. If the beam has a spheroid profile with b_t the transverse semi-axes, the current we read as a function of the blocking plate position will be of the form

$$I(x) = \begin{cases} 0, & x \leq -b_t \\ I_0(x + \frac{2b_t}{3} - \frac{x^3}{3b_t^2}), & -b_t < x < b_t \\ I_0, & x \geq b_t, \end{cases} \tag{2.12}$$

which comes from integration of the spheroid and I_0 is the total beam current. On the other hand, if the beam has a Gaussian profile with the standard deviation of σ_b, the current will be

$$I(x) = I_0(1 + \operatorname{erf}(\frac{x}{\sqrt{2}\sigma_b})). \tag{2.13}$$

Figure 2.11 shows the measured current as a thin foil of copper intruding the beam. The two functions in equations (2.12) and (2.13) are fitted to the measurement with almost the same fitting error. The standard deviation of the Gaussian fit is 130 μm corresponding to the FWHM of 306 μm, the standard deviation of the spheroid fit was 120 μm.

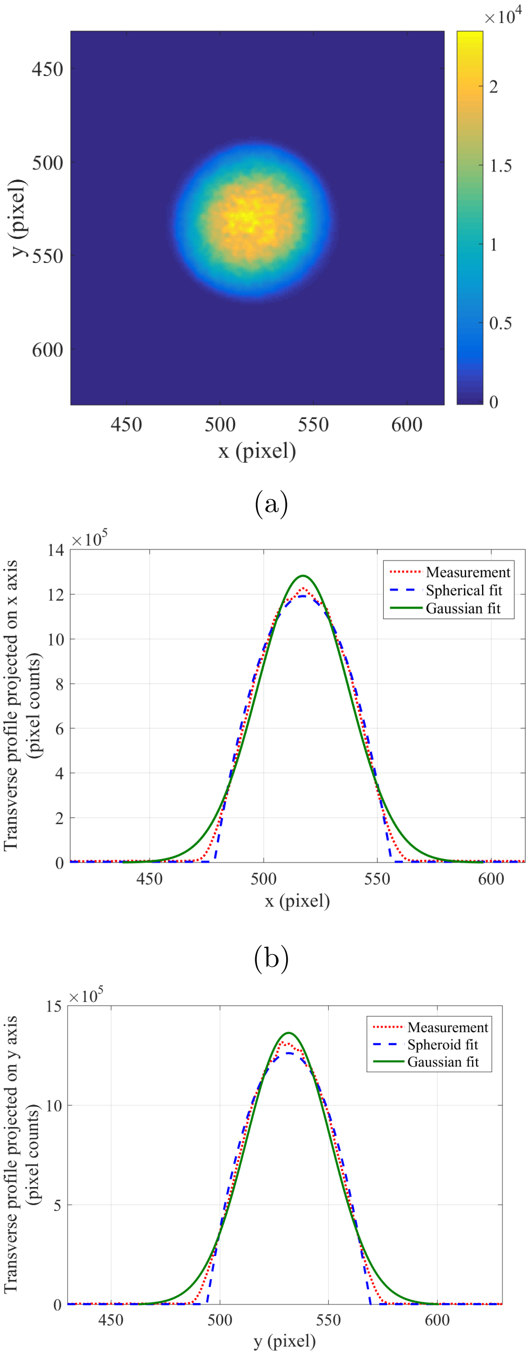

(a)

(b)

(c)

Figure 2.10: (a) The electron beam on a phosphor screen as detected by a CCD camera. (b) the projection of the beam onto the x axis (c) the projection of the beam onto the y-axis. For both one dimensional plots, we fitted a Gaussian and spheroid profiles onto the measured data.

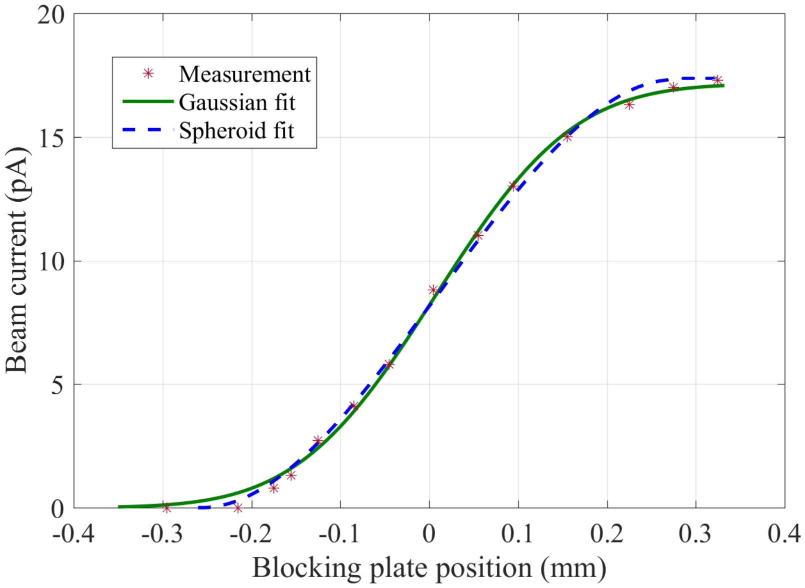

Figure 2.11: Measurement of the electron beam transverse size. We read the beam current while a copper foil intruded the beam in x direction. Functions in equations (2.12) and (2.13) are fitted to the data points.

2.6 Longitudinal compression of the electron pulses: RF cavity

Unlike the transverse compression of electrons by time-invariant magnetic fields, the electrons are compressed by a time-varying electric field of an RF cavity that is precisely synchronized to the electrons. In this section, we first review the compression mechanism, and then the synchronization.

2.6.1 RF compression of electron pulses

The electron pulses can be compressed using the time-varying longitudinal electric field of a microwave cylindrical cavity in its TM_{010} mode, with the electric field

$$\vec{E}_c(r,t) = E_0 J_0(\frac{x_{01}}{R} r)\cos(\omega_0 t)\hat{z}, \tag{2.14a}$$

and magnetic field

$$\vec{B}_c(r,t) = \frac{E_0}{c} J_1(\frac{x_{01}}{R} r)\sin(\omega_0 t)\hat{\phi}, \tag{2.14b}$$

where E_0 is the amplitude of oscillation, J_0 and J_1 are the zero and first order Bessel functions of first type, respectively, x_{01} is the first zero of J_0, R is the radius of the cavity and ω_0 is the resonance angular frequency of the cavity [85]. If the electron beam is transversely much smaller than the radius of the cavity such that $r/R \to 0$, then

$$J_0(\frac{x_{01}}{R}r \to 0) \to 1; \quad J_1(\frac{x_{01}}{R}r \to 0) \to \frac{1}{2}\frac{x_{01}}{R}r. \tag{2.15}$$

Therefore, the cavity fields become

$$\vec{E}_c(r \ll R, t) \approx E_0 \cos(\omega_0 t)\hat{z}, \tag{2.16a}$$

and

$$\vec{B}_c(r \ll R, t) \approx \frac{E_0}{c}\frac{1}{2}\frac{x_{01}}{R}r \sin(\omega_0 t)\hat{\phi}. \tag{2.16b}$$

Suppose that the length of the cavity l_{cavity} is such that

$$\frac{l_{cavity}}{v_z} \ll \frac{2\pi}{\omega_0}, \tag{2.17}$$

for v_z the velocity of electrons, so the time the electron pulse spends inside the RF cavity is much shorter than its field oscillation period. Around time t_0 for which $\omega_0 t_0 = \pi/2$, the field of the cavity can be approximated by

$$\vec{E}_c(r \ll R, t \to t_0) \approx -E_0\omega_0(t - t_0)\hat{z}, \tag{2.18a}$$

and

$$\vec{B}_c(r \ll R, t \to t_0) \approx \frac{E_0}{c}\frac{1}{2}\frac{x_{01}}{R}r(1 - \frac{(\omega_0(t - t0))^2}{2})\hat{\phi}. \tag{2.18b}$$

For an electric field amplitude in the order of 1 MV/m, the amplitude of the magnetic field will be around few mT for $r = R/10$, and will diverge an electron beam whose transverse size is relatively large, since it applies an outward radial force

$$\vec{F}_B(r, t) \approx ev_z\frac{E_0}{c}\frac{1}{2}\frac{x_{01}}{R}r(1 - \frac{(\omega_0(t - t0))^2}{2})\hat{r} \tag{2.19}$$

to an electron at r. Therefore, by making the electron beam big enough on the cavity, we can set the phase of the RF cavity at a value for which the beam is biggest on the detector. By this technique, we send the electrons to the cavity around time t_0 where the electric field in equation (2.18a) is crossing zero from positive values to negative values. Then, making the beam transverse size smaller on the cavity by use of the magnetic lenses will not change the arrival time of electrons since magnetic fields cannot change the energy of the beam.

For an electron pulse moving along the $+z$ direction, the electric field in equation (2.18a) applies a force that is in the $-z$ direction while the pulse is entering the cavity and linearly increases by time so that it is in the $+z$ direction while the pulse is exiting the cavity. This time-varying electric field compresses the electron bunch in time, i.e. the electron pulse goes to a focus after the RF cavity. The RF cavity was purchased from AccTec BV and its shape was optimized for highest axial electric field and quality factor. Figure 2.12a shows a cylindrical RF cavity and Figure 2.12b shows its geometrically optimized version. As a general rule, if one modifies the shape of an RF cavity so that the ratio of its volume over its boundary surface increases for a a given cutoff frequency, the quality factor increases because the ratio of stored energy in the cavity over the dissipated energy on the cavity walls increases. Figure 2.12c illustrates the timing between the RF cavity electric field and the electron pulse for an optimum compression.

Suppose z_c and v_z represent the center of the electron beam and its velocity, respectively. If the center of the electron pulse traverses the center of RF cavity at time t_0, no force would be applied to it, so it retains its longitudinal velocity. The total longitudinal force on an electron at z, by including the space charge electric field in equation (2.5) will be [79]

$$F_z(z) = -eE_0\omega_0\frac{z-z_c}{v_z} + \frac{3eQ}{8\pi\epsilon_0 a^3}C_z(z-z_c) = \left\{ -eE_0\frac{\omega_0}{v_z} + \frac{3eQ}{8\pi\epsilon_0 a^3}C_z \right\}(z-z_c). \tag{2.20}$$

As we see, for large enough values of $E_0\omega_0$, not only the space charge effect can

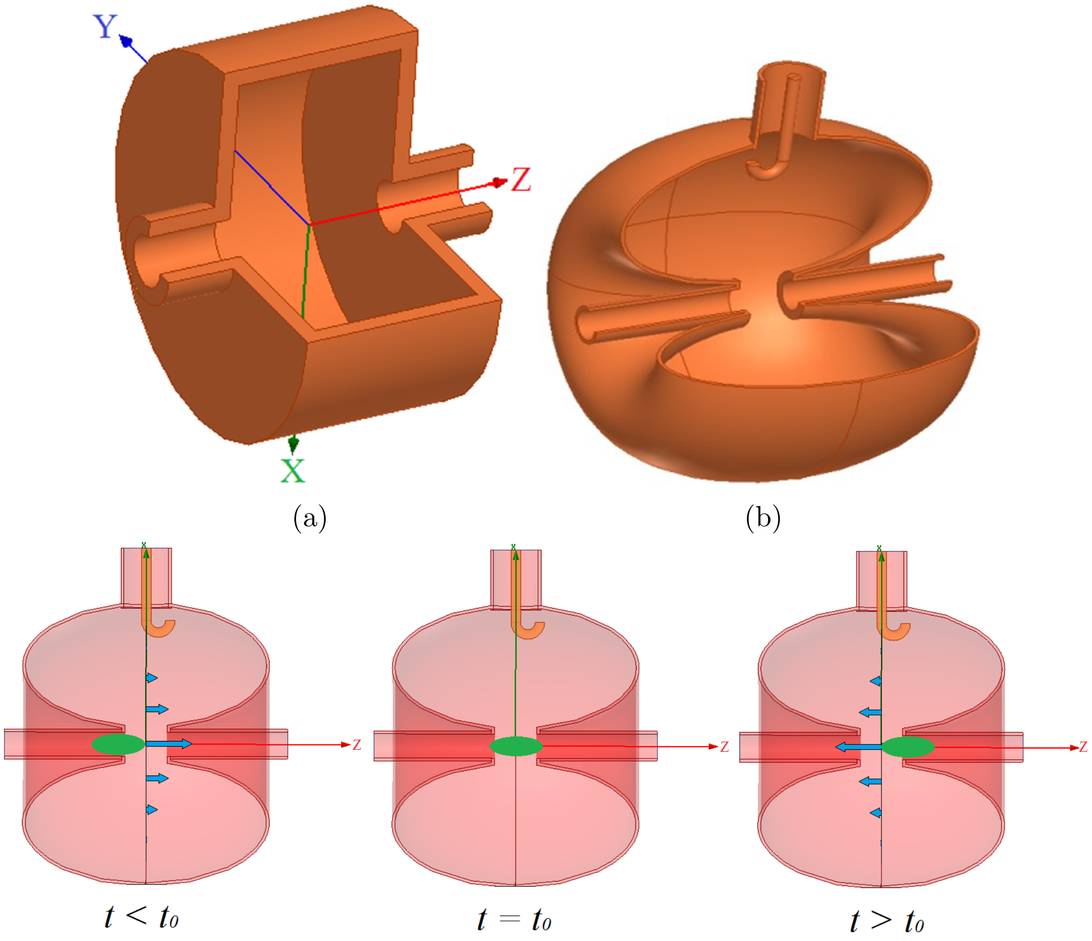

(a) (b)

(c)

Figure 2.12: (a) A cut of a cylindrical RF cavity; the electron pulses travel along +z direction and go inside the cavity through a hole with a diameter much shorter than the oscillation wavelength so it minimally disturbs the fields patterns (b) The geometrically optimized RF cavity for higher quality factor and axial electric field. (c) Timing between the cavity electric field and the electrons . Blue arrows show the electric field. (Reproduced from [79].)

be compensated but the pulse can be longitudinally compressed and focused on a target. Calculation of the temporal focal length of the cavity is not straightforward because of the space charge effect; however, by ignoring the space charge, the focus point can be obtained analytically in a closed form [86].

Unfortunately, the first mode of the RF cavity is TE_{110} and not TM_{010}. Therefore, the RF cavity feed antenna had to be designed so it coupled most of the input power to TM_{010} [78].

2.6.2 Electrons-RF field synchronization and timing

The bottleneck of aneffective electron pulse compression is a precise timing between the arrival of the electrons and the phase of the compressing electric field. In our setup, we use a commercial synchronizer (AccTec BV) that adjusts the phase of the RF cavity electric field within 100 fs with respect to the arrival of the electrons. The laser oscillator acts like a clock for the whole system, i.e., the electrons and the pump laser are synchronized to the oscillator output. Therefore, the idea was to synchronize the RF cavity fields to the laser oscillator too [87]. At the output of the laser oscillator, there is a 10% beam sampler that directs the beam to a fast photo-diode, the output of which goes to the commercial synchronizer where an RF signal with a frequency 40 times larger than the input is generated. The phase of the output signal is locked to the phase of the input signal. The resonance frequency of the RF cavity is 2.997 GHz at 45^o, corresponding to the laser repetition rate of 74.935 MHz. The quality factor of the RF cavity is around 10,000, resulting in a bandwidth of 300 kHz. So the repetition rate of the laser oscillator should be within the range of 74.931 to 74.939 MHz. We motorized one of the laser oscillator end mirrors, so we can change the repetition rate and monitor it. There is an active feedback loop that corrects the repetition rate in case of any drift [83]. Furthermore, we replaced the pump laser of the oscillator with another pump laser (Lighthouse Photonics, Sprout-H) with a significantly better nominal optical noise. Amplitude noise in the laser output causes amplitude noise in the electric field signal read by the fast photo-diode and translates into a phase jitter at the synchronizer output. Figure 2.13 shows the laser oscillator and the modifications we did. Any change in the RF cavity temprature changes its dimensions and hence its resonance frequency. This can introduce a change in the phase of its oscillating field. The duty cycle of the RF cavity field is reduced to 5% for a better temperature stabilization. So for a the setup repetition rate of 5 kHz, the RF cavity is on only for 10 μs. By a commercial temperature controller (AccTec BV), the RF cavity temperature is stabilized within 1 mK.

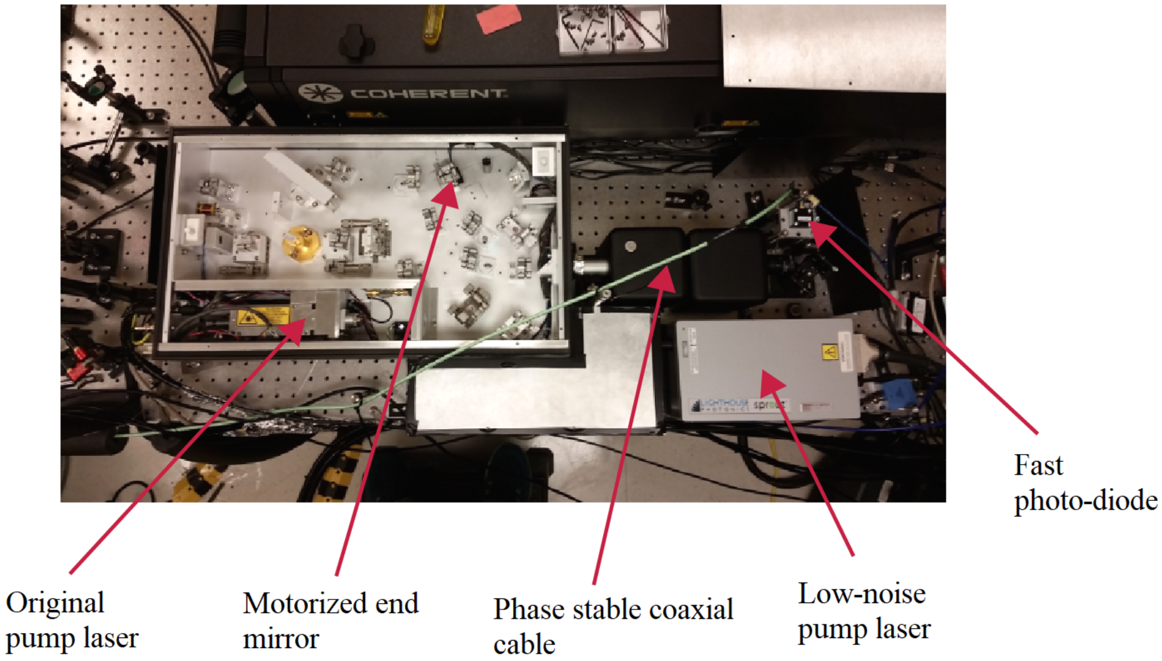

Figure 2.13: Laser oscillator setup.

The signal from the synchronizer goes to a custom-designed adjustable RF 0-10 dB attenuator (RLC electronics) and to a solid-state 53 dB amplifier (Microwave amps, AM83-3S-50-53R). The amplified signal goes to a 30 dB directional coupler (Meca Electronics, 722N-30-3.100) and then to the RF cavity. The directional coupler takes samples from the RF cavity input and reflection signals and sends them to RF power detectors (Mini-Circuits, ZX47-40LN) by which we monitor the input power to and the reflection from the RF cavity. Figure 2.14 shows all the described elements. Figure 2.15a shows the signal detected by the power detectors on an oscilloscope. In the experiment, we moved the end mirror of the laser oscillator so that the reflection from the cavity becomes minimum. According to the data sheets of the power detectors, the conversion from the detected voltage by the oscilloscope, v to the actual power P in dBm is

$$P = -40.54 \times v + 39.86; \tag{2.21}$$

therefore, the reflection signal observed on the oscilloscope should be maximum. Figure 2.15b represents the input power and the reflection power in Watts. We used phase stable coaxial cables (Times Microwave Systems, PT210) to connect the RF devices for the lowest phase jitter. The details of determining the input power and the phase value of the RF cavity for optimum longitudinal compression are discussed in the next chapter, where we describe the electron pulse duration measurement.

The noise peak in the input power is due to the Pockels cells switching in the laser amplifier and is an approximate indicator of the time the electrons enter the RF cavity. The rise time of the RF cavity is around 6μs. We made a pulse stretcher and delayer device that enables the RF cavity fields such that the electrons enter the cavity after its rise time. The details of the circuit is provided in Appendix A.

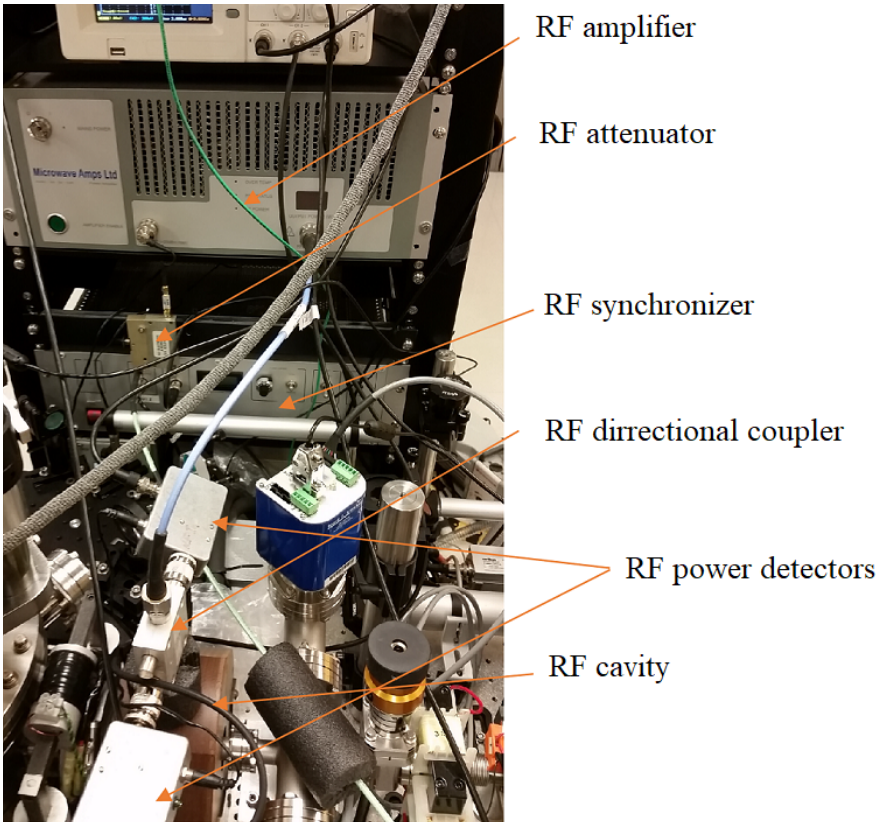

Figure 2.14: RF cavity setup elements.

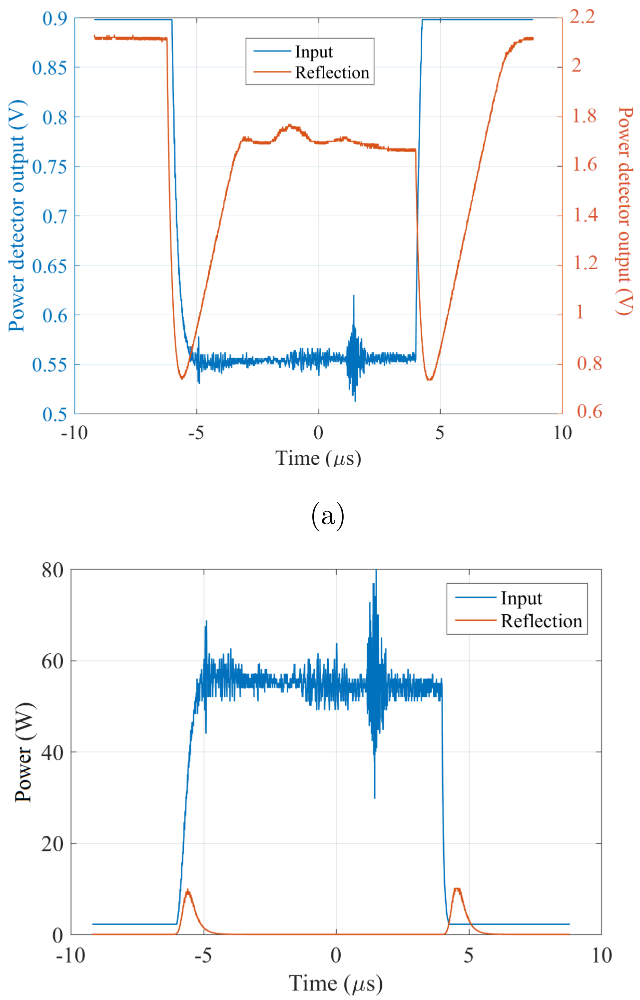

(a)

(b)

Figure 2.15: (a) The signal detected by the oscilloscope. In the experiment, we minimize the reflection from the RF cavity by adjusting the end mirror of the laser oscillator and hence its repetition rate. An active feedback loop keeps the repetition rate constant in time. Minimum reflection in power corresponds to maximizing the reflection signal in the oscilloscope. (b) Conversion the volatges read by the oscilloscope to the actual input and reflected powers.

2.7 General Particle Tracer simulation of the electron beam

The General Particle Tracer (GPT) is a numerical simulator developed by Pulsar Physics that we used to analyze the setup and find an insight into different beam line components and their functions. It helped to estimate quantities that we do not measure directly like the energy spread of the beam, the emittance and the transverse coherence length. Table 2.2 summarizes the parameters we fed into the simulator. The values of the coil currents are the same as what used

Table 2.2: GPT simulator input parameters.

Simulation Parameters	Values
Laser spot size on cathode	50 μm
Laser pulse duration	40 fs
Accelerator DC voltage	90 kV
Number of electrons per pulse	100,000
1st coil current	8.115 A
1st coil position	43.9 mm
2nd coil current	1.232 A
2nd coil position	275 mm
3rd coil current	2.869 A
3rd coil position	650 mm
RF cavity amplitude	1.6 Mv/m
RF cavity phase	0.76 rad
RF cavity position	577 mm
Target position	800 mm
Phosphor screen distance form cathode	1360 mm

in the experiment (as described in table 2.2) to make the beam transverse size small enough on the target and the detector. The phase of the RF cavity was set so that the average kinetic energy and hence the average gamma factor of the pulse be the same before and after the cavity. The amplitude was set such that the pulse was temporally focused at the target position. As we will discuss it in the next chapter, in the experiment, the phase and amplitude of the RF cavity were determined in the exact same way. The results of the simulation is the most sensitive to the position of the first coil.

Figures 2.16a and 2.16b show the standard deviations of the transverse size and the pulse duration of the electron pulse as functions of distance from the cathode. The minimum pulse duration is around 50 fs rms equivalent to 117 fs FWHM. If we increase the number of electrons per pulse from 10^5 to 5×10^5, with the rest of the parameters untouched, the duration increases to around 220 fs FWHM. As we will discuss in the next chapter, the jitter in the RF cavity phase blurs that difference in the the pulse duration due to the number of electrons. In other words, we hardly measured any pulse duration less than 350 FWHM for both amounts of charge per pulse, indicating there is a timing jitter with a value comparable to the pulse duration.

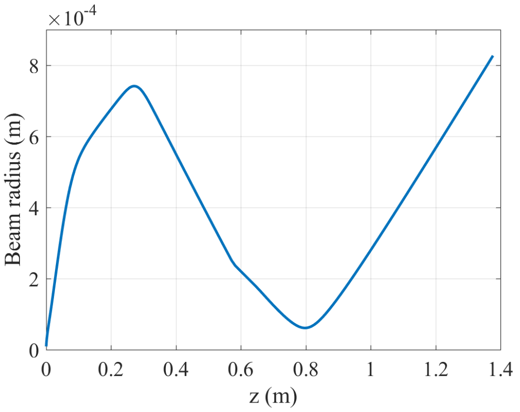

(a)

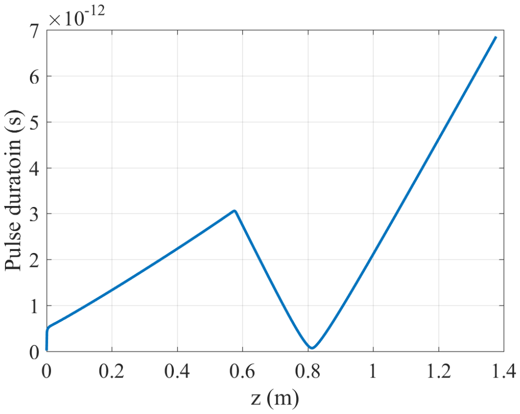

(b)

Figure 2.16: (a) The beam radius (std) and (b) the pulse duration (std) simulation by GPT.

The percentage of the kinetic energy (KE) spread of the electron pulse can be obtained from

$$\frac{\delta KE}{\overline{KE}} = \frac{m_e c^2 \delta\gamma}{m_e c^2(\bar{\gamma} - 1)} \times 100, \tag{2.22}$$

where δ and *overbar* indicate the standard deviation and average, respectively, and γ is the relativistic gamma factor. Figure 2.17 depicts the energy spread of the electron pulse. The energy spread has two jumps at the acceleration stage and the RF cavity and goes to a minimum at the target place where it is compressed in all directions with a value of 0.5%. If we increase the number of electrons to 5×10^5, and keep the other parameters the same, the KE spread becomes 0.82%.

The transverse coherence of the electron beam is a major parameter to have

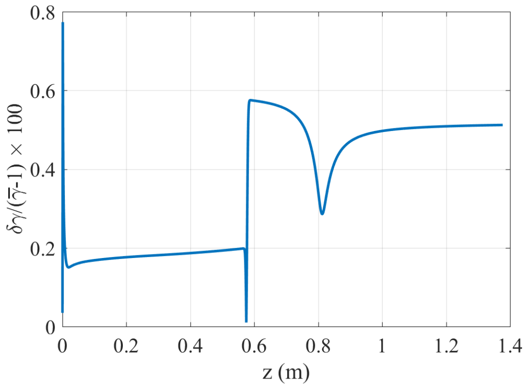

Figure 2.17: Kinetic energy spread percentage of the electron pulse.

a high quality diffraction pattern. Its value should cover the size of one molecule so there is a coherent interference by which we retrieve the molecule's structure. On the other hand, it should be smaller than the distance between two adjacent molecules in the gas so we get incoherent superposition of their individual diffraction signals. The transverse coherence length can be calculated from [88]

$$L_\perp = \frac{\hbar}{m_e c}\frac{\sigma_{target}}{\epsilon_x}, \tag{2.23}$$

where σ_{target} is the transverse size of the electron at the target, and ϵ_x is the transverse rms normalized emittance of the electron pulse defined by [88]

$$\epsilon_x = \frac{1}{m_e c}\sqrt{\langle x^2\rangle\langle p_x^2\rangle - \langle x p_x\rangle^2}, \tag{2.24}$$

where x and p_x are the position and the momentum of a single electron with respect to the center of the pulse and its average momentum and the angle brackets indicates the average over the whole pulse. According to the GPT simulation results, ϵ_x is around 11.7nm (equivalent to 0.0117 mm mrad) for a beam size of around 100-120 μm, resulting in a coherence length of 3.5 to 4 nm, which is consistent with a previous report [59].

2.8 Pump laser setup

The atoms or molecules under study are excited by femtosecond laser pulses and probed by the femtosecond electrons. However, 90 keV electrons propagate with a velocity that is 0.526 times smaller than the pump velocity c. For a gas jet with a hundreds of micrometer diameter, this discrepancy in velocities will significantly reduce the temporal resolution of the setup because not all of the molecules will be excited and probed with the same timing interval. This problem is regarded as the pump-probe velocity mismatch problem. In our setup, we use a technique called the laser front tilting to solve the velocity mismatch problem. First, we will review the problem in more details and then we describe the solution.

2.8.1 Laser-electron mismatch velocity

The effect of velocity mismatch in ultrafast pump-probe experiments was first highlighted by Zewail et al. [67]. Their analysis showed that the temporal blurring due to the velocity mismatch has a major contribution and can be the main limiting factor of the experimental resolution. Figure 2.18 shows the geometry of a pump-probe experiment. The FWHMs of the gas jet, the laser pulse and the electron pulse are w_g, w_l and w_e, respectively. The FWHM durations of electron and laser pulses are τ_e and τ_l, respectively. The electrons propagate with the velocity v_e and the angle between the electrons and the laser is θ. The temporal resolution of the setup can then be obtained from [67]

$$\tau_{total}(\mathrm{FWHM}) = \sqrt{\tau_e^2 + \tau_l^2 + \tau_{vm}^2}, \tag{2.25}$$

where τ_{vm} is the temporal broadening due to the velocity mismatch and is given by [67]

$$\tau_{vm} = \frac{1}{c}\sqrt{\frac{w_e^2 w_g^2(\frac{c}{v_e}\cos\theta - 1)^2 + w_l^2 w_g^2(\frac{c}{v_e} - \cos\theta)^2 + w_e^2 w_l^2((\frac{c}{v_e})^2 - 2\frac{c}{v_e}\cos\theta + 1)}{w_g^2 \sin^2\theta + w_l^2 + w_e^2 + w_l^2 w_e^2 / w_g^2}}. \tag{2.26}$$

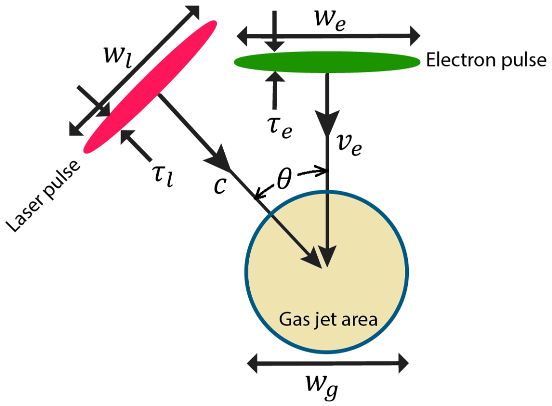

Figure 2.18: Laser, electrons and the gas jet geometry in a gas-phase pump-probe experiment.

Figure 2.19 shows the calculated temporal resolution of the setup as a function of the width of the laser and the electron beams for $\theta = 58.3^{\mathrm{o}}$, and different widths of the gas jet. For the laser and electron beams making the angle $\theta = 58.3^{\mathrm{o}}$, the longitudinal component of the laser pulse velocity will have the same velocity as the electrons. In this figure, the electron and laser pulse durations are 350 fs and 50 fs, respectively. The width of the gas jet plays an important role in the temporal resolution, since the velocity mismatch problem will be less severe as the target size shrinks. For solid samples with a thickness of several hundreds of nanometer, the velocity mismatch would not be an issue. However, in gas phase experiments, the width of the gas jet cannot be reduced because of both practical barriers and also the fact that atoms and molecules may form clusters by reducing the size. The electron and laser beam widths should be of the same size of the gas jet to excite and observe as many particles as possible. The other way to alleviate the velocity mismatch problem is to reduce the angle between the pump and probe. Suppose we confine the width of gas jet, the laser beam and the electron beam to 250 μm FWHM. Figure 2.20 shows the temporal resolution of the setup as a function of the angle between the pump and probe. As we decrease the angle, the temporal resolution increases, but the velocity mismatch broadening never vanishes. In addition, making the angle very small will not be easily feasible because of practical issues. The other solution is to keep the angle $\theta = 58.3^{\mathrm{o}}$, so

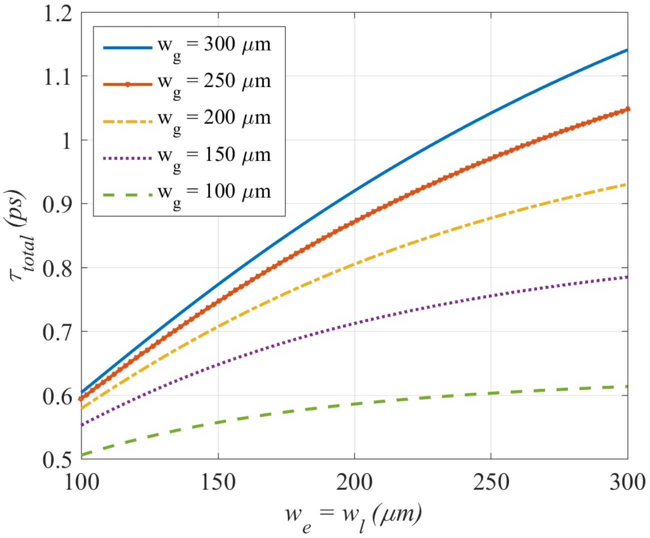

Figure 2.19: FWHM of the setup temporal resolution as a function of the laser and electron beam widths that are kept the same, for different width of the gas jet. The other parameters are $\tau_e = 350 fs$, $\tau_l = 50$ fs, $v_e = 0.526c$, and $\theta = 58.3^{\text{o}}$.

the two beams have the same longitudinal velocities but to tilt the intensity front of the laser pulse so it coincides the electron pulse.

2.8.2 Theory of tilted front laser pulses

Laser intensity front is a technique developed to solve the pump-probe velocity mismatch problem [68, 69, 89]. Figure 2.21 shows two configurations of the laser and electron pulses. The angle θ is chosen so the longitudinal component of the laser beam have the same value as the electron pulses, i.e.

$$\theta = \cos^{-1}(\frac{v_e}{c}). \tag{2.27}$$

In the tilted laser pulse configuration, the intensity front of the laser intensity is tilted to make an angle $90 - \theta$ degrees with its direction of propagation. By this technique, the timing between the laser and electron pulse remains the same throughout the gas jet area.

The intensity front tilting is done by a reflective optical grating. As is shown in Figure 2.22, the grating consists of a periodic vertical ridges with a period of d equivalent to the grating constant of $1/d$ ridges per unit of length. Because of

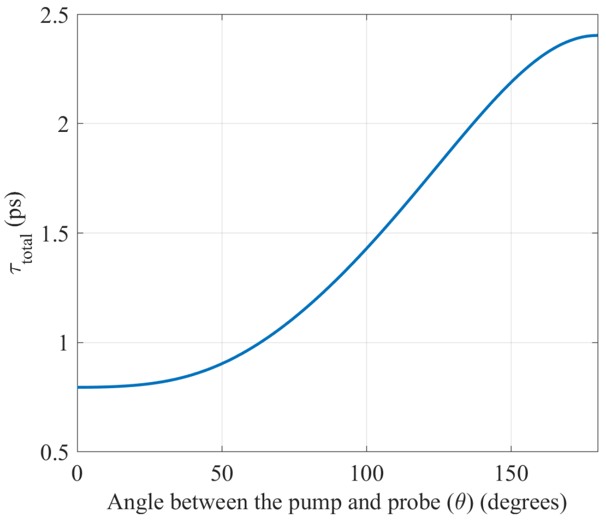

Figure 2.20: FWHM of the setup temporal resolution as a function of the angle between the laser and electron beams. The other parameters are $\tau_e = 350$ fs, $\tau_l = 50$ fs, $v_e = 0.526c$, and $w_e = w_l = w_g = 250\mu$m.

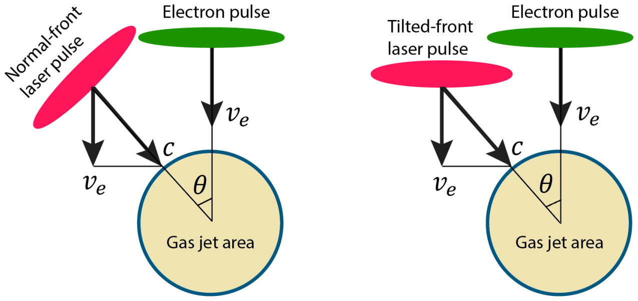

Figure 2.21: The pump-probe experiment in two configurations. The pump-probe angle is selected such that the longitudinal component of the laser velocity vector has the same value as the electron velocity. For 90 keV electrons, the angle is $\theta = 58.3^{\circ}$. In the normal-front laser beam, the constant intensity planes are normal to the direction of propagation. In the tilted-front laser beam, however, the constant intensity fronts make an angle $(90 - \theta)$ degrees with the direction of propagation. In this configuration, the timing between the laser and electron pulses is constant, therefore, there is no velocity mismatch.

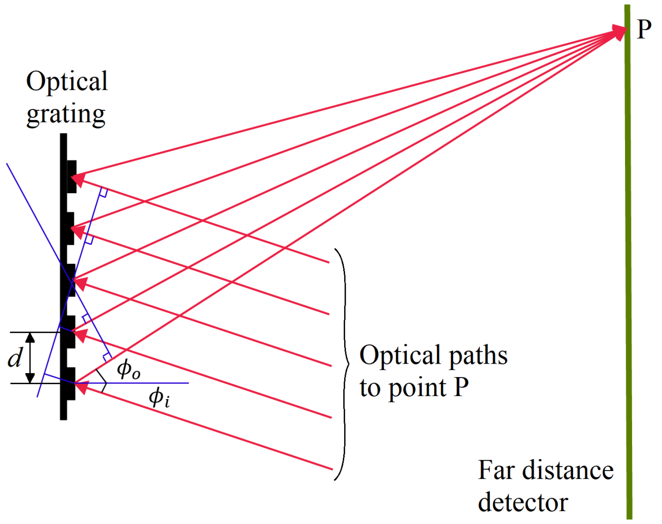

Figure 2.22: Diffraction of light by an optical grating. Each red line shows an optical paths to the point P on a far distance detector. Each path is slightly different in length from the others; hence, the optical rays going to point P on each path will have a different phase.

the ridges, the incident beam will be diffracted by the grating. Suppose a plane wave incidents with an angle ϕ_i on the grating. The outgoing beam E_o will be proportional to

$$E_o \propto \sum_{n=-N}^{+N} e^{-in2\pi\frac{d}{\lambda}\times(\sin\phi_o - \sin\phi_i)} = \frac{\sin((2N+1)\pi\frac{d}{\lambda}(\sin\phi_o - \sin\phi_i)}{\sin(\pi\frac{d}{\lambda}(\sin\phi_o - \sin\phi_i))}, \tag{2.28}$$

where λ is the wavelength of the incident beam and $2N$ is the number of ridges. The detected intensity I_o will be proportional to

$$I_o \propto |E_o|^2 \propto \frac{\sin^2((2N+1)\pi\frac{d}{\lambda}(\sin\phi_o - \sin\phi_i)}{\sin(\pi\frac{d}{\lambda}(\sin\phi_o - \sin\phi_i))}. \tag{2.29}$$

According to equation (2.29), the maximums of intensity take place whenever its denominator vanishes:

$$d(\sin\phi_o - \sin\phi_i) = m\lambda, \tag{2.30}$$

where m is an integer and called the order of diffraction. If we take a derivative

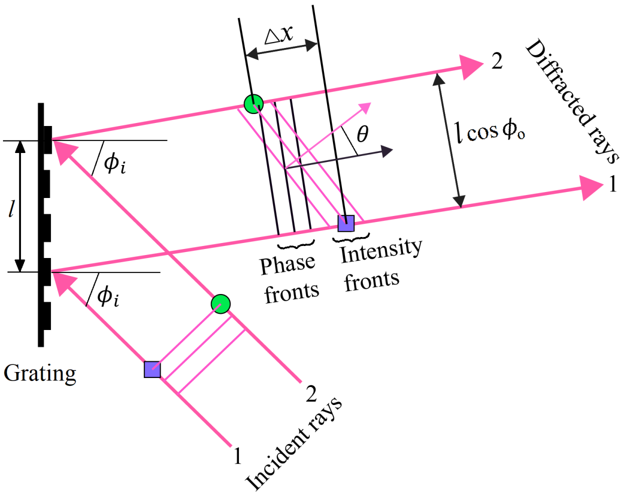

Figure 2.23: Intensity front tilting by the grating. Two parallel rays are diffracted by the grating at the zero angle. Consequently the ray 1 will be ahead of ray 2 by value Δx. From this geometry we calculate the tilt angle θ.

from equation (2.30) with respect to ϕ_o and invert the result, we get

$$\frac{d\phi_o}{d\lambda} = \frac{m}{d\cos\phi_o}, \tag{2.31}$$

which is known as the grating dispersion relation. Now, suppose the grating is designed so the first order diffracted beam comes at the zero angle with respect to the grating normal, so $\phi_o = 0$, we want to find the tilt angle θ. Figure 2.23 shows the front tilting by the grating. Consider two optical rays hitting the grating by the angle ϕ_i and are diffracted to angle $\phi_o = 0$. After the diffraction, ray 1 will be ahead of ray 2 by the amount of $\Delta x = l\sin\phi_i - l\sin\phi_o$. The tangent of the tilt angle is

$$\tan\theta = \frac{\Delta x}{l\cos\phi_o} = \frac{\sin\phi_i - \sin\phi_o}{\cos\phi_o}. \tag{2.32}$$

By use of equation (2.31), equation (2.32) becomes

$$\tan\theta = -\frac{m\lambda}{d\cos\phi_o} = -\frac{d\phi_o}{d\lambda}\lambda. \tag{2.33}$$

Suppose that the refracted beam is normal to the surface of the grating, and the laser beam has a bandwidth of $\Delta\lambda$. By rearranging equation (2.31) and taking integral of it, we get

$$\sin\phi_{o2} - \sin\phi_{o1} = \frac{m}{d}\Delta\lambda, \tag{2.34}$$

where ϕ_{o2} and ϕ_{o1} are angles that represent the edge of the output beam. For a small laser bandwidth, the two angles are small and we may write $\sin\phi_{o2} \approx \phi_{o2}$ and $\sin\phi_{o1} \approx \phi_{o1}$; hence, equation (2.34) becomes

$$\Delta\phi_o = \phi_{o2} - \phi_{o1} = \frac{m}{d}\Delta\lambda. \tag{2.35}$$

Therefore, the beam has a divergence angle that is proportional to its wavelength bandwidth. The grating translates the bandwidth of the laser into a divergence angle, and gives a spatial chirp to the refracted beam. Tilting the laser intensity front will change the pulse duration too. A Fourier analysis of a Gaussian beam with a temporal profile of $\exp(-(2\sqrt{\ln 2}\frac{t}{\tau_{l0}})^2)$, with τ_{l0} being the FWHM duration of the incident pulse, shows that the laser pulse duration increases as a function of the distance from the grating z as [90]

$$\tau_l(z) = \tau_{l0}\sqrt{1 + \frac{(2\ln 2)^2(\frac{d\phi_o}{d\lambda}|_{\lambda_0})^4\lambda_0^6}{\pi^2 c^4 \tau_{l0}^4} z^4}, \tag{2.36}$$

where λ_0 is the central wavelength of the laser. Equation (2.36) assumes that there is a negligible distortion because of the spectral lateral walk-off [90]. If we image the surface of the grating, the pulse duration of the incident pulse can be retrieved at the image plane. For this case, temporal distortions can be avoided if the grating face coincides the object plane, i.e., $\phi_o = 0$ [91]. Demagnification of the imaging setup can change the tilt angle at the image plane. If M is the demagnification of the imaging setup, and θ' is the tilt angle at the image plane, we have

$$\tan\theta' = -M\tan\theta, \tag{2.37}$$

where the minus sign comes from the fact that the image is spatially inverted with

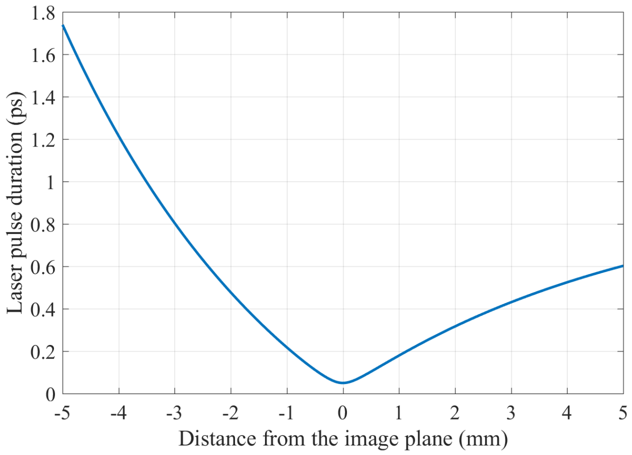

Figure 2.24: Tilted laser pulse duration as a function of deviation from the image plane.

respect to the object.

In our setup, the grating period is $d = 6.7\mu$m corresponding to the grating constant of 150 mm^{-1}, and 80% of incident power diffracts to the first order. For $\phi_o = 0$, the tilt angle from equation (2.33) becomes $\theta = -6.85^{\text{o}}$ and the incident angle from equation (2.32) becomes $\phi_i = -6.9^{\text{o}}$. For the tilt angle of $\theta' = 58.3^{\text{o}}$, necessary for the laser-electrons velocity matching, the demagnification from equation (2.37) becomes $M = 13.36$. To control the laser beam size on the image plane which is the position of the gas jet, we adjust the size of the beam on the grating by use of a telescope.

The pulse duration as a function of distance from the image plane can be obtained by including the demagnification M in equation (2.36), i.e.

$$\tau_l(z) = \tau_{l0}\sqrt{1 + \frac{(2\ln 2)^2 (M(z)\frac{d\phi_o}{d\lambda}|_{\lambda_0})^4 \lambda_0^6}{\pi^2 c^4 \tau_{l0}^4} z^4}. \tag{2.38}$$

Here, the demagnification is the size of the beam on the grating over the size of the beam around the image plane. For $f = 0.25$m the focal length of the imaging lens, M becomes equal to $\frac{1}{4z+0.077}$. Figure 2.24 shows the pulse duration as a function of distance from the image plane.

The width of the tilted laser pulse should be chosen so that it covers all area

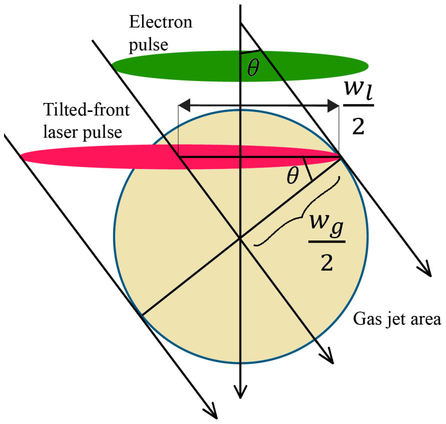

Figure 2.25: Interaction area of the laser and the gas jet.

of the gas jet. Figure 2.25 shows the interaction area of the laser and the gas jet. Because the front of the laser is tilted, its width should be larger in comparison to the width of a normal front laser to cover the gas jet area. According to Figure 2.25, the width of laser beam w_l whose front is tilted by angle θ, should be equal to $\frac{w_g}{\cos\theta}$ to cover the gas jet.

2.8.3 Tilted pulse setup and measurement

Figure 2.26 depicts the elements of the optical setup by which we generate the tilted front laser pulses and measure the tilt angle and the pulse duration at the image plane. In that figure, mirrors, pinholes and beam splitters are shown by M, P, and BS respectively, and the numbers show the order by which the laser hits the optics. The beam from the laser amplifier is directed to an optical telescope for a desired size on the grating and hence at the target. The pinhole P1 can be put on the mounts of either the convex or the concave lens to make the beam centered on them. By use of P2 the beam is kept parallel to the motion of the moving stage that is to delay the pump laser. Fine adjustments of that stage is necessary to avoid any change in the beam pointing while the stage is moving. The position of P3, P4, P5 and P6 are chosen so the beam goes at 6.9° to the grating and comes out perpendicularly. Mirrors M6 and M7 are responsible for the beam going through P3 and P4. The diffracted beam from the grating is adjusted by the position of the grating and its angle so it goes through P5 and P6. By this, we make sure that the diffraction angle is zero. The diffracted beam goes to M8 and M9 on another moving stage by which the accurate object distance is set. From this point, the beam is directed by several other mirrors and a periscope to the target chamber. There is a beam polarizer to set the polarization of the beam. If we need to measure the tilt angle and the pulse duration, we can split the beam before going to the grating by BS1 into the normal front beam and the tilted front beam. The normal front beam goes to another set of mirrors and combines with the tilted front pulse at BS2. The moving stage in the normal beam path is used to make the optical distance from BS1 to BS2 the same for both beams such that the two beams temporally overlap. The accurate timing was found by synchronizing each beam individually to the electron beam in a way we will explain in Section 4.5. We used P7 and P8 to spatially overlap the two beams. For accurately setting the beams on the pinholes, we partially close P1 (while the laser power is low) to generate diffraction rings in the beam. Then, we adjust the two last mirrors before P7 in each beam to center the diffraction rings onto the edge of the pinholes. The beam is guided to a periscope to bring it to the height of the target chamber. The beam after the periscope is directed to the target chamber. Figure 2.27 shows the beam going to the chamber. In this figure, L1 is the lens that images the grating on the target position. The beam then goes out of the chamber to a beam block. By an optical wedge, we take a sample from the outgoing beam. We image the target plane (nozzle) by another lens (L2) onto a CCD camera with a demagnification of $M' = 0.29$. By use of this camera, we observe the interference between the two overlapping beams from which we evaluate the tilt angle and the pulse duration. Note that the the laser pulse duration, measured in the direction of propagation, is the same at the second imaging plane (CCD camera) but the tilt angle is different since the total demagnification is different. The total demagnification will be $MM' = 13.36 \times 0.29 = 3.88$ and from equation (2.37), the tilt angle will be 25.1^{o} at the camera.

Figure 2.28 shows the normal and tilted front laser pulses overlapping on a

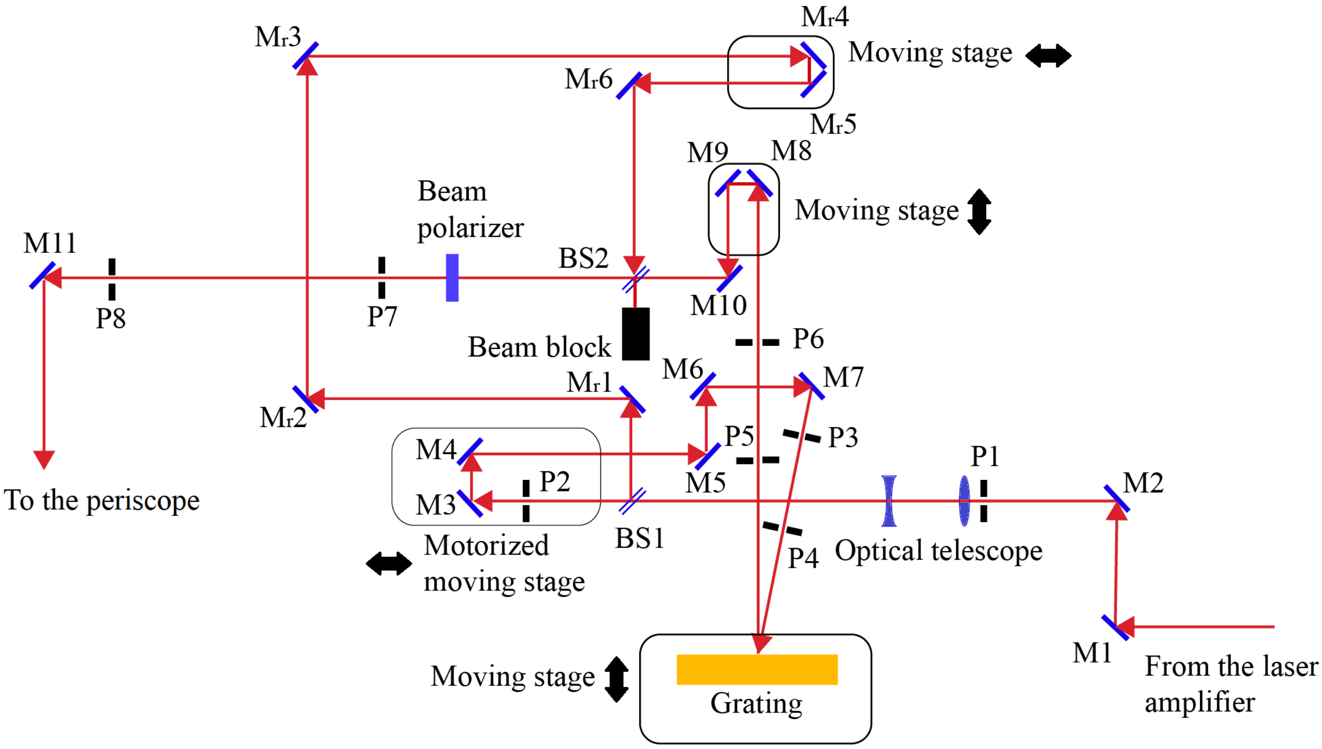

Figure 2.26: Tilted front laser pulse generation and measurement setup. Here, mirrors, pinholes and beam splitters are shown by M, P, and BS respectively, and the numbers show the order by which the laser hits the optics

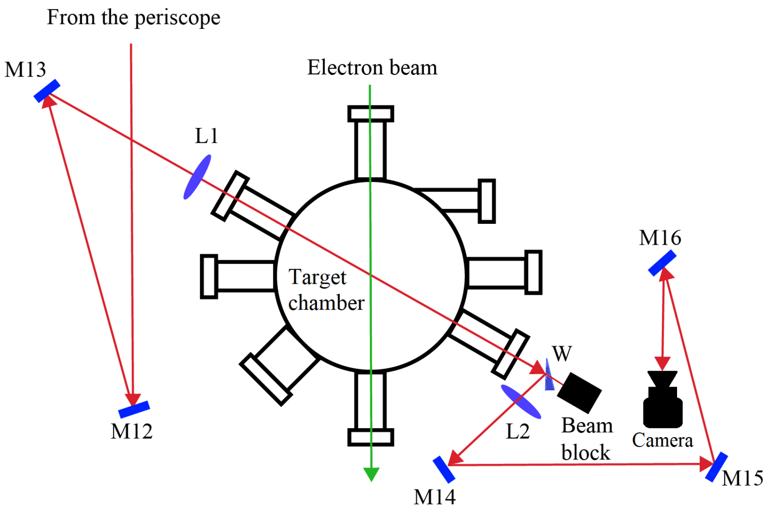

Figure 2.27: Tilted front laser pulse path to the target chamber.

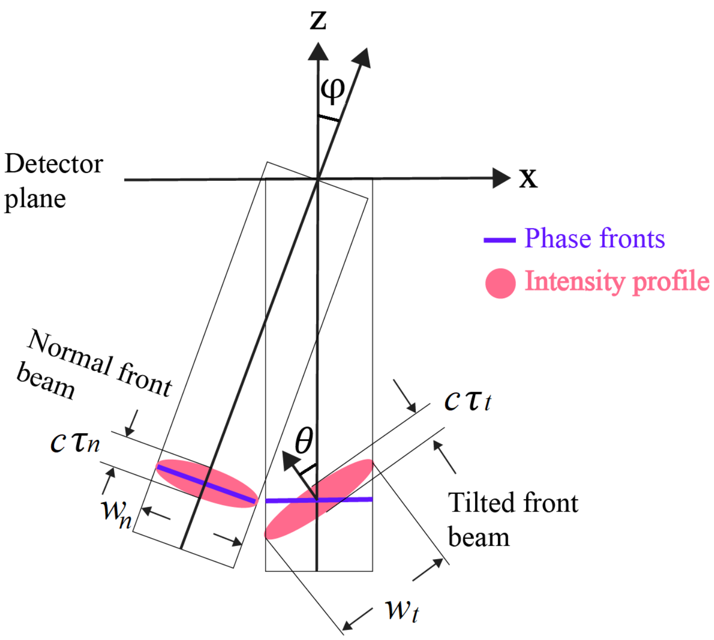

Figure 2.28: The tilted pulse and the normal front pulse overlap spatially and temporally on the detector plane and interfere. From the the interference pattern we extract the angle between the two beams φ, the tilt angle θ and the duration of the tilted front pulse.

detector at $z = 0$ plane. In this figure, θ is the tilt angle and ϕ is the angle between two beams in the x-z plane and we assume there is no angle in y-z plane. The electric field of the tilted pulse, near the image plane, can be approximated by

$$\begin{aligned} E_t \approx & E_0 \exp\left\{ -\frac{(-x\sin\theta + (z - c(t-t_0))\cos\theta)^2}{c^2\tau_t^2/(4\ln 2)} - \right. \\ & \left. \frac{(x\cos\theta + (z - c(t-t_0))\sin\theta)^2 + y^2}{w_t^2/(4\ln 2)} \right\} \times \exp\{i(kz - \omega(t-t_0))\}, \end{aligned} \tag{2.39}$$

with E_0, ω and k being the amplitude, angular frequency and wave number of the field, respectively. The electric field of the normal pulse, by ignoring the curvature of the phase front, can also be approximated by

$$\begin{aligned} E_n \approx & E_0 \exp\Bigg\{ -\frac{((z-ct\cos\varphi)\cos\varphi+(x-ct\sin\varphi)\sin\varphi)^2}{c^2\tau_n^2/(4\ln 2)} - \\ & \frac{(-(x-ct\sin\varphi)\cos\varphi+(z-ct\cos\varphi)\sin\varphi)^2+y^2}{w_n^2/(4\ln 2)}\Bigg\}\times \\ & \exp\{i(k(z\cos\phi+x\sin\phi)-\omega t)\}. \end{aligned} \tag{2.40}$$

The total intensity will be proportional to $I \propto |E_t+E_n|^2$ with an interference term I_{int}, approximately proportional to

$$\begin{aligned} I_{int} \propto & E_0^2 \exp\Bigg\{ -\frac{(z-ct)^2}{c^2\tau_n^2/(4\ln 2)} - \frac{(-x\sin\theta+(z-c(t-t_0))\cos\theta)^2}{c^2\tau_t^2/(4\ln 2)}\Bigg\}\times \\ & \cos(\omega t_0+kx\sin\varphi), \end{aligned} \tag{2.41}$$

provided that $w_t, w_n \gg c\tau_t, c\tau_n$ and $\varphi \to 0$. Equation (2.41) shows fringes only along the x-axis since we assumed there is no angle between the beams in the y direction. The period of fringes is equal to $\frac{2\pi}{k\sin\varphi}$. The interference, however, is limited to a small area where the two beams overlap. In the experiment, we try to make the angle φ smallest to minimize the number of fringes over that area for a more accurate measurement. Figures 2.29a and 2.29b show the simulation of total intensities in $y=0$ and $z=0$ planes, respectively, where the angle between the two beams is 1^o and the tilt angle is 25^o, for $t_0=0$. The other parameters are E_0=1 V/m, $\tau_t=100$ fs, $\tau_n=80$ fs, $w_t=w_n=300\mu$m. If we delay the tilted front pulse by an amount of t_0, the peak of interference envelope will move on the $z=0$ plane by the value of $\Delta x = ct_0/tan(\theta)$, from which we can measure the tilt angle.

The last parameter we can measure from the width of interference envelope is the duration of the tilted pulse. On a CCD camera that lies on $z=0$ plane, the

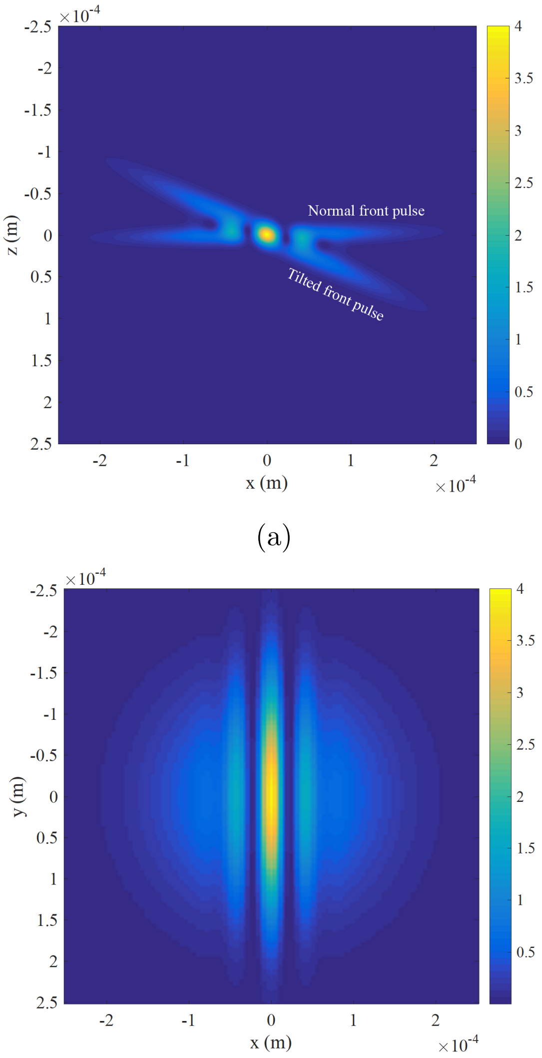

(a)

(b)

Figure 2.29: Interference of the tilted pulse and the normal pulse in (a) $y = 0$ and (b) $z = 0$ planes. The intensities are in the unit of W/m^2

detected signal will be the integral of I_{int} in equation (2.41) over all times, i.e.,

$$\begin{aligned}\int_{-\infty}^{\infty} I_{int} dt \propto & E_0^2 \cos(kx\varphi)\times \\ & \int_{-\infty}^{\infty} \exp\left\{ -\frac{(ct)^2}{c^2\tau_n^2/(4\ln 2)} - \frac{(x\tan\theta + ct)^2}{c^2\tau_t^2/(4\ln 2\cos^2\theta)} \right\},\end{aligned} \tag{2.42}$$

for $t_0 = 0$ and $\sin\varphi \approx \varphi$. Evaluation of the integral gives

$$\begin{aligned}\int_{-\infty}^{\infty} I_{int} dt \propto \sqrt{\frac{\pi}{4\cos 2}} \frac{\tau_n \tau_t E_0^2}{\sqrt{\cos^2\theta\tau_n^2 + \tau_t^2}} \cos(kx\varphi)\times \\ \exp\left\{ - \frac{\tan^2\theta}{c^2\tau_n^2/(4\ln 2) + c^2\tau_t^2/(4\ln 2\cos^2\theta)} x^2 \right\}.\end{aligned} \tag{2.43}$$

According to equation (2.43) the interference has a Gaussian envelope with a FWHM of

$$L = \sqrt{\frac{c^2\tau_n^2 + \frac{c^2\tau_n^2}{\cos^2\theta}}{\tan^2\theta}}. \tag{2.44}$$

Hence, the tilted front pulse duration will be equal to

$$\tau_t = \frac{1}{c}\sqrt{L^2\sin^2\theta - c^2\tau_n^2\cos^2\theta}. \tag{2.45}$$

Figure 2.30a shows the interference between the normal and tilted front beams as seen on the CCD camera that is shown in Figure 2.27. The interference part is obtained by either subtracting the normal and tilted front beams separately from the total intensity or by fitting a two-dimensional Gaussian function to the total intensity and subtracting the result from the total intensity. Figure 2.30b shows the projection of the interference pattern on the x-axis with a function $A\exp(-\frac{(x-x_0)^2}{L^2/(4\ln(2))}) \times \cos(k(x-x_0)\varphi + \phi)$ similar to equation (2.43). By the fit, we determined the value of L in equation (2.44) and the angle between the two beam φ to be 123 μm and 0.12°, respectively. The resultant pulse duration from equation (2.45) is 160 fs. As is shown in Figure 2.28, the pulse duration is defined in the direction of the field gradient and not the direction of propagation. As a result, the pulse duration will be 88 fs under the nozzle where the tilt angle is 60°. The pulse duration in the direction of propagation is 177 fs both under the nozzle and at the camera.

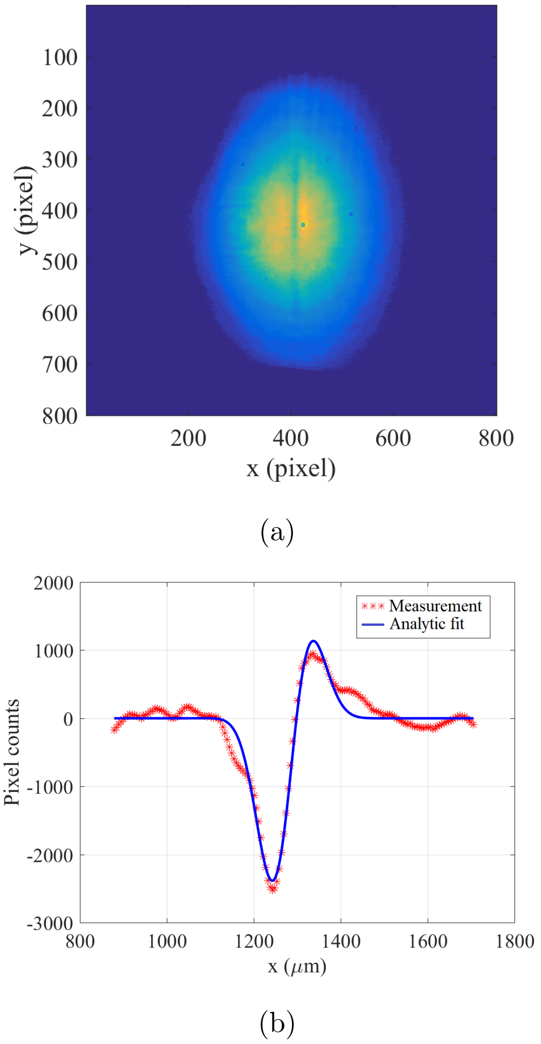

(a)

(b)

Figure 2.30: (a) Measured intensity of the interference between the normal and tilted front intensities (b) the projection of the interference term onto the x-axis and a function $A \exp(-\frac{(x-x_0)^2}{L^2/(4\ln(2)}) \times \cos(k(x-x_0)\varphi + \phi)$ fitted to it.

2.9 Summary

In this chapter, we represented a setup that can generate electron pulses of femtosecond duration with a close to Gaussian transverse profile. The electrons are photo-emitted by UV ultrafast laser pulses and accelerated to 90 kV, and then compressed transversely by magnetic lenses and longitudinally by the electric field of an RF cavity on the position of the target. The setup is equipped with a tilted front laser pump that is velocity matched to the electrons. By this setup, we are able to observe ultrafast dynamics induced by the tilted front laser pump in atoms and molecules in gas phase.

Chapter 3

Electron Pulse Duration Measurement

3.1 Introduction

In this chapter, we will describe the streak camera by which the duration of ultrafast electron pulses were measured at the position of the target. We first present a brief review on the history of streak cameras, and then focus on the laser-activated streak camera that we built. We will discuss the geometry and structure of the streak camera, and review the physics of its operation. For that, we provide a circuit analysis of the device, along with all the parameters necessary to describe its streaking field. We develop a general mathematical model that describes the streaking process and simulate the streaked patterns on the detector. Then, we will review the whole measurement setup and describe the electron pulse duration measurement process. We will also focus on how to achieve the shortest possible pulse duration. Finally, we will show how to use the streak camera to monitor the drift in the laser-electron timing.

3.2 A brief history of streak cameras

Streak cameras have a long history and were originally developed to measure optical pulses or to monitor their temporal profile. The earliest streak cameras were mechanical and took advantage of a rotating mirror that reflects the light to a recording medium such as a film [92]. For a constant speed of rotation, the detected streak length on the detector was proportional to the light pulse duration. However, poor synchronization, stability, and a limited speed of rotation all together restricted the achievable temporal resolution to the microsecond regime [93].

In the early 1970's, ultrafast streak cameras were developed that used streaking fields instead of rotating mirrors [94]. The idea of this type of streak camera was as follows: first, by a photoemission process the light (x-ray) pulse was converted to an electron pulse. Then, a time-varying electric field—e.g., the electric field of a discharging tube—was applied to that electron pulse. The electric field was perpendicular to the motion of the electrons and linearly varied with time. It thus applied different forces on different parts of the electron pulse. The applied force translated the temporal profile of the electron pulse into deflection angles, streaking it across the detector with a steak length that was proportional to the original optical pulse duration. The proportionality constant was determined mostly by the streak velocity and was one of the parameters to determine the resolution of the camera. The timing between the optical pulse and the streaking field was a critical parameter for ensuring an optimum pulse duration measurement, and was achieved by employing optoelectronics, by which the streak field timing could be controlled with relatively low jitter. From that time on, there have been many improvements in designing streak cameras both in their temporal resolution and timing jitters [95–106]. A high voltage silicon photo-switch was first integrated into a high voltage streaking tube to increase the temporal resolution and signal-to-noise ratio (SNR) due to a stronger streaking field [96]. The strength of the streaking field was further increased by employing GaAs photoswitches that offered a higher breakdown voltage [97, 107]. These types of streak camera are more suitable for pump-probe experiments, where the pump can be used to trigger the streak camera.

In the past ten years, streak cameras have been developed further to help characterize ultrafast electron pulses in the ultrafast electron diffraction (UED) experiments. Measuring the duration of femtosecond pulses requires a very rapidly changing streaking field to provide sufficient resolution. Streaking fields from a microwave cavity [108], a laser standing wave [109–111], a discharging capacitor [112–114], a split ring resonator [115], and a terahertz resonator [116] have been suggested or used. In our study, we employed a streak camera that used the electric field of a discharging capacitor since it could generate a high enough streaking field that was synchronized to our laser. We will review its geometry and structure, and provide its equivalent circuit from which we derive the differential equation that governs the device. We will review the physics behind the streaking process and develop an accurate method to extract the pulse duration from the measurements.

3.3 Streak camera theory and characterization

3.3.1 The geometry and structure of the streak camera

Figure 3.1 depicts the components of the streak camera that we used in our study. A parallel plate capacitor connected to a GaAs photo-switch constitute the streaking device. The capacitor is initially charged before a laser pulse activates the switch and the discharge process starts, i.e., the electric field across the capacitor starts a damped oscillation. Different parts of an electron pulse that go through the capacitor will see different values of that oscillating field and will be deflected to different angles. The transit time of the electron pulse through the capacitor is much shorter than the period of the oscillating field. The electrons enter the capacitor around the first zero crossing of its field, when the field has its highest rate of change and is approximately linear in time. This process maximally streaks the electron pulse on the detector by symmetrically mapping its longitudinal profile onto a transverse profile. The detector is a phosphor screen imaged onto a CCD Camera.

3.3.2 Circuit analysis of the streaking device

A schmatic of the streaking device is depicted in Figure 3.2 and photographs of it are shown in Figures 3.3a and 3.3b. As the electron first arrive at the streak camera, they are truncated by a 25 μm pinhole before going to the streaking field region. The primary role of the pinhole is to increase the resolution of the measurement by making the size of the electron beam smaller on the detector.

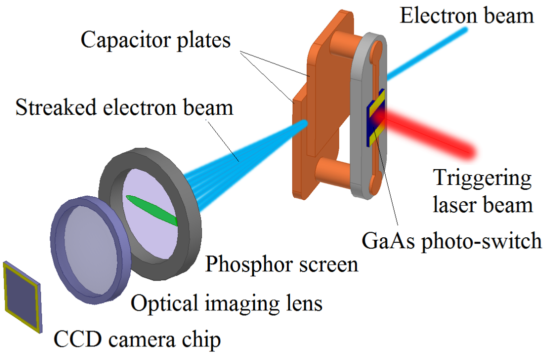

Figure 3.1: Components of the streak camera. A GaAs photo-switch is connected to a parallel plate capacitor to form the streaking device. Once the switch is activated by a laser pulse, the charged capacitor becomes short-circuited. Then the oscillating field of the discharging capacitor will streak the electron pulse going through its plates. The streaked electron pulse hits a phosphor screen that is imaged onto a CCD camera by an optical lens. (Reproduced from [114], with the permission of AIP Publishing.)

A smaller beam will observe a more uniform field across the capacitor and the chance of charge accumulation on the non-conductive parts of the streak camera is also reduced. The area of the the capacitor plates that face each other (as seen in Figure 3.2)) is 3 mm × 3 mm. The distance between the two plates is 325 μm. This accurate separation is obtained by use of several layers of Kapton tape with known thicknesses as a spacer. Kapton tapes are vacuum compatible and can tolerate high voltages. According to the size of the plates and their separation distance, the capacitance of the parallel conductors is approximately $C = 0.245$ pF. The frame that holds the structure is made of PEEK (polyether ether keton) material. In front of the streaking device, there is grounded plate to prevent charge accumulation on the frame. There is a small copper tube after the grounded plate to guide the electrons to the pinhole. Two 2 kΩ resistors are used to decouple the oscillating voltage across the capacitor from the high voltage pulse and the ground. The capacitance of the high voltage coaxial cable that connects the capacitor to the high voltage pulser is around 10 pF; hence, the time-constant of the charging process will be in order of $\tau = 2{\times}2\text{k}\Omega{\times}10$ pF $= 40$ ns, which, as we will show, is much longer than oscillation period of the capacitor, and so it will not be charged again during the oscillation.

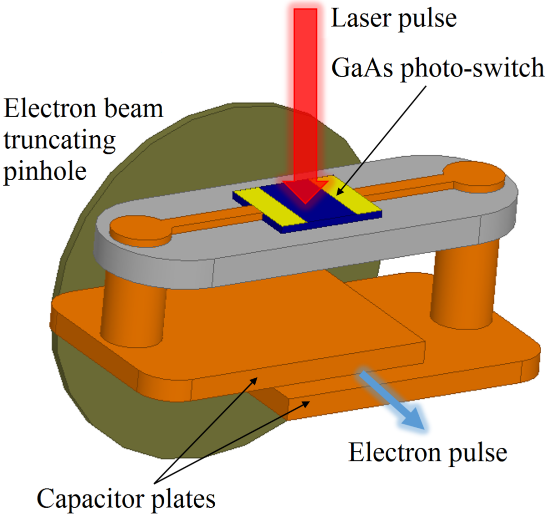

Figure 3.2: Basic illustration of the streaking device. A paralle plate capacitor is connected to a GaAs photo-switch which is activated by a laser pulse and short circuits the capacitor. Electrons are first truncated by a 25 μm pinhole and then go through the plates of the capacitor. The dimensions are not in scale in this figure for the sake of a better representation. (Reproduced from [114], with the permission of AIP Publishing.)

The homemade photo-switch is composed of a 5 mm wide, 0.6 mm thick undoped GaAs wafer with two Ohmic contacts on its sides, separated by 2.4 mm. The Ohmic contacts are composed of a 100 nm layer of gold on top of a 10 nm layer of chromium. The whole circuit has a time-independent resistance R_0 that is due to all conductors and the Ohmic contacts of the photo-switch, a time-dependent resistance $R(t)$ due to the photo-switch and a self inductance L. The equivalent circuit of the streak camera after the laser excites the photo-switch is shown in Figure 3.4. In order to figure out how the electron pulse interacts with the electric field of the capacitor, we need to know the voltage of the capacitor as a function of time. From the equivalent circuit in Figure 3.4, the differential equation that governs the voltage $V_C(t)$ across the capacitor is

$$V_C(t) + LC\frac{d^2V_C(t)}{dt^2} + C\frac{dV_C(t)}{dt}(R_0 + R(t)) = 0 \qquad (t \geq 0), \tag{3.1a}$$

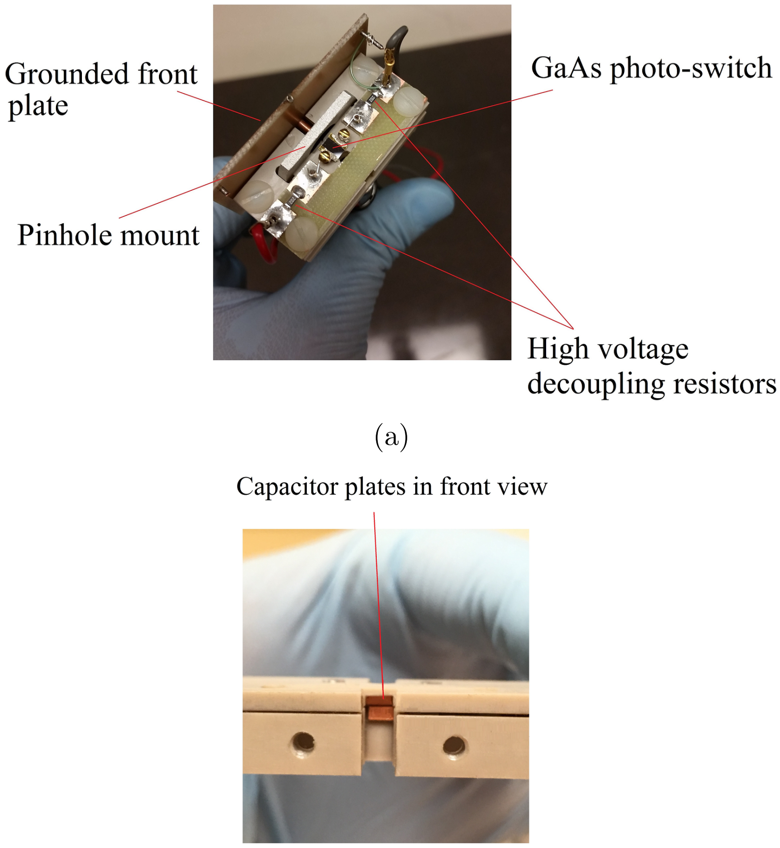

(a)

(b)

Figure 3.3: Pictures of the streaking device (a) in the top view and (b) in the front view while the pinhole and the photo-switch were not assembled. (Reproduced from [114], with the permission of AIP Publishing.)

with the initial conditions of

$$V_C(0) = V_0; \qquad \left.\frac{dV_C(t)}{dt}\right|_{t=0} = 0, \tag{3.1b}$$

where V_0 is the initial voltage across the capacitor. To solve equation (3.1a), we need to know the mathematical form of $R(t)$.

When the laser hits the GaAs wafer, the photon-created charge carrier density $n(t)$ can be estimated as [117]

$$n(t) = (\frac{1-r}{V_p})\frac{1}{E_\lambda}e^{-\frac{t}{\tau}}\int_0^t e^{\frac{t'}{\tau}}P(t')dt', \tag{3.2}$$

where $r = 0.325$ is the normal reflectance of the GaAs wafer for 800 nm tiggering

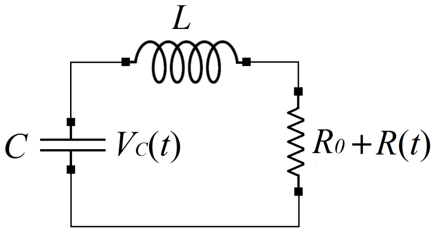

Figure 3.4: The equivalent circuit of the streaking device after the laser activates the photo-switch.

laser pulse [118], $E_\lambda = 2.48 \times 10^{-19}$J is the photon energy, $P(t)$ is the laser instantaneous power, $V_p = wl\delta_d$ is the photo-conductive volume of the GaAs wafer with $w = 5$ mm, $l = 2.4$mm, and $\delta_d = 1$ μm being the width of the photo-switch, its length and its 800 nm laser penetration depth [119], respectively. The time constant τ is a parameter that depends on the electron-hole recombination life time T_r, the Ohmic contacts injection efficiency η_i, and the drift velocity v_d [117] and is determined by

$$\frac{1}{\tau} = \frac{1}{T_r} + (1 - \eta_i)\frac{v_d}{l}. \tag{3.3}$$

Since the Ohmic contacts are not ideal, τ is always smaller than the electron-hole recombination life time. Equation (3.2) assumes the switch is illuminated uniformly, the contact loss is equal for electrons and holes, and there is no carrier trapping.

The laser pulse that excites the switch is about 40 fs long, which is much shorter than τ. Consequently, we approximate $P(t)$ in equation (3.2) by

$$P(t) = E_0\delta(t), \tag{3.4}$$

where $E_0 = 80$ μJ is the energy of the triggering laser pulse, and $\delta(t)$ is the Dirac delta function. As we will explain later, the laser power is chosen to minimize the jitter of the switch. By inserting equation (3.4) into equation (3.2), we find

$$n(t) = (\frac{1-r}{V_p})\frac{E_0}{E_\lambda}e^{-\frac{t}{\tau}} = n_0e^{-\frac{t}{\tau}}. \tag{3.5}$$

The carrier density will determine the time-dependent photo-induced conductance of the wafer as

$$\sigma(t) = (\mu_e + \mu_p)en(t), \tag{3.6}$$

where $\mu_e = 0.85$ m^{2}V^{-2}s^{-1} and $\mu_p = 0.04$ m^{2}V^{-2}s^{-1} are the mobilities of electrons and holes, respectively and e is the electron charge. By having the switch conductance, we find its resistance as:

$$R(t) = \frac{l}{w\delta_d\sigma(t)} = \frac{l^2 E_\lambda}{(\mu_e + \mu_p)e(1-r)E_0}e^{t/\tau} = R_1 e^{t/\tau}. \tag{3.7}$$

From this equation, we have $R_1 = 0.372\ \Omega$. In the above calculations, we ignored the dark current of the switch since its value is negligible and of no importance in comparison to the laser-induced current.

We designed another experiment to obtain the time constant τ to fully determine the time-dependent resistance of the GaAs photo-switch. We found τ by exciting the photo-switch by a continuous wave (CW) laser at the same central wavelength of the pulsed laser. For a CW laser turned on at $t = 0$, the power will be

$$P(t) = P_0\Gamma(t), \tag{3.8}$$

where P_0 is the power of the laser and $\Gamma(t)$ is the Heaviside step function

$$\Gamma(t) = \begin{cases} 1, & t \geq 0 \\ 0, & t < 0. \end{cases} \tag{3.9}$$

We insert equation (3.8) into equation (3.2) to get

$$n(t) = (\frac{1-r}{V_p})\frac{P_0\tau}{E_\lambda}(1 - e^{-\frac{t}{\tau}}); \quad (t \geq 0). \tag{3.10}$$

Hence, the steady-state photo-induced carrier density will be

$$n_{ss} = (\frac{1-r}{V_p})\frac{P_0\tau}{E_\lambda}, \tag{3.11}$$

and it results in the steady-state photo-switch resistance

$$R_{ss} = \frac{l}{w\delta_d\sigma(t)} = \frac{l^2E_\lambda}{(\mu_e+\mu_p)e(1-r)E_0} = \frac{\zeta_s s}{P_0\tau}, \tag{3.12}$$

where $\zeta_s s = 1.486 \times 10^{-5}$ ΩJ is a constant. For a low enough laser power P_0 and a nanosecond order τ, R_{ss} will be much larger than the contact resistance of the switch. We apply a constant voltage across the photo-switch, and measure its current as a function of the CW laser power to determine τ. We used the circuit in Figure 3.5a where the CW laser-excited switch is in series with a resistor and a DC power supply. We measured the voltage across the 47 kΩ resistor for different laser powers. From the measurement, we could determine how the resistance of the switch varies as a function of the laser power. Figure 3.5b shows the resistance of the switch and a curve from equation (3.12) fitted to it, where the fit parameter was τ and we got $\tau = 0.36$ns.

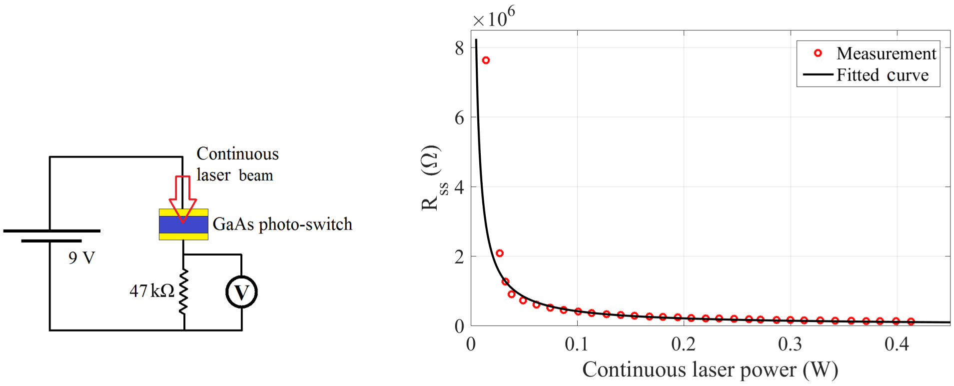

(a) (b)

Figure 3.5: (a) The circuit used to measure the resistance of the GaAS photo-switch as a function of time. (b) The resistance of the switch as a function of the laser power and a curve in equation (3.12) fitted to it. (Reproduced from [114], with the permission of AIP Publishing.)

By knowing the time-dependent resistance of the GaAs photo-switch, we can

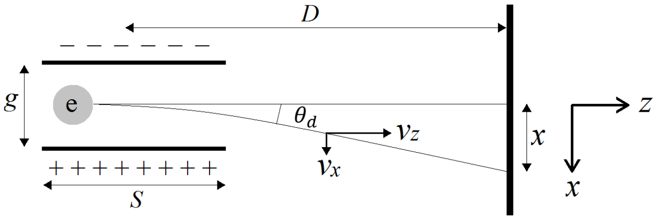

Figure 3.6: The interaction of an electron with the electric field of the parallel plate capacitor. (Reproduced from [114], with the permission of AIP Publishing.)

rewrite the differential equation in 3.1a as

$$V_C(t) + LC\frac{d^2V_C(t)}{dt^2} + C\frac{dV_C(t)}{dt}(R_0 + R_1 e^{\frac{t}{\tau}}) = 0; \qquad (t \geq 0). \tag{3.13}$$

This equation can be solved both analytically and numerically; however, there is no analytical closed form solution for it. The only parameters to be determined in this equation are the circuit self-inductance and the resistance of the Ohmic contacts of the photo-switch, which could only be obtained through an electron deflection experiment. Before proceeding, we will review that experiment.

3.3.3 Electron deflection by the streak camera

Figure 3.6 depicts the interaction of an electron with the transverse electric field across a parallel plate capacitor. We assume that the initial transverse velocity of the electron is zero and the capacitor electric field is in the x direction. As the electron traverses the capacitor plates it gains a transverse momentum which is equal to

$$p_x = \int_t^{t+t_s} \frac{eV_C(t)}{g} dt \approx \frac{eV_C(t)}{g} t_s, \tag{3.14}$$

where s and g are the length of the capacitor and the separation between its plates, respectively, and t is the time at which the electron enters the cavity and t_s is the amount of time it spends traversing the capacitor. The approximation is due to the fact that t_s is much smaller than the period of the capacitor electric field oscillation, since the electrons are accelerated by a 10^5 kV source, they have a velocity of $v_z = 0.526c$ for c being the speed of light in vacuum and we have $t_s = s/v_z$. The tangent of the deflection angle θ_d will be

$$tan(\theta_d) = \frac{v_x}{v_z} = \frac{p_x}{p_z} = \frac{eV_C(t)}{gm_e\gamma v_z}, \tag{3.15}$$

where m_e is the mass of the electron, and the γ is the relativistic gamma factor

$$\gamma = \frac{1}{\sqrt{1-\frac{v_z^2}{c^2}}}. \tag{3.16}$$

For small angles of deflection θ_d corresponding to $p_x << p_z$, the displacement of the electrons $x(t)$ on the detector, a distance D from the streaking device, will be

$$x(t) = \frac{eDs}{gm_e\gamma v_z^2}V_C(t). \tag{3.17}$$

Hence, the displacement is linearly proportional to the capacitor voltage. The result will be that the displacement $x(t)$ will satisfy equation (3.13) and we have

$$x(t) + LC\frac{d^2x(t)}{dt^2} + C\frac{dx(t)}{dt}(R_0 + R_1e^{\frac{t}{\tau}}) = 0 \qquad (t \geq 0). \tag{3.18a}$$

with the initial conditions of

$$x(0) = \frac{eDs}{gm_e\gamma v_z^2}V_0; \qquad \frac{dx(t)}{dt}\;|_{t=0} = 0. \tag{3.18b}$$

Figure 3.7 shows the displacement of the electron on the detector and a solution to the differential equation (3.18a) fitted to it. We solved the differential equation numerically by the method of finite difference and the fit parameters were the circuit self-inductance, the photo-switch Ohmic contacts resistance and the initial deflection point and we obtained $R_0 = 48\ \Omega$ and $L = 8.35$nH. Figure 3.8 shows the time-invariant resistance of the circuit as well as the time-dependent resistance of the photo-switch. Time zero is the moment that the laser pulse excites the photo-switch. As a result, the time-independent resistance of the switch can be ignored

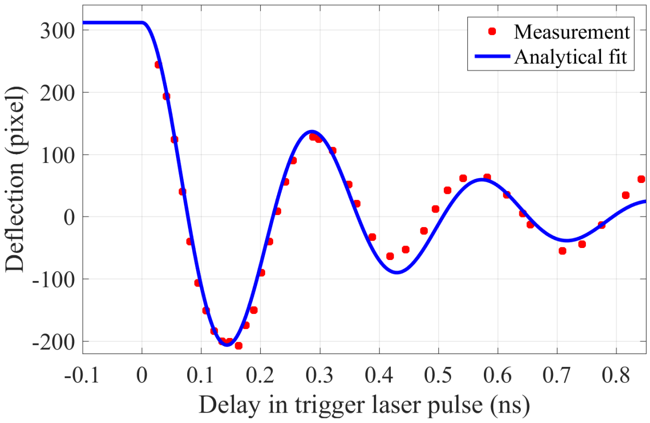

Figure 3.7: Displacement of the electrons on the detector as a function of the trigger laser pulse arrival time and the fitted function. In this Figure, $t = 0$ is the moment when the laser pulse activates the switch, which was determined from the fit. In this experiment, the initial voltage is 350 V so that the maximum displacement during the oscillation could be captured on the detector. (Reproduced from [114], with the permission of AIP Publishing.)

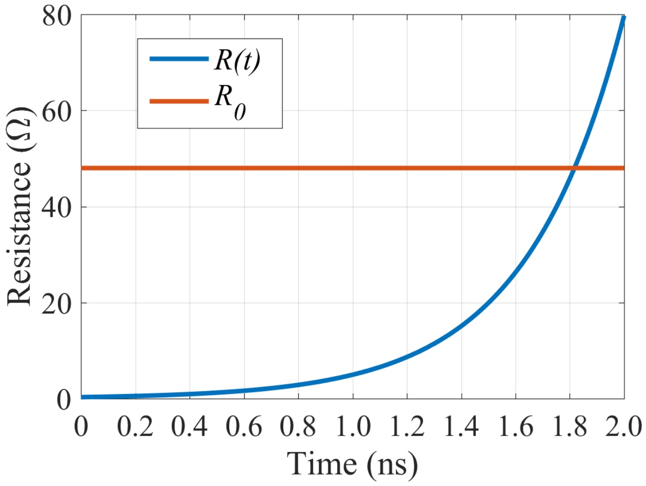

Figure 3.8: A comparison between the circuit time-independent resistance that is dominated by the Ohmic contacts of the GaAs photoswitch and the circuit time-dependent resistance that is due to the laser pulse exciting the switch. (Reproduced from [114], with the permission of AIP Publishing.)

Table 3.1: Summary of the streaking device dimensions and parameters.

Parameter	Description	Value
l	Photo-switch Ohmic contacts separation	2.4 mm
W	Width of the photos-witch	5 mm
P_0	Laser power	400 mW
E_0	Laser pulse energy	80 μJ
R_1	Resistance of the photo-switch at $t = 0$	0.372 Ω
τ	Lifetime of the photo-switch	0.36 ns
R_0	Ohmic contacts resistance of the photo-switch	48 Ω
s	Sides of the capacitor plates	3 mm
g	Separation between the capacitor plates	325 μm
C	Capacitance of the streaking capacitor	0.245 pF
L	Streaking device self-inductance	8.35 nH
D	Distance between the streaking device and the detector	57 cm
ξ	Radius of the electron beam truncating pinhole	12.5 μm

in the first few oscillations of the capacitor electric field in Figure 3.7. For those times, a damped harmonic oscillation can model the device, since the laser pulse energy is high enough to make the switch resistance small in comparison to the other resistance. In this case ($R(t) << R_0$), the displacement of the electrons when the photo-switch is excited by the laser at $t = t_0$ will be

$$x(t) = \begin{cases} \frac{eDs}{gm_e\gamma v_z^2}V_0, & t \le t_0 \\ \frac{eDs}{gm_e\gamma v_z^2}V_0 e^{-\frac{R}{2L}(t-t_0)}\cos[\sqrt{\frac{1}{LC}-\frac{R^2}{4L^2}}(t-t_0)], & t > t_0 \end{cases}, \tag{3.19}$$

where the damping rate factor $2L/R$ and the oscillation frequency $\frac{1}{2\pi}\sqrt{\frac{1}{LC}-\frac{R^2}{4L^2}}$ are equal to 0.348 ns and 3.494 GHz, respectively. The quality factor of the device is $\frac{1}{R_0}\frac{L}{C} = 3.85$. We have summarized all the parameters of the streaking device in Table 3.1.

3.3.4 Electron pulse streaking process

In this section, we will provide the mathematical description that we developed to model the streaking process, from which we can extract the electron pulse duration. Suppose two electrons enter the capacitor of the streaking device at

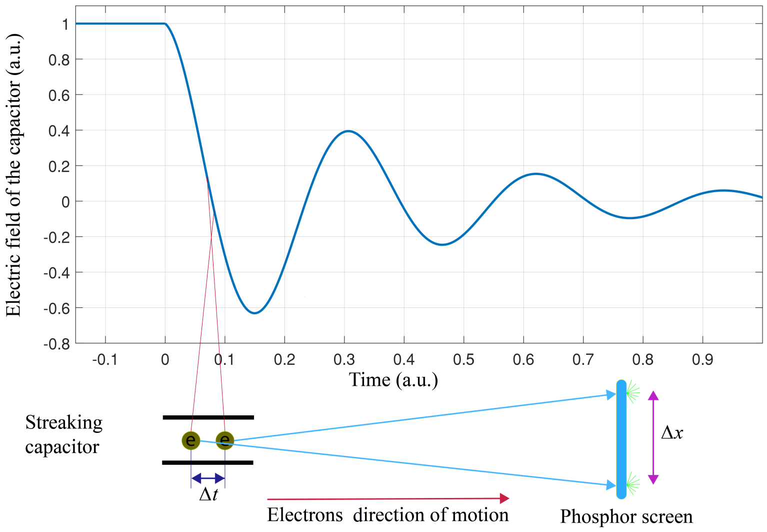

Figure 3.9: Two electrons entering the streaking device with the time interval of Δt. The capacitor applies different electric field to the electrons and deflect them differently.

times t and $t + \Delta t$ as shown in Figure3.9. According to equation (3.17), the distance between the two electrons on the detector will be

$$\begin{aligned}\Delta x = x(t+\Delta x) - x(t) &= \frac{eDs}{gm_e\gamma v_z^2}\frac{V_c(t+\Delta x) - V_c(t)}{\Delta}\Delta t \\ &\approx \frac{eDs}{gm_e\gamma v_z^2}\frac{dV_C(t)}{dt}\Delta t.\end{aligned} \tag{3.20}$$

The separation Δx will be maximum when $dV_C(t)/dt$ is maximum for which we write

$$\Delta x = \kappa\Delta t, \tag{3.21}$$

where

$$\kappa = \frac{eDs}{gm_e\gamma v_z^2}\frac{dV_C(t)}{dt}|_{max}, \tag{3.22}$$

is the streak velocity. In literature, the streak velocity is usually expressed in the unit of deflection angle per time, and is regarded as the most important parameter to quantify the performance of a streaking device. However, κ can also be expressed as in terms of pixels per time. In this case, it will determine the performance of the streak camera which is a combination of the streaking device performance, its distance from the phosphor screen and the optical setup that images the phosphor screen on the detector. We introduce a new quantity that gives the sensitivity of the streak camera and can be measured directly

$$\varsigma = \frac{1}{\kappa}. \tag{3.23}$$

The value of ς is determined experimentally by measuring the electron beam displacement on the screen as we delay the triggering laser that activates the photoswitch around the time when $dV_C(t)/dt$ maximizes, i.e., around the first zero-crossing of the capacitor electric field. Consider an electron pulse with a negligible momentum spread whose center traverses the capacitor at the first zero-crossing of its electric field. If the time zero is set at that moment, those electrons of the pulse that enter the capacitor at time t will be transversely deflected to the distance $x = \kappa t$ on the detector. Then we can rewrite equation (3.21) as

$$\Delta x = \kappa \Delta t = \frac{\kappa}{v_z} z = \kappa' z, \tag{3.24}$$

where we define the dimensionless parameter κ' the streak coefficient. Equation (3.24) means that an electron at point z, measured from the center of the electron beam, will be deflected to the point x on the detector. This process is illustrated in Figure 3.10, where a uniformly charged spheroid with the transverse semi-axis b and longitudinal semi-axis a, is first truncated by a pinhole of diameter 2ξ and then sent to a streaking device with a streak coefficient of κ'.

For an electron pulse with a constant duration, the length of the streak on the detector increases as the streaking coefficient increases. This parameter is determined by four factors that are:

1. The amplitude of the streaking field, i.e., the initial voltage across the capacitor, and the separation between the capacitor plates.

2. The maximum rate of the change in the streaking field that depends on its oscillation frequency as well as the quality factor of the device.

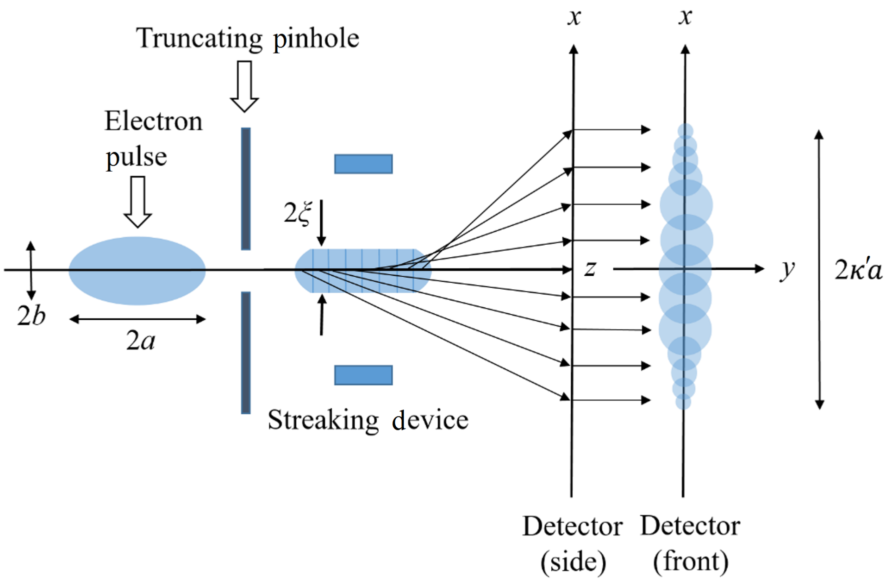

Figure 3.10: An electron pulse is composed of infinite number of differential disks. The capacitor electric field deflects each of those disks to a different angle. By this process the electrons will be streaked on the detector. (Reproduced from [114], with the permission of AIP Publishing.)

3. The distance between the streaking device and the phosphor screen.

4. The magnification of the optical lens that images the phosphor screen on the CCD camera.

For the first parameter, we are limited by the breakdown voltage of either the GaAs photo-switch or the capacitor plates. As we will describe later in this chapter, we charge the capacitor by 50 nanosecond high voltage pulses instead of a constant high voltage to reduce the chance of breakdowns. Experimentally, we saw no breakdowns for pulsed voltages of around 800 V and under in our switches. For voltages around 1500 V and above, breakdowns in the photo-switch happened. The shape of the Ohmic contacts plays a role on the voltage gradient (electric field) across the photo-switch and hence can increase or decrease the breakdown limits. To make the photo-switch, we simply covered the center part of the GaAs wafer by a piece of Kapton tape and then deposited the Ohimc contacts on its sides by the evaporation technique. As a result, very smooth edge contacts grew on the sides of the wafer.

For the second parameter, we tried to make the circuit dimensions as small

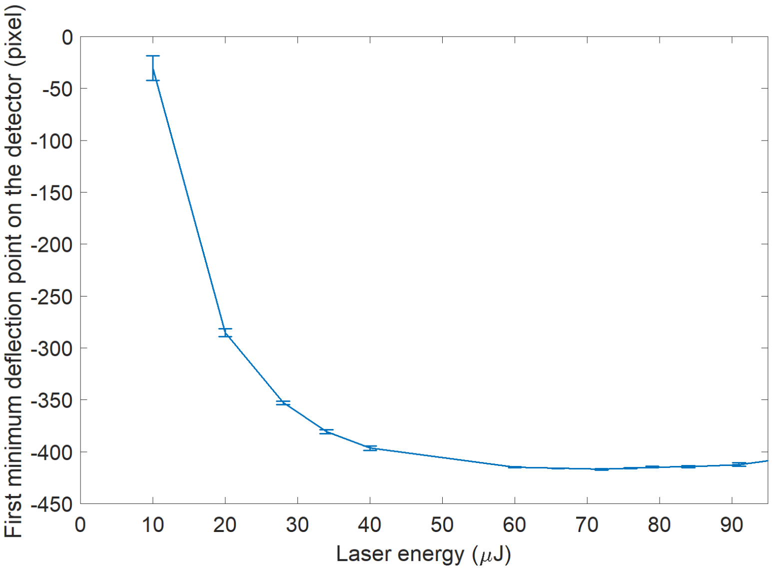

Figure 3.11: The position of electron pulses deflected by the capacitor electric field at its first minimum as a function of the triggering laser energy.

as possible, to reduce its self-inductance, which according to equation (3.19), will increase the oscillation frequency. Reducing the separation between the capacitor plates linearly increases the amplitude of the streaking field, but will decrease the oscillation frequency due to equation (3.19), yet we are limited in this by the breakdown voltage limit. The other restricting parameter is that we want to prevent the deflected electron pulses from hitting the walls of the capacitor. An increase in the quality factor will increase the depth of the minimums and consequently improve the performance of the device by increasing the rate of the change in the streaking field. As long as the triggering laser fluence is strong enough to make the Photo-switch resistance much smaller than the Ohmic contacts resistance, the quality factor is limited only by the Ohmic contacts resistance. Figure 3.11 shows the minimum deflection point on the detector as a function of the trigger laser energy. The Figure indicates that above 60 μJ energy of the pulse, corresponding to the fluence of 640 μJ/cm^2, the depth of the first minimum in the streak field is independent of the trigger energy. The uncertainty in the position of the beam also increases by decreasing the the laser energy which implies a bigger jitter in the device timing. We will discuss the device timing jitter later in this chapter.

The streaked electron pulses have a larger divergence than the unstreaked electron pulses and hence an increase in the distance between the streaking device and the phosphor screen will increase the streak length and hence the temporal resolution. An increase in the magnification in the optical setup that images the phosphor screen onto the CCD chip will increase the length of both streaked and unstreaked electron pulses in pixels too. This provides a more accurate measurement.

3.3.5 Mathematical modeling of the streaking process

Now we will try to provide a mathematical description of the streaking process. The method is general and can be apply to any type of streaking device with a streak coefficient κ'. We refer to Figure 3.10 where a uniformly charge spheroid is first truncated and then streaked. The truncated pulse is composed of an infinite number of differential disks, where each of which is deflected to a different angle. The deflection angle depends on the distance of the differential disk from the center of the pulse and the streak coefficient κ'. For now, let us ignore the divergence of the electron beam from the streaking device to the detector. After the electron pulse hits the phosphor screen, the intensity of the light emitted by the screen will be proportional to

$$\begin{aligned} &I\left(x,y;\kappa'\right) \\ &= \frac{\eta Q}{\frac{4}{3}\pi ab^2} \int\limits_{-a}^{a} dz \Gamma\left(r\left(z\right)-\sqrt{\left(x-\kappa' z\right)^2+y^2}\right)\Gamma\left(\xi-\sqrt{\left(x-\kappa' z\right)^2+y^2}\right), \end{aligned} \tag{3.25}$$

where Q is the charge of the electron pulse, η is the quantum efficiency of the screen, i.e., the number of photons created by one electron, (x,y) is the plane of the screen, $\Gamma(\bullet)$ is the Heaviside function given by equation (3.9), and $r(z)$ is the transverse radius of the uniformly charged spheroid

$$r(z) = b\sqrt{1-\frac{z^2}{a^2}}. \tag{3.26}$$

The method we are developing here, is general in a sense that equation (3.26) can be replaced by any other charge distribution, e.g., the Gaussian distribution

$$r(z) = A\exp(-\frac{z^2}{2B^2}), \tag{3.27}$$

for the amplitude A and standard deviation B. However, the electron pulses that are generated in our system are uniformly charged spheroids and hence we use equation (3.26). We evaluate the integral in equation (3.25) for two cases of $\kappa' = 0$ that corresponds to the unstreaked pulse and $\kappa' \neq 0$, that corresponds to the streaked pulses. For $\kappa' = 0$, we have

$$I_{unstreaked}\left(x, y\right) = \frac{3\eta Q}{2\pi b^2}\sqrt{1 - \frac{x^2+y^2}{b^2}}\,\Gamma\left(\xi - \sqrt{x^2+y^2}\right), \tag{3.28}$$

and for $\kappa' \neq 0$ we have

$$\begin{aligned} I_{streaked}(x, y; k') = \frac{\eta Q}{\frac{4}{3}\pi a b^2} \times \Bigg\{ & \big[(z-B^-)\Gamma(z-B^-) - (z-B^+)\Gamma(z-B^+)]\big]_{-a}^{-a\sqrt{1-\frac{\xi^2}{b^2}}} \\ & + \big[(z-A^-)\Gamma(z-A^-) - (z-A^+)\Gamma(z-A^+)]\big]_{-a\sqrt{1-\frac{\xi^2}{b^2}}}^{a\sqrt{1-\frac{\xi^2}{b^2}}} \\ & + \big[(z-B^-)\Gamma(z-B^-) - (z-B^+)\Gamma(z-B^+)]\big]_{a\sqrt{1-\frac{\xi^2}{b^2}}}^{a} \Bigg\}, \end{aligned} \tag{3.29a}$$

where

$$\begin{aligned} A^{\pm} &= \frac{x}{\kappa'} \pm \frac{\sqrt{\xi^2 - y^2}}{\kappa'}; \\ B^{\pm} &= \frac{\kappa' x}{\kappa'^2 + \frac{b^2}{a^2}} \pm \sqrt{\frac{b^2 - (x^2+y^2)}{\kappa'^2 + \frac{b^2}{a^2}} + \left(\frac{\kappa' x}{\kappa'^2 + \frac{b^2}{a^2}}\right)^2}. \end{aligned} \tag{3.29b}$$

In equation (3.29a), let $f(z)$ be any of the terms on the right hand side; then $[f(z)]_b^a = f(a) - f(b)$.

In practice, the divergence of the electron beam as well as the finite resolution of the phosphor screen are not negligible. To take these parameters into account, we Gaussian blur the intensities in equations (3.28) and (3.29a) by convoluting them with a Gaussian function, i.e.

$$I^{blurred}_{unstreaked}\left(x,y;\kappa'\right)=N\iint I_{unstreaked}\left(x',y';\kappa'\right)e^{-\frac{\left(x-x'\right)^2+\left(y-y'\right)^2}{2\sigma^2}}dx'dy', \tag{3.30a}$$

$$I^{blurred}_{streaked}\left(x,y;\kappa'\right)=N\iint I_{streaked}\left(x',y';\kappa'\right)e^{-\frac{\left(x-x'\right)^2+\left(y-y'\right)^2}{2\sigma^2}}dx'dy', \tag{3.30b}$$

where σ determines the width of the Gaussian blur and N is a normalization constant such that

$$\iint I^{blurred}\left(x,y;\kappa'\right)dxdy=\iint I\left(x,y;\kappa'\right)dxdy. \tag{3.31}$$

where I is either of the intensities in equations (3.30a) or (3.30b). Equation (3.31) comes from the fact that the total number of electrons and hence the photons generated by the screen does not change by the blurring process. Figures 3.12a and 3.12b depict the simulation of an unstreaked and a streaked electron pulse by the method developed in this section. The simulation was performed based on the parameters of an electron pulse we generated in our research as well as the sensitivity of our streak camera. We will explain in Section 3.4.5 how this mathematical model can be employed to extract the electron pulse duration.

3.4 Experimental setup

In this section, we will discuss the experimental setup by which we measured the electron pulse duration diagram of which can be seen in Figure 3.13. Electron pulses are compressed by the longitudinal electric field of the RF cavity and subsequently sent to the streaking device. The laser pulse that activates the photo-switch can be delayed by a manual stage by which we can set the capacitor discharge timing. The streaking device is held by a three-dimensional manipulator that can move the device to the position of the target. A high voltage pulser is connected to the device to initially charge the capacitor. The streaked and unstreaked pulses are captured by the phosphor screen and are imaged onto a CCD

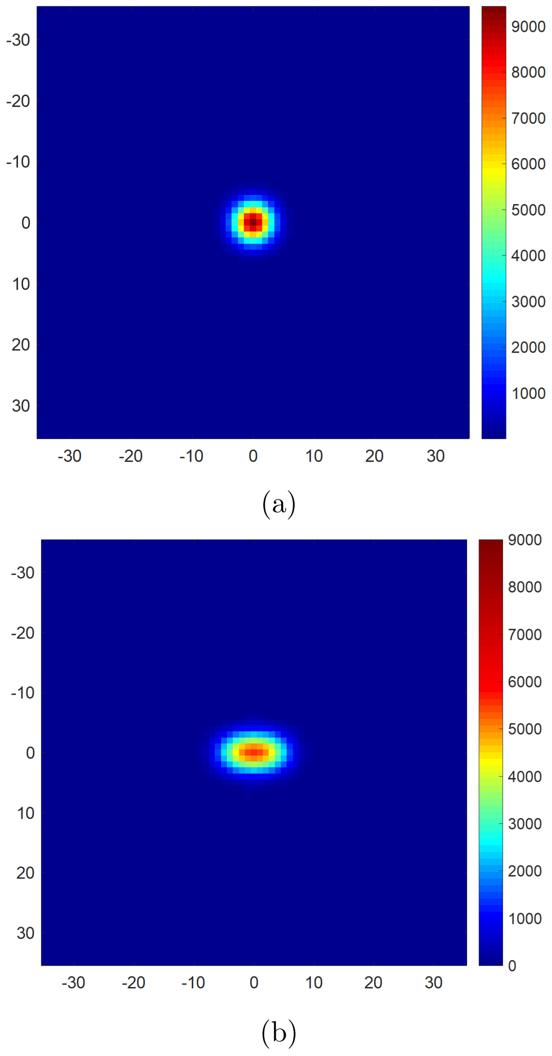

Figure 3.12: (a) Simulation of a detected unstreaked electron pulse of original diameter of 2 *mm* FWHM and 471 fs FWHM duration. The pulse is truncated by a 25 μm diameter pinhole. The width of the Gaussian blur in equation (3.30) is $\sigma = 2.226$ pixels and is chosen so that the simulated unstreaked beam matches the measured unstreaked beam as best as possible.(b) Simulation of the electron pulse in part (a) but streaked with a sensitivity of $\kappa = 69.4$ fs per pixel.

camera.

3.4.1 Triggering laser setup

We use a polarizing beam splitter in the path of the 800 nm pump laser, to pick off 400 μJ pulses to trigger the GaAs photo-switch. We use a lens to make the beam size $3mm \times 4mm$ FWHM on the photo-switch. There is one beam sampler that sends 5% of the beam to a fast photo-diode to look for any laser prepulse, as a laser prepulse, depending on its amplitude, can partially discharge the capacitor

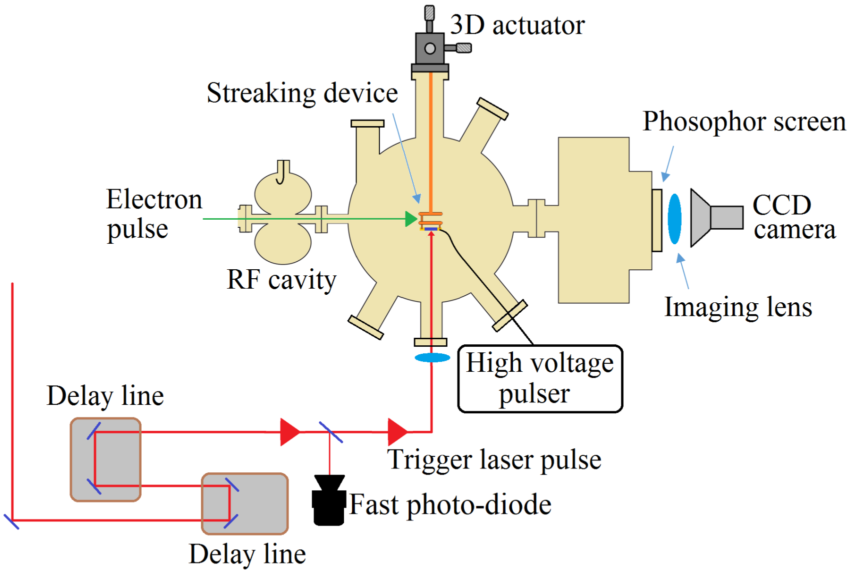

Figure 3.13: The electron pulse duration measurement setup. (Adapted from [114], with the permission of AIP Publishing.)

before the arrival of the main pulse, degrading the performance of the device.

There are two optical stages to change the timing of the triggering laser. One stage is longer with a less accurate reading and is used to observe the whole oscillation of the capacitor electric field (for example, the range of data in Figure 3.7 was obtained using this stage). During the experiment, this stage was used to locate the streak camera's first zero crossing of the capacitor electric field. This was achieved by first turning off the RF compressor to avoid the possible role of the RF cavity phase in accelerating or decelerating the electrons. Then we move the stage until the center of the streaked beam is at the position of the unstreaked beam on the screen. At this point, we use the second stage that is shorter but has a finer reading to accurately figure out the streak velocity and the sensitivity of the streak camera.

3.4.2 High voltage nanosecond pulser

The capacitor of the streaking device is initially charged by a high voltage pulse to minimize the risk of breakdowns in the GaAs photo-switch that is in parallel with the capacitor. Figure 3.14a shows the homemade pulser and figure 3.14b depicts its block diagram. The streaking device is connected to a high voltage switch, which in turn is connected to a high voltage DC supply through a buffering capacitor and two impedance matching resistors. The buffering capacitor stabilizes the amplitude of the high voltage pulse by suppressing the ripples caused by switching. The two 75 Ω non-magnetic resistors match the coaxial cable impedance and avoid high voltage reflections. A 6 μs TTL trigger signal comes from the laser synchronization and delay generator unit and is split into two paths, one of which is delayed by 50 ns and inverted, and in the other is kept the same. Then the two signals go to a logic AND gate. At the output of the logic gate, a 50 ns TTL signal is generated that triggers the high voltage switch. The 50 ns delay line is composed of several logic gates with certain propagation delays that add up to 50 ns. The logic gates are chosen and combined so that the state of the TTL output signal is the same as the input signal.

3.4.3 Evaluation of the GaAs photo-switch jitter

One important parameter that describes the performance of the streak camera for measuring ultrafast electron pulses is the timing jitter τ_s in the photo-switch due to the fluctuations in the triggering laser pulse energy. The timing jitter refers to the uncertainty in conduction band creation time when the laser pulse hits the switch. The timing jitter translates into a jitter in the deflection angle and can degrade the measurement if it is large in comparison with the electron pulse duration. To explain the effect of the jitter, let us consider the electric field across the capacitor around its first zero crossing that happens at $t = 0$. We have

$$E(t) = E_1\omega(t - \tau_s) = E_1\omega t - E_0, \tag{3.32}$$

where E_1 is the amplitude of the field, ω_0 the angular frequency of the streaking field oscillation. The jitter acts like a constant, random electric field E_0 that is added to the streaking field. This constant field deflects the electron pulse randomly. In a single shot measurement this deflection can be ignored if it is not

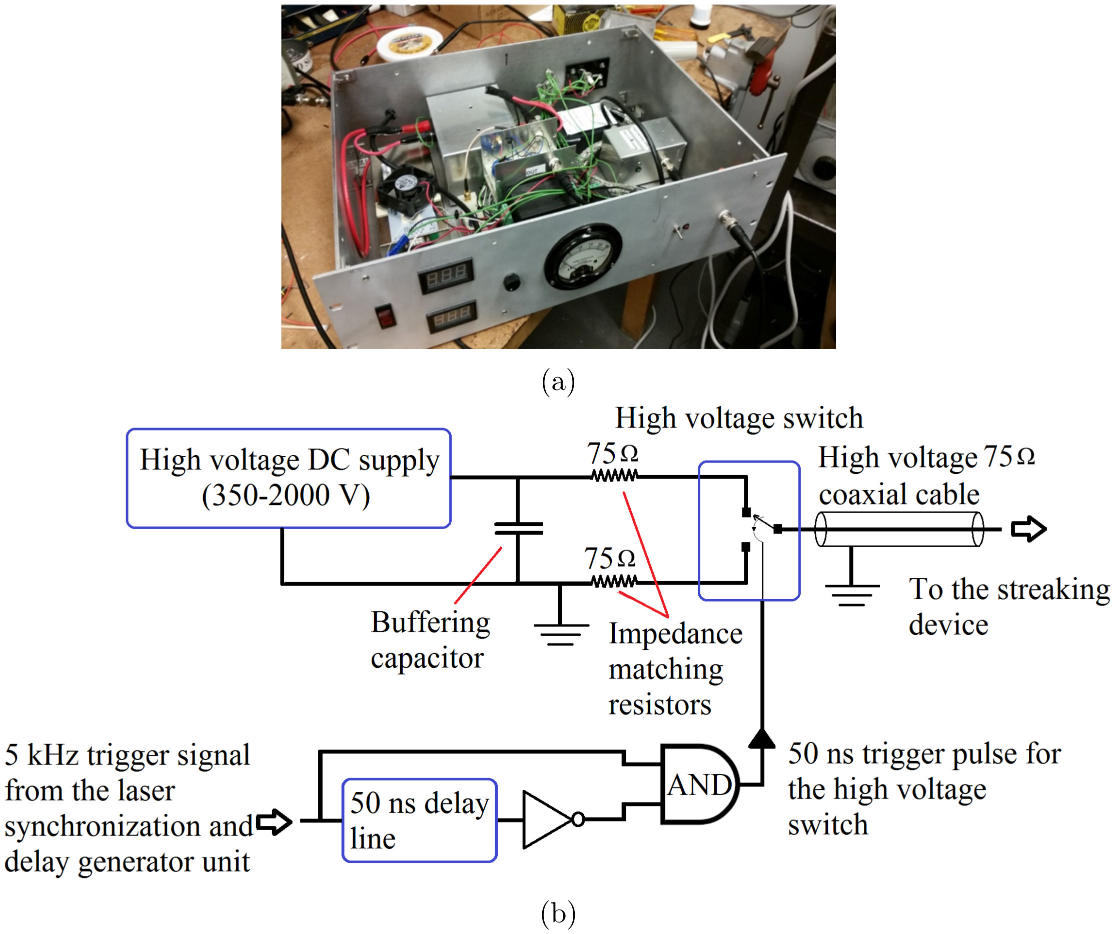

Figure 3.14: (a) A photo of the homemade high voltage nanosecond pulser. (b) block diagram of the device. (Reproduced from [114], with the permission of AIP Publishing.)

too big. However, the effect of the photo-switch jitter is worse if the measurement is not a single shot, as data collected over many pulses observe many random deflections due to the jitter, which increases the width of the streaked beam. The measured pulse duration τ is, therfore, a convolution of the actual pulse duration τ_e with the photo-switch timing jitter, i.e.,

$$\tau = \sqrt{\tau_e^2 + \tau_s^2}. \tag{3.33}$$

An experiment was conducted to evaluate the photo-switch jitter as a function of the laser pulse energy. We recorded the electron pulse time of arrival relative to the streaking field as a function of the trigger laser energy. Figure 3.15 shows the change in the time of arrival of the electrons with respect to the first zero crossing

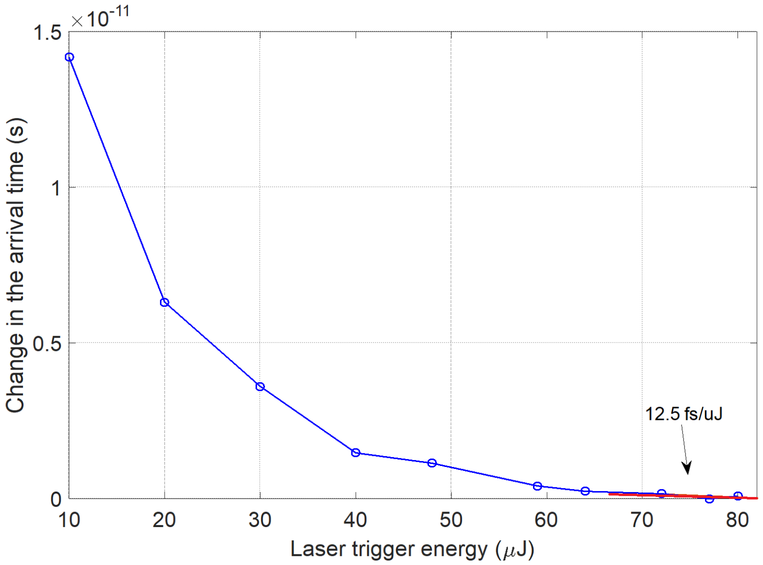

Figure 3.15: Change in the arrival time of electron with respect to the first zero crossing of the streaking field as a function of the triggering laser pulse energy. The red line is fitted to the last three points and its slope shows the rate of change in the arrival time vs the change in the laser pulse energy.

of the streaking field vs the trigger laser energy. The line that is fitted to the last three points on the graph has a slope of 12.5 fs/μJ. The measured laser power fluctuation is 0.5% RMS, so the expected timing jitter will be 5 fs RMS for 80 μJ pulses (the fluence of 850 μJ/cm^2), which is much lower than the electron pulse duration.

3.4.4 Evaluation of the streak velocity and the streak camera sensitivity

The optical setup that images the phosphor screen onto the CCD camera chip has a demagnification of 3.74 and the size of the camera pixels is 9.9 μm, so each pixel corresponds to 37 μm of the phosphor screen. The gamma factor in equation (3.16) is 1.176 for electrons accelerated to 90 kV kinetic energy; therefore, κ in equation (3.22) will be equal to 32.5 μm/V equivalent to 0.88 pixel/V. The position of the beam vs the corresponding delay in the trigger laser pulse for initial voltages $V_0 = 600$V, $V_0 = 800$V, and $V_0 = 1000$V around the first zero crossing of the capacitor electric field are shown in Figure 3.16. We fitted a line to each data set. The slope of each line gives the sensitivity defined by equation (3.23). By having the dimensions and the parameters of the imaging system, the sensitivities are converted to streak velocities. We found the streak velocities of 1.89 mrad/ps, 1.4 mrad/ps, and 0.94 mrad/ps, for initial voltages of 1000 V, 800 V and 600 V, respectively.

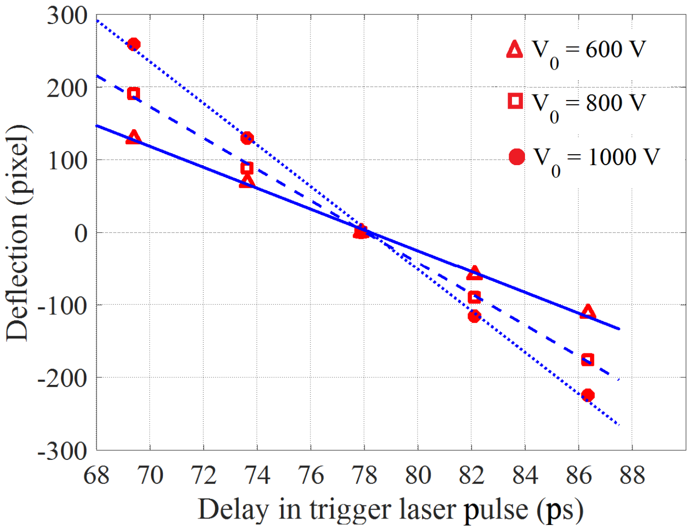

Figure 3.16: Deflection of the electron beam as a function of the delay in the photo-switch trigger laser pulse. The red triangles, squares, and circles show the measured deflection as a function of the trigger delay around the first zero crossing of the capacitor electric field for initial voltages of $V_0 = 600$ V, 800 V, and 1000 V, respectively. The corresponding values of sensitivities in equation (3.23) are obtained by fitting lines to the data points and are $\varsigma = 69.4$ fs/pixel, $\varsigma = 46.5$ fs/pixel, and $\varsigma = 34.9$ fs/pixel, respectively, equal to streak velocities of 1.89 mrad/ps, 1.4 mrad/ps, and 0.94 mrad/ps, respectively. These graphs can be considered the part of the oscillating graph shown in Figure3.7 around its first zero crossing for the higher initial voltages. (Reproduced from [114], with the permission of AIP Publishing.)

3.4.5 Electron pulse duration measurement

We measured the duration of pulses of 5×10^5 electrons that were focused on the screen for a better resolution. By focusing the electrons on the screen, the size of the unstreaked beam will be smaller and it will decrease the uncertainty of the measurement. However, focusing the beam on the screen will be at the price of a large beam on the target (streaking device). The electron beam was 2.4 mm FWHM on the streaking device and 192 μm (around 5.2 pixels) on the detector.

The measurement was done in an accumulation mode over 10 images each with 500 ms of exposure time to increase the signal to noise, where the electron pulses have a repetition rate of 5 kHz. For this case, the jitter in the arrival time of the electrons with respect to the triggering laser τ_{jitter} will be convolved in the pulse duration in the same way we discussed earlier (see Section 3.4.3) and similar to equation (3.33) we have

$$\tau = \sqrt{\tau_e^2 + \tau_{jitter}^2}, \tag{3.34}$$

since the jitter has a Gaussian distributed. The value of τ_{jitter} could be obtained if we could measure the pulse duration in a single shot experiment. It is worth mentioning that in gas phase experiments, the density of the target is by far lower in comparison to solid targets and the diffraction experiment cannot be done in a single shot mode since the number of scattering events and hence the signal to noise is considerably low. Thus, the experiment should be done in an accumulation mode, and consequently the temporal resolution will be determined by τ in equation (3.34) instead of τ_e.

In Figures 3.17a-3.17d, images of streaked and unstreaked electron pulses are shown. One can see (by comparing Figures 3.17a and 3.17b) that the streak length of the RF compressed pulse is significantly reduced compared to the streaked-uncompressed pulse. By projecting the images onto the x-axis, we can compare the change in the width of the compressed streaked pulse to the compressed unstreaked pulse in Figure 3.17c. The result is shown in Figure 3.17d. The pulse duration are extracted from theses one dimensional graphs.

The conventional method to extract the pulse duration is to fit Gaussian functions to both the unstreaked and streaked graphs in Figure 3.17d. If σ_{st} and σ_{us} are the standard deviations (STD) of the fitted Guassians to the streaked and unstreaked pulses, respectively, then the pulse duration can be determined by the deconvolution

$$\Delta t_{STD} = \varsigma \sqrt{\sigma_{st}^2 - \sigma_{us}^2}, \tag{3.35}$$

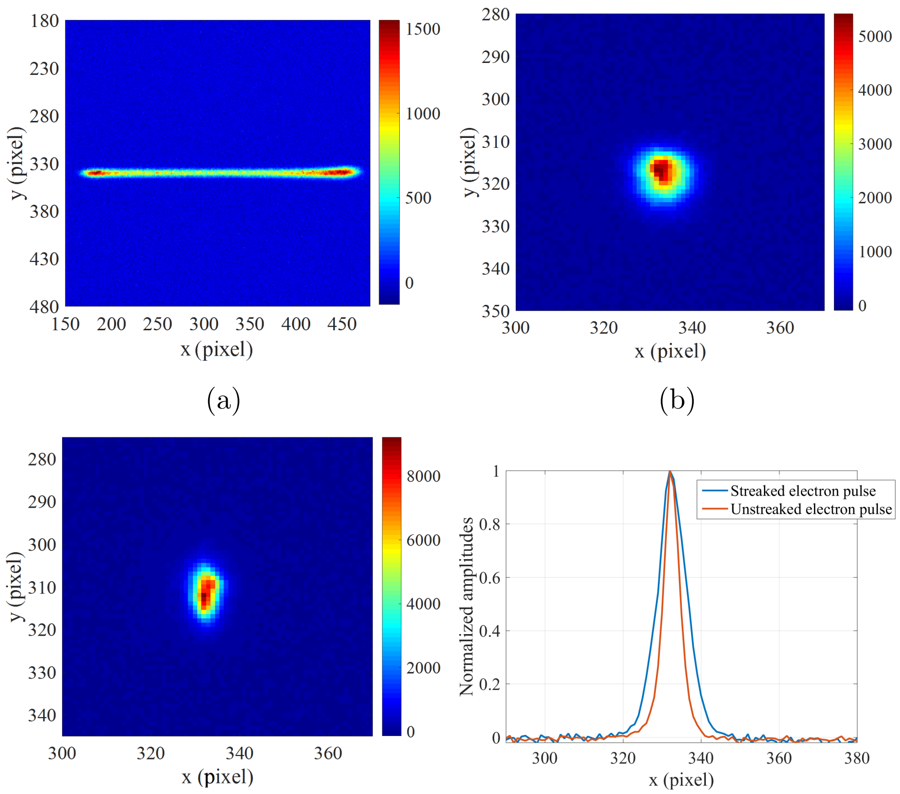

(a) (b)

(c) (d)

Figure 3.17: (a) Image of the streaked uncompressed electron pulse; (b) image of the streaked compressed pulse; (c) image of the compressed unstreaked beam; (d) the streaked and unstreaked compressed pulses integrated over the y axis. (Reproduced from [114], with the permission of AIP Publishing.)

where $\varsigma = 69.4\text{fs/pixel} = 0.94$ mrad/ps. The resultant pulse duration is $\Delta t_{STD} =$ 206 fs, which—when converted to a full width half maximum—gives $\Delta t_{FWHM} =$ 486 fs, with an uncertainty of 4 fs over the ten measurements. Similar calculations for the uncompressed pulse results in $\Delta t_{STD} = 8.8$ ps equivalent to $\Delta t_{FWHM} =$ 20.7 ps.

The other method to calculate the pulse duration is based on the mathematical model we developed in Section 3.3.5. We can project the blurred intensities obtained from equation (3.30) onto the x-axis. For the unstreaked beam we fit the function:

$$P^{blured}_{unstreaked}\left(x\right) = \int\limits_{-\infty}^{\infty} I^{blured}_{unstreaked}\left(x, y\right) dy \tag{3.36}$$

to the measured unstreaked beam to find the width of the Gaussian blur in equation (3.30). Similarly, we fit the function:

$$P_{streaked}^{blured}(x;\kappa') = \int\limits_{-\infty}^{\infty} I_{streaked}^{blured}(x,y;\kappa')\,dy \tag{3.37}$$

to the measure streaked pulse under the constraint:

$$\int\limits_{-\infty}^{\infty} P_{unstreaked}^{blured}(x)\,dx = \int\limits_{-\infty}^{\infty} P_{streaked}^{blured}(x;\kappa')\,dx \tag{3.38}$$

to determine the value of a the longitudinal semi-axis of the electron pulse that is a uniformly charged spheroid. Under the condition in equation (3.38), a is the only degree of freedom in the fit. The FWHM in this method is the FWHM of the function $A(z) = \pi r^2(z)$ for $r(z)$ given by equation (3.26) and is equal $\sqrt{2}a$. The longitudinal standard deviation for this distribution is equal to $a/\sqrt{5}$. The duration of the streaked compressed pulse shown in Figure 3.17b is $\Delta t_{STD} =$ 149 fs equivalent to $\Delta t_{FWHM} =$ 471 fs with an uncertainty of 4 fs over the ten measurements. For the uncompressed pulse in Figure 3.17a, the pulse duration is $\Delta t_{STD} = 4.6$ ps equivalent to $\Delta t_{FWHM} = 14.7$ ps.

Figures 3.18a and 3.18b demonstrate the comparision between the two methods to evaluate the pulse duration for compressed and uncompresse pulses. For shorter pulse durations, the results of the two methods are similar. This is because the blurring due to the finite resolution of the detector and the divergence of the electron beam make the streaking trace approximately Gaussian when the initial beam width is comparable to the width after streaking. For longer pulse durations, the Gaussian method does not fit the data very well and will give inaccurate values for the pulse duration. The measured distribution in Figure 3.18b also shows maxima near the edges of the distribution, which is most likely caused by the fact that the electrons deflected at the larger angles will start to experience the fringe fields of the capacitor and be deflected less than they would if the field remained uniform.

As we discussed earlier, the jitter in the arrival time of the electrons can blur

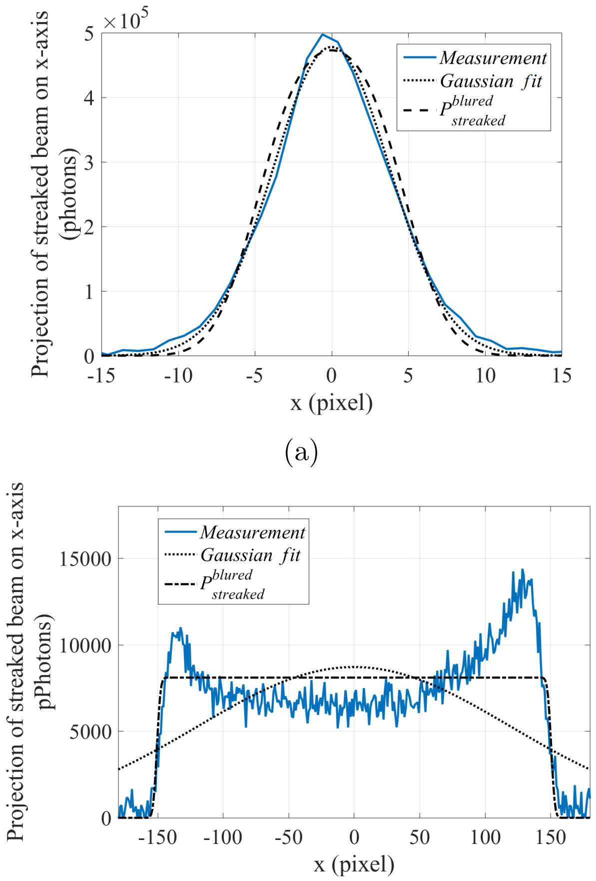

(a)

(b)

Figure 3.18: (a) The compressed streaked pulse and (b) the uncompressed streaked pulse, both integrated over the y-axis together with the Gaussian function and the developed model fitted to them. (Reproduced from [114], with the permission of AIP Publishing.)

the streaked beam on the detector. If we knew the value of the jitters, we could replace equation (3.30b) by

$$I^{blured}_{streaked}\left(x,y\right) = N \iint^{I_{streaked}} \left(x',y'\right) e^{-\frac{(x-x')^2}{2\left(\sigma^2+\sigma^2_{jitter}\right)}-\frac{(y-y')^2}{2\sigma^2}} dx'dy', \tag{3.39}$$

and keep equation (3.30a) unchanged to account for that blurring effect.

3.4.6 The streak camera resolution

The resolution of the streak camera depends on two parameters. The first one is the streak camera sensitivity that is measured by observing how much the beam center moves on the detector as we delay the trigger laser pulse. The other parameter is the size of the unstreaked beam on the detector. The larger the unstreaked beam, the less resolution of the device. The unstreaked beam for the experiment in Section 3.4.5 was 5.2 pixel wide FWHM. For a maximum sensitivity of ς=34.9 fs/pixels and a streaked pulse, which is only one pixel wider than the unstreaked beam, the electron pulse duration will be 118 fs. This value determines the resolution of the streak camera. However, it is possible to measure streaked pulses that are less than a pixel wider than the unstreaked pulses, provided the signal to noise is sufficiently high.

3.4.7 Minimization of the electron pulse duration

The electron pulse duration, at the position of the target, depends on the following parameters:

1. the number of electrons per pulse;
2. the traverse divergence of the beam;
3. the phase and amplitude of the RF cavity longitudinal electric field; and
4. the timing jitter between the electrons and laser.

Experimentally, the shortest pulse duration is obtained with lower currents in the first coil and higher currents in the second coil in the setup (see figure 2.1 for the position of the coils). In this way, the electron pulse will have a smaller diameter on the axis of the RF cavity that is essential for optimum compression. In this case, the beam will have a larger divergence and we should keep the number of electrons lower to make the size of the beam small on the detector. As we discussed before, the fast jitter in the RF cavity field will increase the measured pulse duration too. However, here, we will focus on experimentally obtaining the optimum values for the amplitude and the phase of the RF cavity for the shortest pulse duration.

The pulse compression will be the best when the center of the electron pulse coincides with the zero crossing of the RF cavity longitudinal electric field. In this case, a symmetric force will be applied to the front and back sides of the pulse and it will self-compress at some distance from the cavity. We call the phase of the RF cavity for which this symmetric force is applied to the electron pulse, the phase zero. At phase zero, the total kinetic energy of the pulse will not be affected by the RF cavity compression, and the amplitude of the compressing field only affects the temporal focal length of the cavity, i.e., higher amplitudes causes the electron pulse to temporally focus closer to the RF cavity and vice versa.

In the experiment, we first determine the phase zero and the key to find it is to use the fact that the energy of the electron pulse is the same after and before the RF cavity. This means that if we ignore the delay caused by the RF cavity, the streaked and unstreaked pulse centers should coincide on the detector. We, therefore, adjust the phase of the RF cavity so that the center of the streaked beam falls onto the center of the unstreaked beam. There are two phases for which this coincidence happens, and for one of them, the streak length is by far larger than the other because we are maximally increasing the pulse duration at the incorrect phase. In reality, the delay caused by the RF cavity might be considerable; therefore, this method will not give the right phase zero. Here, we analytically calculated the delay caused by the RF cavity.

Let us consider a single electron entering the RF cavity at its phase zero. At that time, the the electric field of the RF cavity changes linearly by time, and the equation of motion in the longitudinal direction will be

$$\frac{dp_z}{dt} = m\frac{d\gamma v_z}{dt} = eE_0\omega_0 \left(t - t_0\right). \tag{3.40}$$

By integrating equation (3.40) over time, we have

$$\gamma v_z \left(t\right) = \gamma_0 v_{z0} + \frac{e}{m}E_0\omega_0 \left(t - t_{in}\right)\left[\frac{1}{2}\left(t + t_{in}\right) - t_0\right], \tag{3.41}$$

where $v_{z0} = v(t_{in})$ is the initial velocity of the electron at the cavity entrance at time $t = t_{in}$. At the phase zero, the electron leaves the cavity at time t_{out} with the same velocity v_{z0} and momentum; therefore, from equation (3.41) we should have

$$t_0 = \frac{1}{2}\left(t_{exit} + t_{in}\right). \tag{3.42}$$

We define $Y(t)$ being the right-hand-side of equation (3.41) for t_0 replaced by equation (3.42):

$$Y(t) = \gamma_0 v_{z0} + \frac{e}{m} E_0 \omega_0 (t - t_{in})(t - t_{out}). \tag{3.43}$$

Then from equation (3.41), the velocity of the electron at time t will be

$$v_z(t) = \frac{Y(t)}{\sqrt{1 + \frac{Y(t)^2}{c^2}}}. \tag{3.44}$$

For l_{cav} being the length of the RF cavity, we know that

$$l_{cav} = \int_{t_{in}}^{t_{exit}} v_z\left(t\right) dt = \int_{t_{in}}^{t_{exit}} \frac{Y\left(t\right) dt}{\sqrt{1 + \frac{Y^2(t)}{c^2}}}. \tag{3.45}$$

This equation determines the moment the electron exits the cavity t_{exit}. If the RF cavity is off, the exit time $t^{'}_{exit}$ will be

$$t^{'}_{exit} = \frac{l_{cav}}{v_{v0}} + t_{in}. \tag{3.46}$$

The difference between t_{exit} determined by equation (3.45) and $t^{'}_{exit}$ in equation (3.46) is the delay caused by the RF cavity at the zero phase. The maximum energy that an electron can gain or lose by the field of the RF cavity is in the order of $\omega_0 \Delta t e E_0 l_{cav}$ where Δt is the amount of time that the electron spends inside the cavity and we approximate it by $\frac{l_{cav}}{v_z}$. If an electron pulse with 10^5 eV kinetic energy, has a one percent energy spread, then the electric field of the cavity should be in order of 2×10^5 V/m, for $\omega_0 = 6\pi \times 10^9$ rad/s and $\Delta t \approx 4 \times 10^{-12}$ s. Figure 3.19 shows the delay caused by the RF cavity as a function of its longitudinal electric field amplitude. The delay at the phase zero is under 60 fs. Therefore,

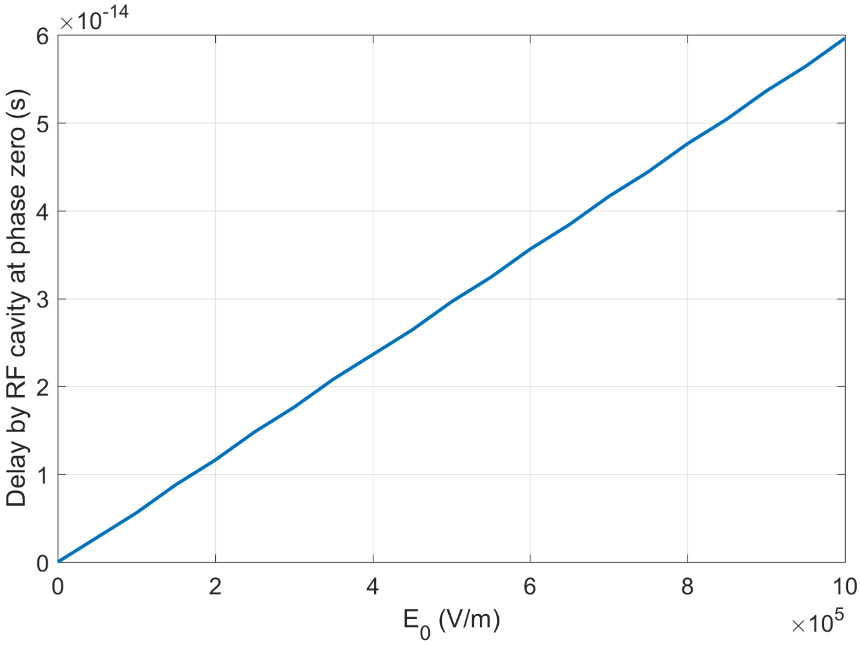

Figure 3.19: The single electron delay $(t_{exit} - t'_{exit})$ caused by the RF cavity longitudinal electric field at its phase zero.

the corresponding deflection caused by the streaking device with a sensitivity of 69.4 fs/pixel will be under one pixel. We solved the equation (3.45) numerically to obtain t_{exit}.

Once we determine the phase zero, we change the amplitude for the shortest streak length on the detector. This procedure will give the shortest pulse duration at the position of the streaking device. Figure 3.20 shows the electron pulse duration as a function of the RF cavity input power for different phases. The shortest pulse duration happens at the phase zero.

3.4.8 Evaluation of fast and slow jitters

As we mentioned before, we cannot measure the fast jitters in the arrival of the electrons caused by the jitter in the RF cavity electric field, since we cannot do a single shot measurement. However, based on numerical simulations using the General Particle Tracer code, the electron pulse duration on the target should be around 250 fs for electrons and 100 fs for 5×10^5 electrons. Nevertheless, we have observed that the temporal resolution does not improve from 350 fs when reducing

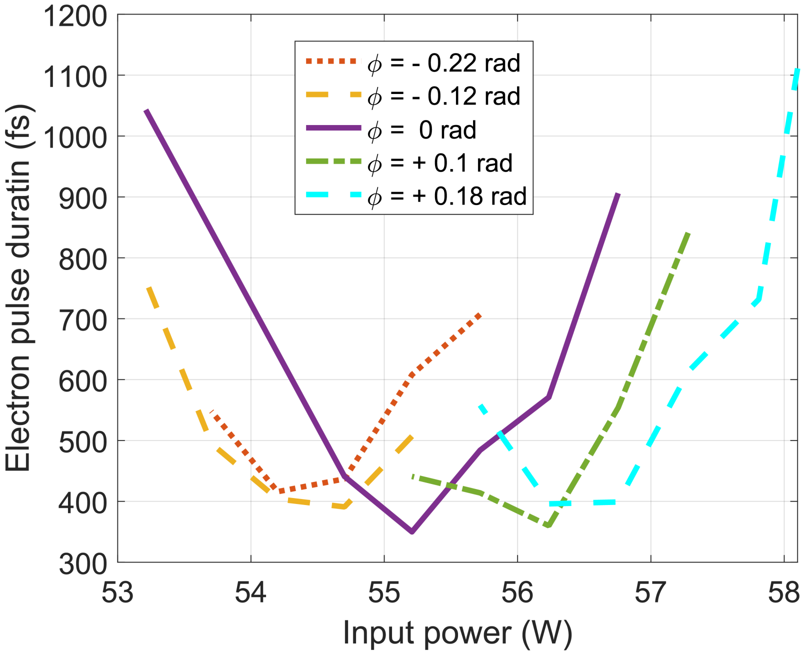

Figure 3.20: Electron pulse duration as a function of the phase and input power of the RF cavity. The shortest pulse duration happens at the phase zero. (Structural Dynamics, Vol. 4, 044022, (2017); used in accordance with the Creative Commons Attribution (CC BY) license.)

the pulse charge from 5×10^5 to 10^5 electrons, which suggests a large contribution from the timing jitter. To improve the resolution of the setup, attempts should be made to reduce the fast jitters. On the other hand, the slow jitters or drifts can be measured by the streak camera. Figure 3.21 shows the center of the electron beam on the detector as we delay the triggering laser in steps of 85 fs around the first zero crossing of the capacitor electric field with the initial voltage of 600 V. We fitted a line to the data points with the root-mean-square (RMS) fitting error of 70.3 fs. The slope of the fitted line is 65.3 fs/pixels, which is close to what we got from Figure 3.16 for V0 = 600 V. The measured fluctuations in the deflection can be attributed to the slow component of the timing jitter in the experiment. In this measurement, each data point is an average over ten consecutive frames each with an integration time of 500 ms. Accordingly, we can monitor the changes in the arrival time of the electron pulses with respect to the trigger laser pulse down to around 70 fs RMS with a measurement time of a few seconds.

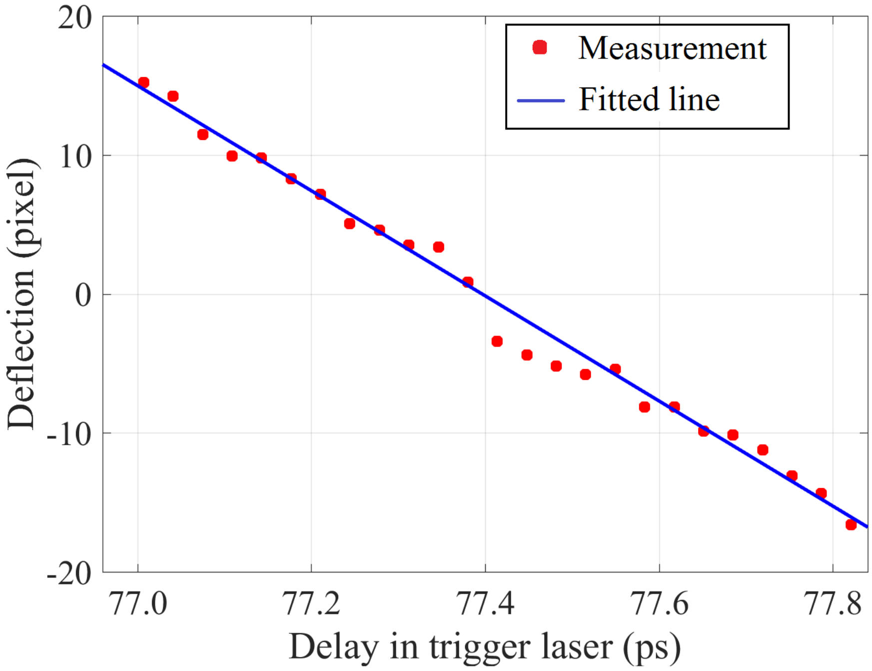

Figure 3.21: Position of the electron beam center as a function of the trigger laser delay. The initial voltage of the capacitor was 600 V. The trigger laser pulse was delayed in steps of 85 fs. This graph is the central part of the graph shown in Figure 3.16 for V0 = 600 V and it shows the fluctuations in the arrival time of the electron pulses relative to the laser pulses. (Reproduced from [114], with the permission of AIP Publishing.)

3.5 Summary

We constructed and characterized a laser-activated femtosecond streak camera with a streak velocity of 1.89 mrad/ps for electrons 90 keV kinetic energy. A full circuit analysis of the streaking device was provided and all the equivalent circuit parameters were extracted to describe the oscillating field. The device produces a streaking field of 3 MV/m with an oscillation frequency of 3.49 GHz and a quality factor of 3.85. The quality factor was limited mostly by the resistance of the GaAs Ohmic contacts. We developed a general mathematical model that provides an accurate method to evaluate the pulse duration. We measured pulse duration as low as 350 fs FWHM and showed that we can measure timing drifts that are as low as 70 fs RMS. Based on the setup parameters, we expect that the streak camera can measure a pulse duration around 100 fs. The resolution of the device could be further improved by increasing the voltage across the capacitor, reducing the size of the device to increase the discharge frequency and by improving the detection system to reduce the integration time. Using an image intensifier and a low noise detector can allow for single shot measurements.

Chapter 4

Diffraction Experiment and Setup Calibration

4.1 Introduction

In this chapter, we will focus on the gas injection and pumping system, the diffraction experiments we did to calibrate the setup, and the temporal overlapping of the pump and probe. The gas stream, the electron beam, and the laser beam should all intersect at one point in space, which we call the center of scattering. The gas stream should be localized at the scattering center, meaning that the density should be highest there and drop off quickly for any deviations from the center. Here, we consider two types of gas nozzles that can provide such a gas stream commonly referred to as the gas jet. The gas needs to be quickly removed from the chamber for two main reasons. First, both the acceleration stage and RF cavity need ultra-high vacuum (UHV) to function properly. Second, we want to minimize the probability of electron scattering from the gas molecules everywhere else. The background gas is minimized by directing the gas jet into a high-speed diffusion pump. We separate the chambers by small apertures and differentially pump each one to ensure UHV outside the sample chamber. The electron detection setup including a phosphor screen, a lens, and a low-noise high-gain charge coupled device (CCD) camera is also explained in this chapter. Two static diffraction experiments were done to calibrate the detector. And last, we determined the timing between the laser pulses and the electron pulses by two techniques for normal and tilted intensity front laser pulses. For the former, we generated plasma by focusing the laser beam on the gas thus creating an electric field gradient within the gas itself, effects of which can be seen in the detected electron beam. For the latter, we generated a transient space charge field and a surface polarization on the edge of a copper pinhole under the nozzle by the laser which deflects the electron beam.

4.2 Nozzle, gas injection and differential pumping systems

The setup block diagram is reviewed in Figure 4.1. This setup is equipped with one diffusion pump and four turbo pumps with locations indicated in that figure. A photo of the scattering (target) and the detection chambers, which are connected to each other by a flexible tube (bellows) is shown in Figure 4.2. The gas is injected into the target chamber from the top through a nozzle whose position can be adjusted by a three-dimensional moving stage. This chamber also hosts the streak camera and the electron beam collimator, which are not shown in the figure for clarity. The chamber is pumped by a diffusion pump (Edwards, Diffstak 250/2000P) from the bottom that is backed by a two-stage rotary pump (Edwards, E2M40). The diffusion pump is connected to the chamber through a pneumatically actuated isolation valve, that can separate it from the rest of the setup. The detector chamber is pumped by a turbo pump (Pfeiffer, HiPace80). We measure the pressure in the target chamber by a hot-filament ionization gauge (Kurt J. Lesker, KJLC354401YF). While there is no gas injection and the diffusion pump valve is open, the target pressure goes down to $10^{-8} - 10^{-9}$ Torr. The gas is controlled by a mass flow controller and the pressure is monitored both behind the nozzle and in the target chamber. Pressure in the target chamber is kept below 2×10^{-4} Torr to prevent pump oil from defusing into the chamber.

The RF cavity sits right before the target chamber and is connected to it by a flexible tube and a 3 mm aperture (see Figure 4.1). A turbo pump (Leybold, TW 70 H) is put before the RF cavity and a 5 mm aperture separates them from the acceleration and beam focusing stage of the setup (see Figure 4.1). We measure the pressure of the RF cavity by another ionization pressure gauge to be around 10^{-9} Torr without gas injection. The maximum target chamber pressure of 2×10^{-4}

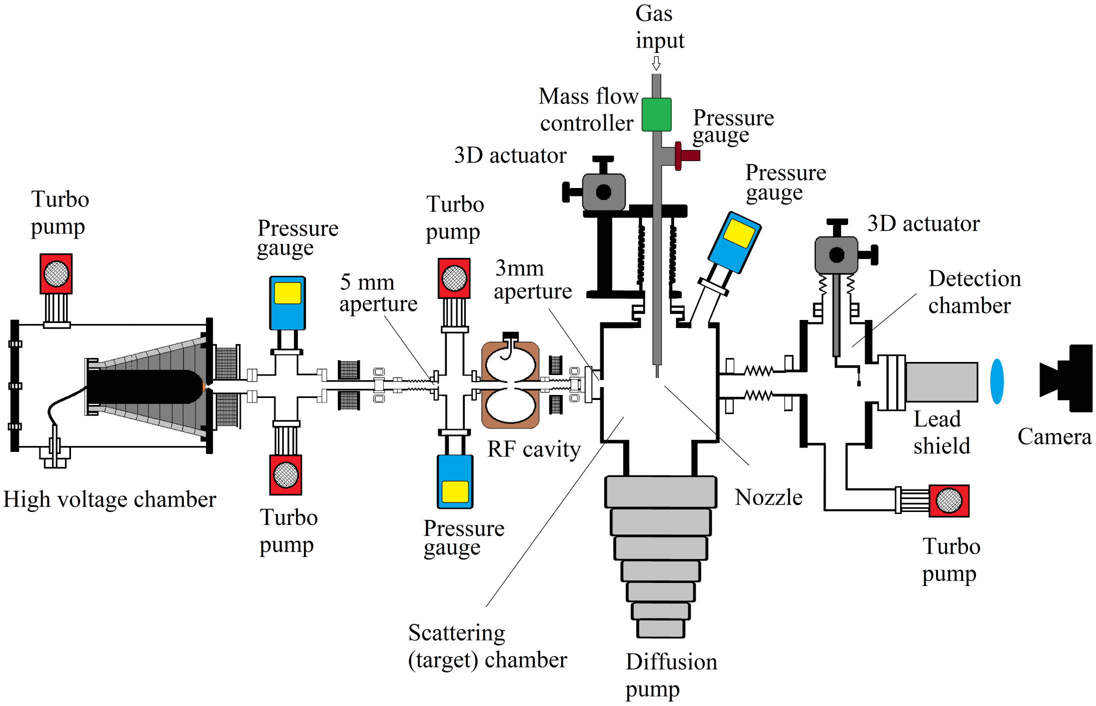

Figure 4.1: A block diagram of the UED setup that shows the the five pumps connected to the setup.

Torr corresponds to pressure in the RF cavity of up to 10^{-6} Torr. There is another turbo pump on a cross junction for the front side of the high voltage chamber, where the the anode and cathode are hosted. We measure the pressure over that area by another ionization gauge. The pressure is around 10^{-7} Torr and does not change appreciably when we inject the gas. The pressure gauge is connected to a safety interlock system that works such that if the pressure goes above 10^{-6} Torr around the cathode, it shuts down the high voltage and the RF cavity. The high voltage chamber is pumped from the backside by the fourth turbo pump to ensure an even pressure throughout the acceleration chamber.

4.2.1 Gas nozzles

The nozzle should be able to deliver a collimated beam of cold gas namely a gas jet with a sufficiently low width. There are two types of nozzles for this purpose: capillary nozzles and converging-diverging (CD) nozzles. The former is simpler to construct and hence less expensive but its performance is not generally as good as

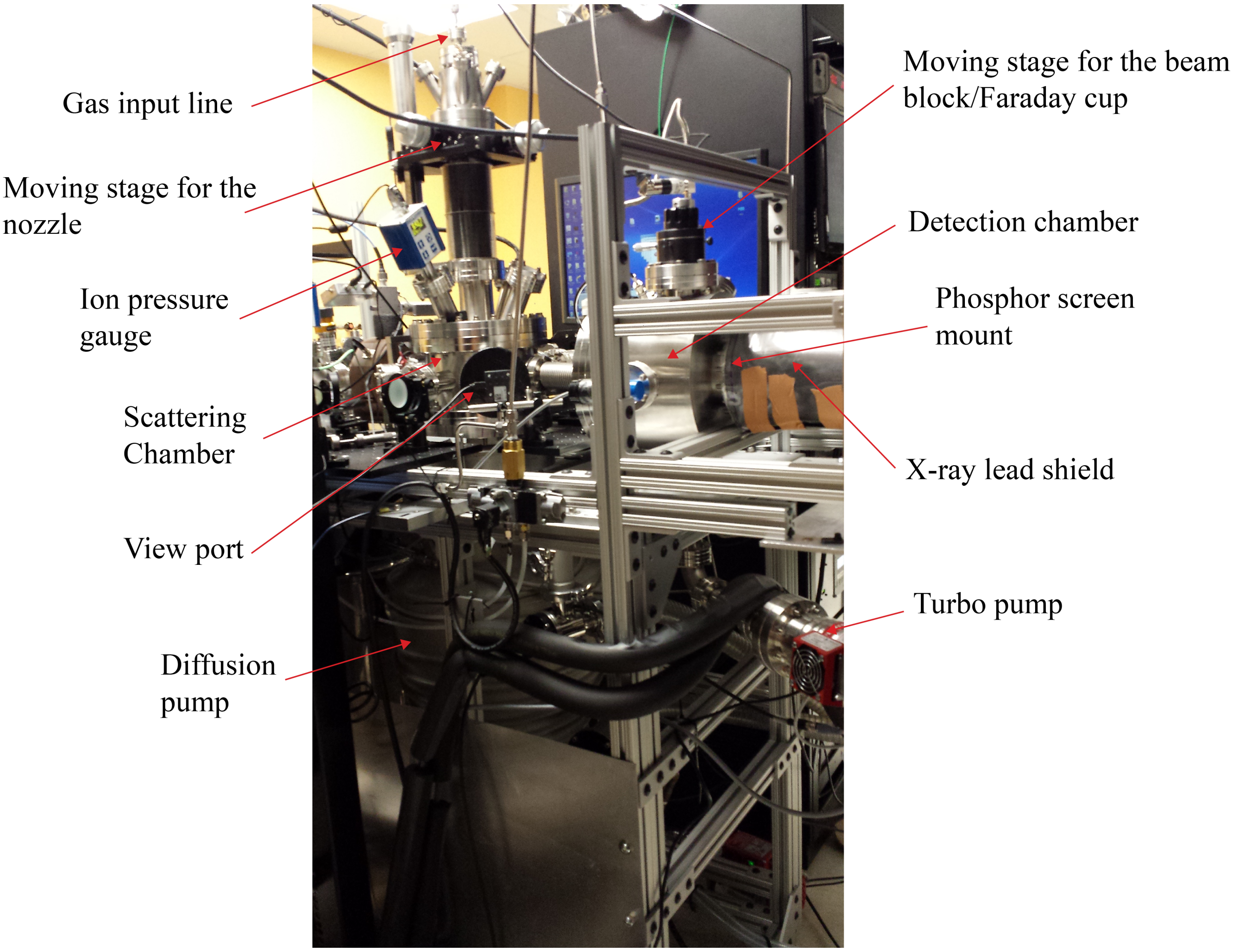

Figure 4.2: A photograph of the target and detector chambers.

a CD nozzle in terms of the the gas temperature and collimation. Figure 4.3 shows the schematic of a homemade capillary nozzle. A stainless tube with an outer and inner diameters of 200 and 100 μm, respectively, and a length of 2 cm crosses a very small needle-pierced hole in a cylindrical piece of rubber. By use of a set screw and an aluminum disk with holes at their centers, the rubber is squeezed tightly around the capillary and a vacuum seal is obtained. The flow of a compressible gas in a constant area tube, where the friction due to the tube wall cannot be neglected, is modeled by the Fanno flow, named after the Italian mechanical engineer Gino Girolamo Fanno [120]. This type of nozzle, for their particular application in gas phase electron diffraction experiments, has been analyzed [121, 122]. The result indicates that a nozzle whose length is much longer than its diameter provides a low temperature sonic or subsonic gas jet.

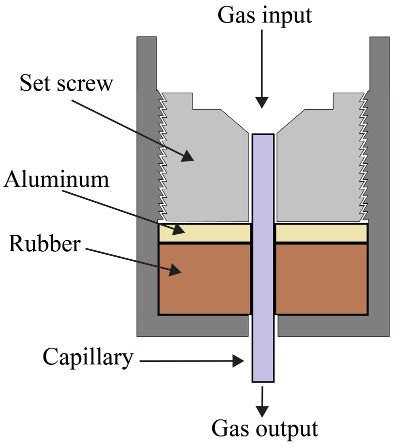

Figure 4.3: Schematic of homemade capillary nozzle.

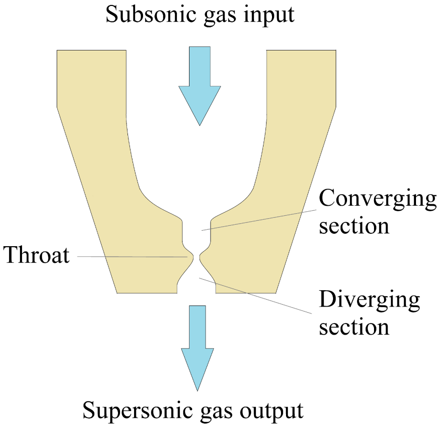

Figure 4.4: Schematic of a CD nozzle.

The other type of nozzle that we use for diffraction experiments is the CD or de Laval nozzle shown in Figure 4.4. This nozzle is employed when a supersonic gas stream with a lower temperature is required. Briefly, the convergence of the tube will increase the flow speed since the mass flow rate remains constant. The design is such that the flow speed reaches the speed of sound at the throat that is shown in the figure. The gas pressure, after the throat, decreases resulting in an increase in the flow speed. For injection of gas by a CD nozzle into vacuum, formation of a sonic flow at the throat is a sufficient condition for a supersonic flow at the exit. The design and the physics of this nozzle is well documented [123–125].

In Section 4.4.2, we will explain how to determine the gas jet diameter and density by use of the diffraction pattern.

4.3 Phosphor screen and optical imaging system

In our setup, we used Gd_2O_2S:Tb phosphor commercially known as P43 or GADOX to detect 90 keV electrons, as P43 has proved to be an efficient electron detector [126, 127]. This phosphor emits green light, peaked at 545 nm, with about $12 - 20\%$ conversion efficiency and has a 10% decay time of 1.5 ms and 1% decay time of around 3 ms which is almost intensity independent [128–132]. The mentioned efficiency leads to creation of 4700 to 7800 photons per electron. However, to get a highest number of photons per electron, the thickness of the phosphor screen should be optimized for a given energy of the incident electron [133]. Generally, we prefer to increase the thickness to maximally absorb all the electrons and generate as much light as possible. But the light can be absorbed by the phosphor screen itself if the screen is too thick. The other problem is that the light generated at any point inside the phosphor propagates isotropically and there is a finite chance of multiple scattering [129], leading to a poor spatial resolution if the screen is too thick. Calculations, by an experimentally derived transfer function (point spread function) of the screen, have shown that the resolution of a 10 μm thick phosphor screen (P43) is around 63 μm FWHM for a 120 keV electron hitting the screen [129].

The density of P43 is 7.3 g/cm^3 [134] but cautious is warranted to use this number to determine the optimum thickness of the screen from the literature. That is because P43 exists in a powder and is deposited on a surface by use of a binding medium. Therefore, the packing factor of the phosphor is smaller in the binding medium than in its crystalline form. So the actual density of the phosphor screen can be significantly lower that 7.3 g/cm^3 [135, 136]. The convention is to express the the desired thickness of the phosphor screen as a coating weight in the unit of mg/cm^2 and not the actual coating thickness since the binding medium might be different from one manufacturer to the other. We used 3 mg/cm^2 layer of P43 with a grain size of 3μm deposited on a Pyrex glass disk with a thickness of 4.8 mm as was recommended by the manufacturer (Beam Imaging Solutions) for highest light intensity and a resolution not much larger than 100 μm. The substrate glass diameter was 63.5 mm with the 40 mm diameter deposited phosphor at its center. There is an aluminum coating layer on top of the phosphor screen for three reasons: 1) preventing light (from laser or other sources) to pass through the phosphor screen; 2) reflecting the back propagating light from the phosphor screen into the forward direction; and 3) preventing charge accumulation on the phosphor. In calculating the aluminum coating thickness, we deal with two concepts: the stopping power and the skin depth. Stopping power is due to the retarding force applied to a moving electron by the ambient atoms and molecules, and is defined as the amount of kinetic energy E_k that an electron loses per unit of length as it travels inside a matter [137]. For 90 keV electrons traveling inside pure aluminum, the stopping power is equal to 8910 keV/cm [138, 139]; hence, a 90 keV electron will lose 0.1% of its energy by traversing a 1000 Å thick aluminum layer. The skin depth is the distance over which a beam of light loses its energy by a factor of $1/e$ while penetrating into a material and depends on the constitutive parameters of the material and the light wavelength. From the date given in [140], we calculated the penetration depth to be 54.5 Å for 99.99% pure aluminum and a light wavelength of 546 nm. Therefore, only around 0.1% of light transverse a 500 Å thick aluminum foil, and it becomes negligible for a 1000 Å thick aluminum foil. On top of our phosphor screen, there is a around 1000 Å thick aluminum. The aluminum coating is thicker on the edge of the glass substrate for a better and more reliable connection to ground. Figure 4.5a and 4.5b show the schematics of the phosphor screen holder from the side and vacuum points of view. Figure 4.5c is a photograph of the screen holder from the room side. The electrons that are stopped in the phosphor screen or even in the glass substrate will radiate x-rays known as the bremsstrahlung radiation, which were detected in our setup. The whole phosphor screen and the light blocking tube are covered by a 2 mm thick lead shield to stop the x-rays (see Figure 4.2).

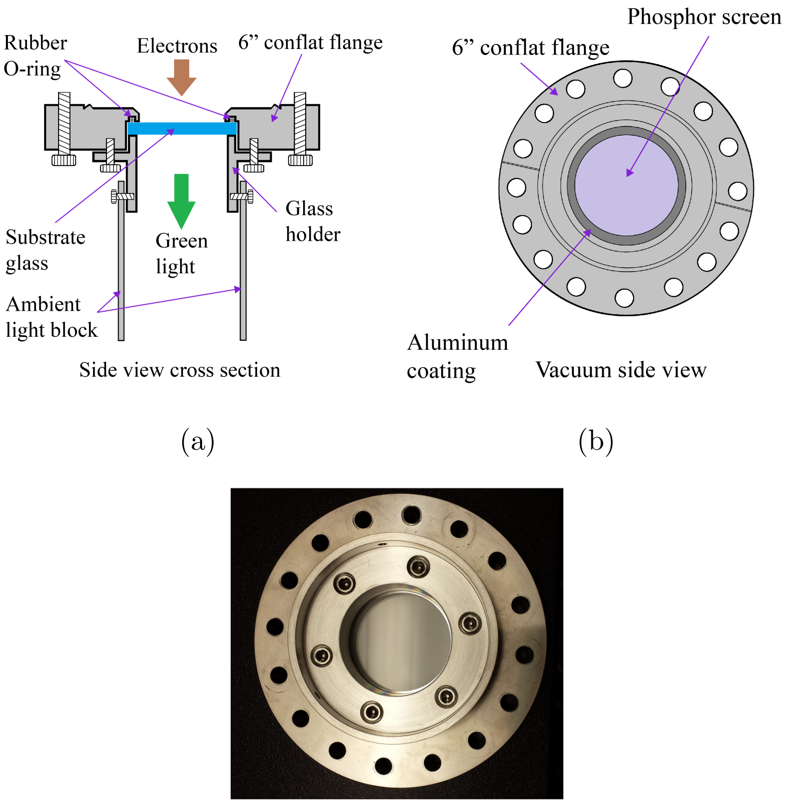

(a) (b)

(c)

Figure 4.5: (a-b) schematic of the phosphor screen holder from two views. The O-ring seals the vacuum. The aluminum coating on the edge is connected to the flange. There is tube that goes all the way to the camera blocking the ambient light. (c) A photograph of the screen holder from the room side. The aluminum coating on the edge is observable on this side too. The ambient light block is not mounted.

The phosphor screen is imaged onto a high-gain low-noise 16 bit CCD camera (Andor, iXon Ultra 888) by an aberration-free optical lens (Nikon, NIKKOR 50 mm f1/2). The camera chip has 1024×1024 pixels with a pixel size of 13μm. The camera uses a four-stage Peltier cooling assembly to reduce the temperature of the CCD chip. The heat from that cooling assembly is removed by a water chiller (ThermoTek, T255P).

4.4 Static diffraction pattern, and setup calibration

We performed static diffraction experiments on molecular nitrogen (N_2) and Trifluoroiodomethane (CF_3I) to calibrate the detector. Calibration of the detector means to determine that one pixel of the detector corresponds to how much of momentum transfer, s or the deflection angle. We used the data from CF_3I to calibrate the detector and then verified the calibration by measuring the bond length from the diffraction pattern of N_2.

Let us return to equation (1.58) for the diffraction pattern from an ensemble of randomly oriented molecules, which is repeated here for convenience:

$$I = M\sum_{i=1}^{N}|f_i|^2 + M\sum_{i=1}^{N}\sum_{j\neq i}^{N}|f_i||f_j|\cos(\eta_i - \eta_j)\frac{\sin sr_{ij}}{sr_{ij}}. \tag{4.1}$$

In general, if we have an N-atom molecule, the first term on the right-hand side of this equation, I_{atomic}, will have N terms, while the second term $I_{molecule}$ will have $\frac{1}{2}N(N-1)$ terms. For CF_3I, we have

$$I_{atomic} = |f_C|^2 + |f_I|^2 + 3|f_F|^2, \tag{4.2a}$$

and

$$I_{molecule} = |f_C||f_I|\frac{\sin sr_{CI}}{sr_{CI}} + 3|f_C||f_F|\frac{\sin sr_{CI}}{sr_{CI}} + 3|f_I||f_F|\frac{\sin sr_{FI}}{sr_{FI}} + 3|f_F||f_F|\frac{\sin sr_{FF}}{sr_{FF}}, \tag{4.2b}$$

where we are interested only in $I_{molecule}$. As we saw in equation (1.47), the scattering amplitude of each atom decreases proportionally to $\frac{1}{s^2+\mu^2}$ as s increases. Hence, for larger values of s, the detected signal will be proportional to $1/s^5$. Since I_{atomic} is known, the convention is to define the modified molecular scattering as

$$sM(s) = s\frac{I_{molecule}}{I_{atomic}} = s\frac{I - I_{atomic}}{I_{atomic}}. \tag{4.3}$$

In fact, equation (4.3) can be seen as a weighted summation of sine functions, each with a period of $\frac{2\pi}{r_{ij}}$ where r_{ij} is any of the inter-atomic distances. In the experiment, however, in addition to I_{atomic}, we have to subtract the background signal too. That background can be the inelastic scattering or any light leakage to the detector. It also can be x-rays generated by the electrons hitting the beam collimator, the beam block or even the phosphor screen. The P43 phosphor screen can generate light from x-rays too [141]. We rewrite equation (4.3) as

$$sM(s) = s\frac{I_{molecule}}{I_{atomic}} = s\frac{I - I_{atomic} - I_B}{I_{atomic}}, \tag{4.4}$$

where I_B being the background signal to account for the mentioned background.

4.4.1 Center of diffraction and azimuthal averaging of diffraction pattern

Figure 4.6a shows the static electron diffraction pattern of CF_3I detected by the CCD camera after subtracting the background noise. The background noise is any signal we receive while the gas is not injected in the path of the electrons. The data was recorded over an exposure time of 20 s. Since the image has a large dynamic range (2^{16}) and the signal decreases proportionally to $1/s^5$ from the center of the diffraction, we can take the logarithm of the image for a better illustration. Care should be taken for the logarithm transformation, since after the background subtraction some of the pixels might have a negative value. In that case, we add a constant to all of the pixels such that the minimum pixel value is equal to one. Suppose the dynamic range of the pixel values in which we are interested is $[P_1, P_2]$. Then, the logarithm transformation of

$$I_{log} = A\frac{\ln I - \ln P_1}{\ln P_2 - \ln P_1} \tag{4.5}$$

will map pixel values in the range of $[P_1, P_2]$ onto the range of $[0, A]$, where A is an arbitrary constant. One example for dynamic range assignment is when there are dead or hot pixels. In that case, P_1 can be the second minimum in the image, and P_2, the second maximum. In Figure 4.6b, the diffraction pattern of CF_3I is sketched in a logarithmic scale.

The diffraction patterns of randomly oriented molecules (or any other cylin-

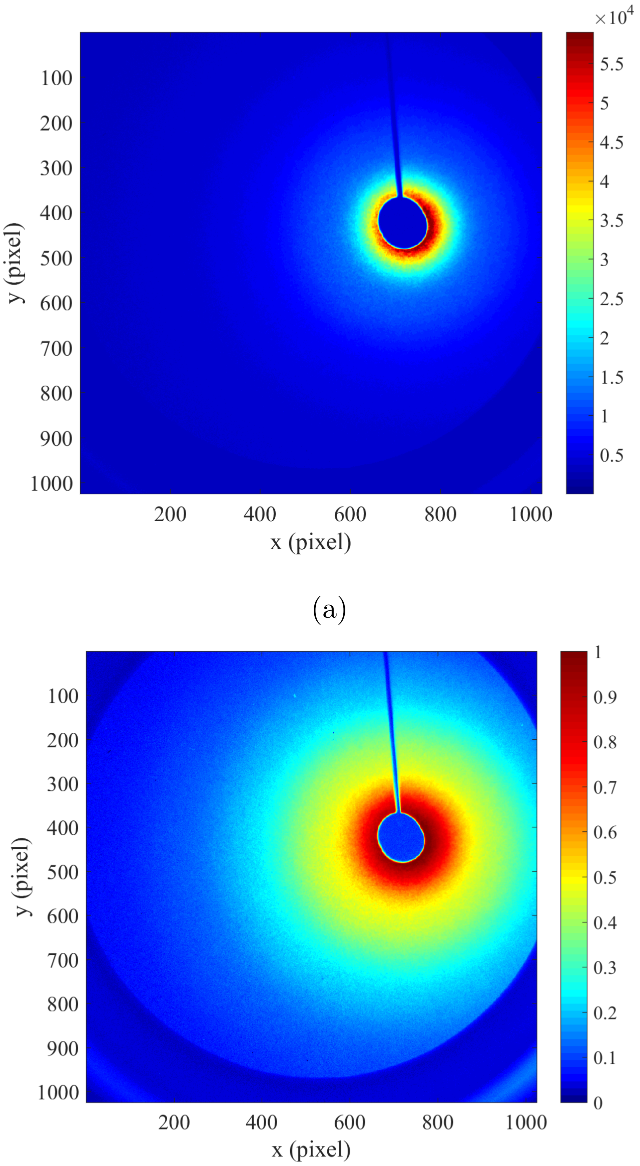

(a)

(b)

Figure 4.6: (a) Diffraction scattering from CF_3I after background subtraction (b) the same diffraction pattern in logarithmic scale. In this figure, we chose $P_1 = 3000$ which is around the signal level at the aluminum ring, and $P_2 = 58,988$ which is the maximum pixel value in the image. We also chose $A = 1$ (see equation (4.5).)

drically symmetric potential) have an azimuthal symmetry over which we may average to get a one-dimensional diffraction signal. But before doing that, we need to know the center of symmetry on the detector to which we refer as the diffraction center. That center is behind the beam block; hence, we need to determine it indirectly. We use the gradient of a diffraction pattern to determine the diffraction center.

Let us show the gradient of a diffraction image I by vector $\vec{G}(m,n)$, i.e.,

$$\vec{G}(m,n) = \nabla I = G_x(m,n)\hat{x} + G_y(m,n)\hat{y}, \tag{4.6}$$

where the indices m and n refer to a pixel location on the CCD chip, and $\hat{x}$ and $\hat{y}$ are unit vectors in the directions of rows and columns, respectively. The gradient shows the direction of maximum change in the detected light. In other words, a line on the CCD chip, with the equation

$$y - n = \frac{G_y(m,n)}{G_x(m,n)}(x - m) \tag{4.7}$$

will cross the diffraction center. As a result, a second line

$$y - n' = \frac{G_y(m',n')}{G_x(m',n')}(x - m'), \tag{4.8}$$

for $m' \neq m$ and $n' \neq n$, will intersect the first line at the center of diffraction. We solve the two line equations for the diffraction center (x_c, y_c):

$$x_c = \frac{m' - m + \frac{G_y(m,n)}{G_x(m,n)}m - \frac{G_y(m',n')}{G_x(m',n')}m'}{\frac{G_y(m,n)}{G_x(m,n)} - \frac{G_y(m',n')}{G_x(m',n')}}, \tag{4.9a}$$

$$y_c = n + \frac{G_y(m,n)}{G_x(m,n)}\left(\frac{m' - m + \frac{G_y(m,n)}{G_x(m,n)}m - \frac{G_y(m',n')}{G_x(m',n')}m'}{\frac{G_y(m,n)}{G_x(m,n)} - \frac{G_y(m',n')}{G_x(m',n')}} - m\right). \tag{4.9b}$$

In practice, we find a large set of intersection points $\{(x_c, y_c)\}$ on the detector plane from a large set of mutually orthogonal lines. However, the set $\{(x_c, y_c)\}$ may have

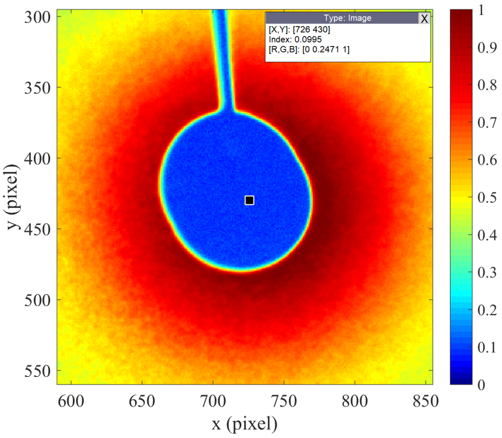

Figure 4.7: The center of diffraction pattern, calculated by the method explained in this section, is shown by a black square.

more than one mode, which means the obtained values for the diffraction pattern are concentrated around more than one point. This happens if, for example, we have a laser leakage point on the detector. For these cases, taking the average of the set will result in an incorrect diffraction center. We rather need to perform a statistical analysis to pick the right center. Low-pass filtering the image also helps to determine the center more precisely, since it reduces the fluctuations in the pixel values due to noise, non-uniformity of the phosphor screen or even the molecular part of the diffraction pattern. The center of diffraction in Figure 4.6a is calculated to be at $(726 \pm 0.3, 430 \pm 0.2)$. Figure 4.7 depicts the center of diffraction.

Once we find the center of diffraction, we can perform the azimuthal averaging. To do so, we define a distance function

$$d(m,n) = \sqrt{(m-x_c)^2 + (n-y_c)^2}, \tag{4.10}$$

which gives the distance between the diffraction center and the the pixel (m,n). Suppose, we have an $N \times N$ pixel image $I(m,n)$. We first flatten the two dimensional matrices d and I into one dimensional arrays:

$$I'((m-1)N+n) = I(n,m); \quad d'((m-1)N+n) = \lfloor d(n,m) \rceil, \tag{4.11}$$

where $\lfloor \bullet \rceil$ indicates rounding to the nearest integer. Ideally, all values in I' that correspond to one specific element value of d' should be the same because they represent all pixels with the same distance from the diffraction center. However, in practice those pixels do not have the same value but have a distribution and we again need to perform a statistical analysis to assign one value to all of those pixels. In appendix B, we have provided a piece of Matlab code that finds the center of diffraction and returns the azimuthal average as well.

After finding the azimuthal average, we use equation (4.4) to find $sM(s)$. The I_{atomic} in the denominator of that equation can be easily obtained from either the tabulated elastic and inelastic scattering amplitudes, or scattering from the Yukawa potential plus the analytic form of the inelastic scattering fit to the measured diffraction pattern. However, $I_{atomic} + I_B$ in the numerator of equation (4.3) should be determined in a much more precise way. Note that the molecular scatting part of the detected signal has a sinusoidal nature and may become zero several times depending on the maximum scattering angle caught by the detector, i.e., the s range.

At zeros of $I_{molecular}$, shown by $\{s_n\}$, the detected signal is equal to $I_{atomic} + I_B$. Therefore, we can fit a curve to the set $\{s_n, I(s_n)\}$ to represent $I_{atomic} + I_B$ in equation (4.4). The zeros of $I_{molecular}$ are obtained from the theory. The other method is to fit a polynomial with variable coefficients to $I_{atomic} + I_B$ such that the difference between $sM(s)$ in the measurement and theory becomes minimum. These methods are the standard techniques in gas phase electron diffraction data analysis [51, 142]. The curve that we fit to the set $\{s_n, I(s_n)\}$ can be either a polynomial of the lowest possible degree [142], or a set of exponential functions. Finally, we low-pass filter the results to cut high frequency noises, which are more prevalent at larger values of s. Figure 4.8 shows the results for azimuthally averaged $sM(s)$. The theoretical results, to which we fit the measurement the best, is given for comparison as well. This procedure revealed that each pixel corresponded to $\Delta s = 0.0125$Å. The two-dimensional diffraction signal in Figure

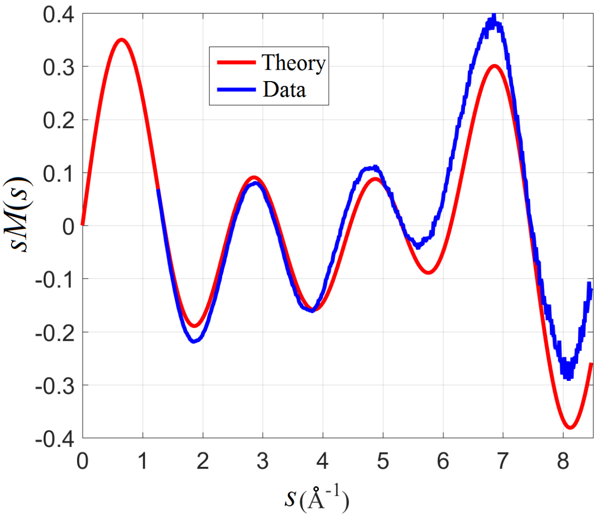

Figure 4.8: Azimuthal average of sM in equation (4.4) from the detected intensity shown in Figure 4.6a. (Structural Dynamics, Vol. 4, 044022, (2017); used in accordance with the Creative Commons Attribution (CC BY) license.)

4.6b is resketched in Figure 4.9 by converting pixels into s . We can take a sine transform of $sM(s)$, to evaluate the inter-atomic distances in CF_3I in real space. As we explained above, we can write $sM(s)$ as a weighted sum of sine functions:

$$sM(s) = \sum_{\alpha\neq\beta} A_{\alpha\beta}\sin(r_{\alpha\beta}s) \tag{4.12}$$

for α and β representing atoms and $A_{\alpha\beta}$ being a constant. Taking a sine transform of $sM(s)$ gives

$$\begin{aligned} f_r(r) = \int_0^\infty ds\, sM(s)\sin(sr) = & \\ &= \int_0^\infty ds \sum_{\alpha\neq\beta} A_{\alpha\beta}\sin(r_{\alpha\beta}s)\sin(sr) \\ &= \sum_{\alpha\neq\beta} A_{\alpha\beta}\int_0^\infty ds\sin(r_{\alpha\beta}s)\sin(sr) \\ &= \frac{\pi}{2}\sum_{\alpha\neq\beta} A_{\alpha\beta}[\delta(r-r_{\alpha\beta})-\delta(r+r_{\alpha\beta})], \end{aligned} \tag{4.13}$$

where $f_r(r)$ represents the radial distribution of atoms. The detector, however,

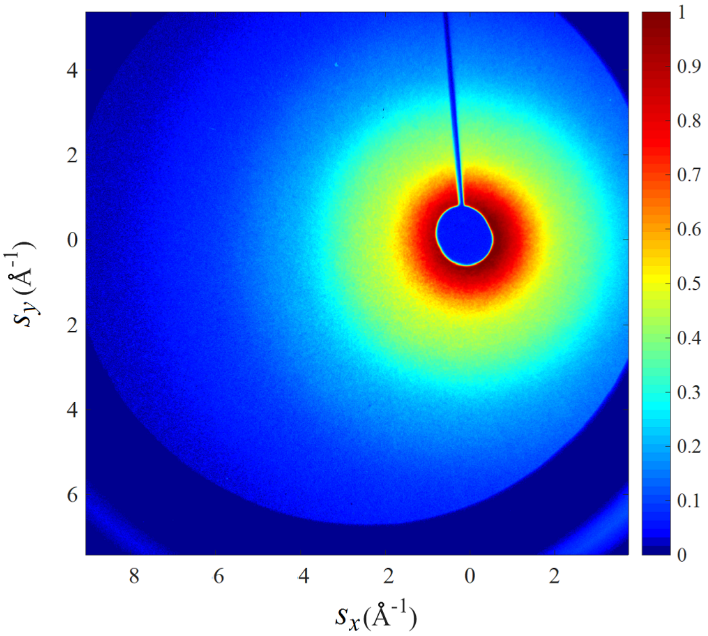

Figure 4.9: Two dimensional diffraction pattern of CF_3I in the momentum space.

has a finite extent s_{max} and equation (4.13) should be revised as

$$f_r(r) = \frac{s_{max}}{2} \sum_{\alpha \neq \beta} A_{\alpha\beta} \{ \mathrm{sinc}[s_{max}(r - r_{\alpha\beta})] - \mathrm{sinc}[s_{max}(r + r_{\alpha\beta})] \}. \tag{4.14}$$

Therefore, there are extra peaks in $f_r(r)$ that are not due to the inter-atomic distances but because of the finite size of the detector. One way of minimizing these artifacts is to use a damping function in the sine transform as

$$f_r(r) = \int_0^\infty ds s M(s) \sin(sr) e^{-\gamma s^2}, \tag{4.15}$$

where γ is a real positive number showing the amount of damping. Figure 4.10 shows the real space reconstruction of the inter-atomic distances of CF_3I by use of the damped sine transform. In this figure, each peak corresponds to one inter-atomic distance where we found $r_{FI} = 2.89$Å, $r_{FF} = 2.15$Å, $r_{CI} = 2.14$Å and $r_{CF} = 1.33$Å. As we mentioned before, the diffraction pattern in this experiment was recorded over 20 s of integration time and the beam current of 70 pA. The results, however, compared favorably with previous UED experiments on CF_3I where the integration time was on the order of one hour due to a much lower

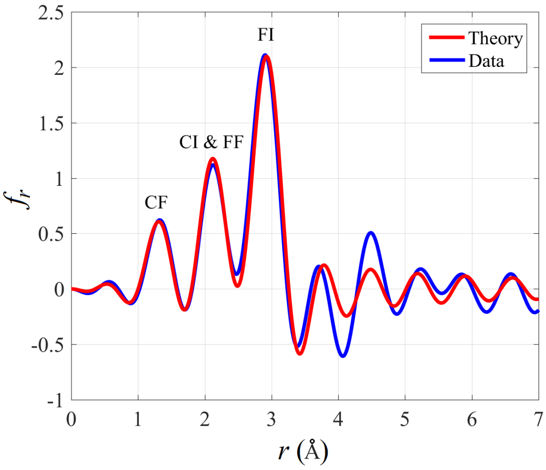

Figure 4.10: Real space reconstruction of CF_3I. (Structural Dynamics, Vol. 4, 044022, (2017); used in accordance with the Creative Commons Attribution (CC BY) license.)

beam current [53]. We repeated the experiment on nitrogen to determine the bond length. Figure 4.11a shows the azimuthally averaged $sM(s)$ for N_2, with a reconstruction in real space shown in figure 4.11b. We retrieved a bond length of 1.093 ± 0.013 Å in agreement with the known value of 1.098 Å. The bond length was retrieved by simulating the sM for different values of the bond length and finding the value that best matched the experimental data. The uncertainty in the bond length is the standard deviation in a set of repeated experiments under the same conditions. The FWHM of the peak in Figure 4.11b is about 0.4 Å. For a molecule with inter-atomic distances which are close, this number determines the resolution by which we can distinguish closely spaced distances. Note that one of the bottlenecks in the gas phase UED experiments was long integration time, on the order of one hour, for a sufficient SNR to retrieve the molecular structure. Previous gas phase UED experiments with keV electrons reached a resolution of 850 fs, with an average beam current of 3 pA [53]. For MeV electrons a resolution of 200 fs have been achieved with a beam current of 0.7 pA. In our setup, we reached a time resolution of 350 fs but with a two orders of magnitude improvement in beam current.

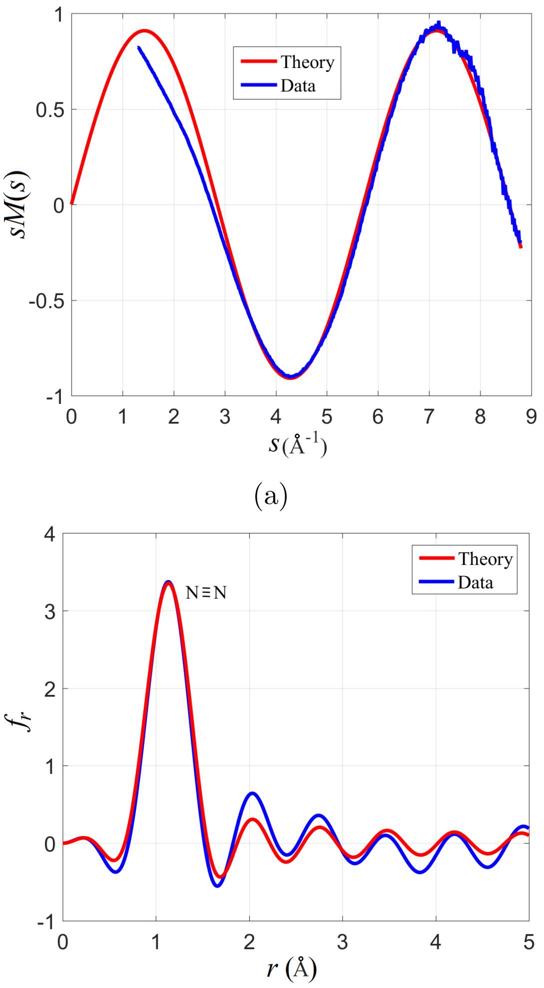

(a)

(b)

Figure 4.11: (a) Experimental and theoretical azimuthaly averaged $sM(s)$ for nitrogen. (b) Real space reconstruction of the bond length. (Structural Dynamics, Vol. 4, 044022, (2017); used in accordance with the Creative Commons Attribution (CC BY) license.)

4.4.2 Gas jet diameter and density measurement

By use of the diffraction signal, we can measure the width and the density of the gas jet. The width of the gas jet was obtained by by moving the nozzle in a perpendicular direction to the electron beam and recording the total pixel counts in the diffraction pattern at each nozzle position. For a more accurate evaluation, we divided the total pixel counts by the average beam current at each point. Table 4.1 shows the recorded data for CF_3I. Figure 4.12 shows a fit Gaussian function to the data points which are proportional to the amplitude of the diffraction signal. The FWHM of the fitted Gaussian is 360 μm. Deconvolving the width of the

Table 4.1: Diffraction signal level with respect to the nozzle position and the beam current.

Total pixel count$\times 10^7$	nozzle position (mm)	Beam current (pA)
1.01	0	55
1.02	0.127	52
1.04	0.254	55
1.08	0.381	56
1.17	0.508	55
1.36	0.635	55
1.59	0.762	55
2.06	0.889	54
2.12	1.016	55
1.50	1.143	57
1.20	1.270	55
1.08	1.397	55
1.04	1.524	55
0.02	1.651	56

electron beam in this experiment ($\sim$300 μm) from this measured width gives a gas jet width of around 220 μm. The backing pressure for CF_3I was 140 Torr in this experiment. We repeated this measurement for nitrogen and found the width of the gas jet to be around 200 μm.

Having the width of the gas jet, we can calculate the density of the gas as well. In the following, we review the steps taken in measuring the gas density:

- We removed the beam block to measure the main electron beam total pixel count. With a gain of 2 and integration time of 0.1 s the total pixel counts was 1.056×10^8 inside a circle with the radius of 81 pixels around the beam center.

- We blocked the main beam and increased the linear gain and the integration time to 10 and 20 s respectively. The diffraction pattern had a total count of 3.251×10^8 between two circles of radii 81 and 430 pixels around the main beam, after subtracting the background signal. Therefore, $\frac{0.1\times 2}{20s\times 10}\frac{3.251\times 10^8}{1.056\times 10^8} \times 100 = 0.31\%$ of the incoming flux was deflected to that area. The mentioned area corresponds to the diffraction angles from 0.0063 to 0.0335 radians.

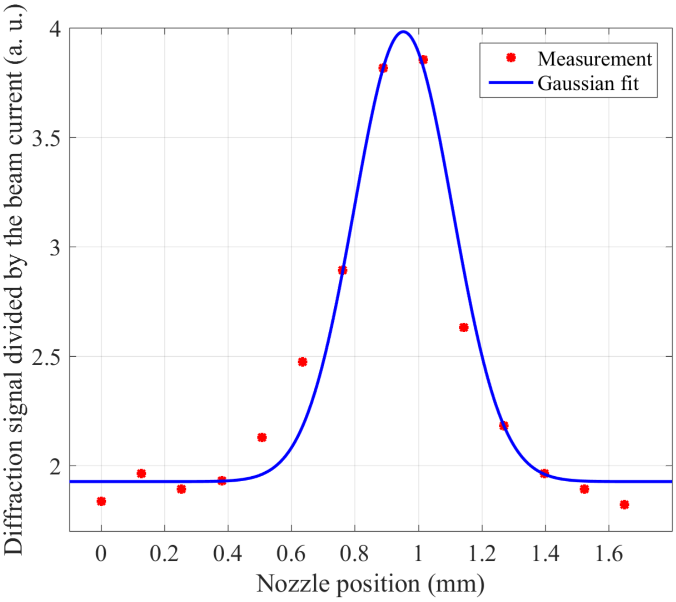

Figure 4.12: Diffraction signal amplitude of CF_3I as a function of the transverse nozzle position.

- If the gas has a width of dz, the incoming flux Φ will decrease according to

$$\frac{d\Phi}{\Phi} = -n\sigma dz, \tag{4.16}$$

where $\frac{d\Phi}{\Phi} = 0.0031$, n is the density of the gas, and σ is the cross section:

$$\sigma(0.0063 < \theta < 0.0335) = \int_{0.0063}^{0.0335} \frac{d\sigma}{d\Omega} d\Omega. \tag{4.17}$$

The function $\frac{d\sigma}{d\Omega} = \left(\frac{0.00233}{0.0218^2+\theta^2}\right)^2$ fits the scattering cross section of atomic nitrogen in units of square of the Bohr radius a_0 best (see Section 1.3.3). Therefore, we get $\sigma = 0.0224a_0^2$, where $a_0 = 5.29 \times 10^{-11}$m.

- By plugging all the values into equation (4.16), we got $n = 2.2 \times 10^{17}\text{cm}^{-3}$. This density should be divided by two since there are two atoms per molecules. It also should be multiplied by the width of the electrons divided by the width of the gas jet. Hence, the gas density is around 1.7×10^{17} molecules/cm^{-3}. Note that in these calculations, we ignored the molecular part of the diffraction signal. The same experiment with CF_3I gave a density of 1.6×10^{16}

molecules/cm^3.

4.5 Temporal and spatial overlapping of pump and probe: time zero

By use of a pinhole in a copper foil mounted under the nozzle, we spatially overlap the electrons, the laser and the gas jet. The foil is adjusted such that the pinhole is accurately under the nozzle. Figure 4.13 illustrates the setup. The copper foil is perpendicular to the laser beam and makes an angle of around 60 degrees with the electron beam. Both the laser and electron beams make it through the pinhole and can be observed by the cameras shown in Figures 2.27 and 4.1, respectively. After centering the two beams on the pinhole, we bring the nozzle down in the path of the both beams. The spatial overlapping can also be done without the pinhole and by use of the nozzle itself, but the pinhole makes it easier and more precise especially for vertical overlapping of the two beams. Furthermore, as we will explain later, the pinhole is used for temporal overlapping of the laser and the electrons.

A coarse temporal overlapping between the electrons and the laser can be achieved by use of the streak camera. As we saw in Figure 3.7, a temporal overlap on the order of 100 ps is attainable. However, we need a temporal overlap within at most few picoseconds. In our setup, we used two techniques to gain an accurate temporal overlapping between the laser and the electron pulses. For the normal intensity front laser beam, we can focus the beam on the gas jet and photo-ionize the gas molecules by which the electron pulses will be affected [50]. For the tilted front laser beam, the laser at its focus has a long pulse duration (see Figure 2.24) and therefore not powerful enough to generate plasma. In this case, we use the copper pinhole. The laser hitting the edge of the pinhole creates a transient space charge field as well as a surface polarization that affect the electron beam [143]. Here, we will discuss these two techniques individually.

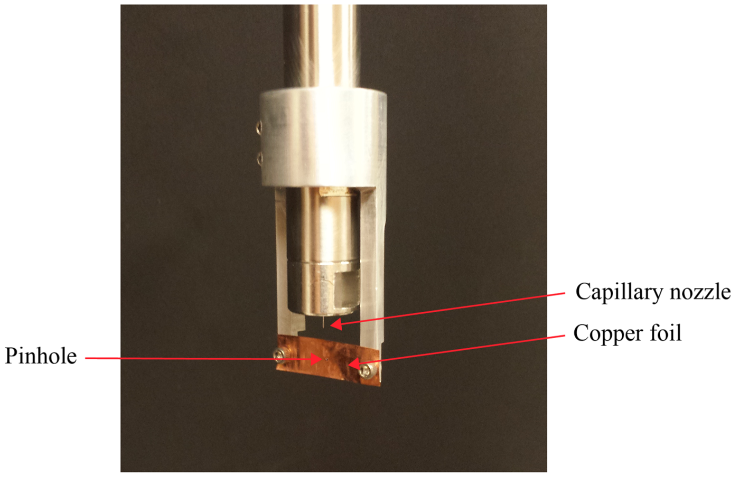

Figure 4.13: Copper foil with a pinhole under the nozzle.

4.5.1 Photo-ionization induced lensing

Figure 4.14 is an image of the target chamber interior taken by a camera at the view port shown in Figure 4.2. The laser with a FWHM diameter of around 10μm was focused onto the gas jet coming out of the nozzle. The laser intensity was around 3×10^{15} W/cm^2 equivalent to the fluence of 240 J/cm^2. The white light created across the laser-gas interaction region can be seen in the figure. At this region, due to the multiphoton ionization a plasma was formed; however, the electrons gained much more kinetic energy than the ions, and were mostly diffused out of the interaction region. Consequently, a cylindrically symmetric charge distribution along the laser path was formed [50]. The resultant electric field was strong enough to disturb the charge distribution in the electron pulse as is demonstrated in Figure 4.15. In this figure, we first delayed the laser pulse with respect to the electrons such that the laser pulse arrived at the target well after the electrons. At this point, we recorded the electron beam on the detector as a reference. We then decreased the delay in constant time steps, and subtracted the reference from any newly recorded image till the disturbance was observed. The temporal evolution can be best seen if we monitor the changes in the pixel counts inside a small portion of the electron beam on the detector as is illustrated

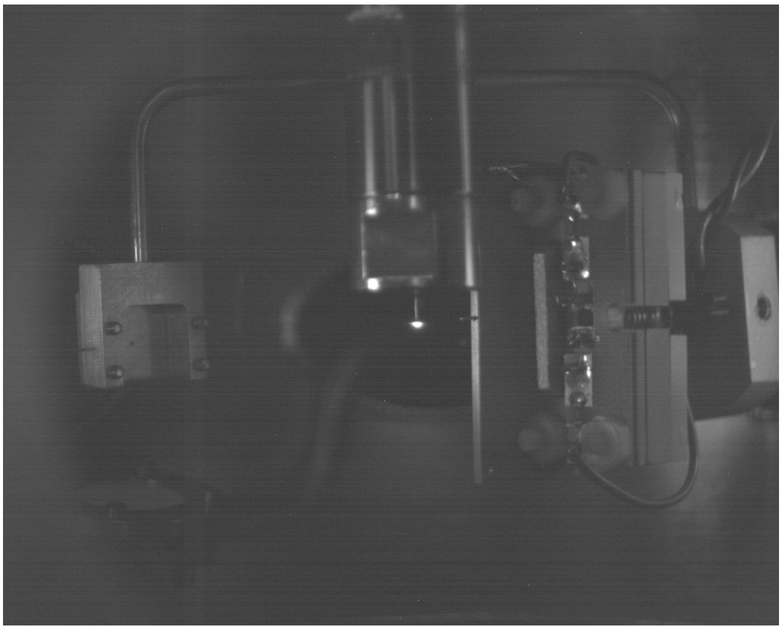

Figure 4.14: The interior of the target chamber. The laser beam is focused onto the gas jet coming out of the nozzle which generates white light.

in Figure 4.16.

We determine the rise time of ionization-induced lensing by fitting the logistic function

$$f(t) = \frac{A}{1 + e^{-\frac{t-t_0}{T}}} \tag{4.18}$$

to the data in Figure 4.16, where $A = 1$, $t_0 = -20.81$ ps, and $T = 0.653$ ps were the fit parameters. The 10% to 90% rise time is equal to $2T\ln(9) = 2.9$ ps.

4.5.2 Transient space charge/polarization field creation

For tilted front laser pulse, the laser passes through the copper pinhole shown in Figure 4.13, with its center slightly lower with respect to the center of the pinhole. By a multiphoton ionization process, some electrons of the metal will be ejected out of the foil [144, 145] and will form a space charge that evolves with time. Also, a temporary surface polarization can be formed as well [146]. Either of these phenomena can affect the electrons with a result shown in Figure 4.17; however, we cannot determine which one has a dominant effect. Similar to the ionization-induced lensing technique, we monitored the change in pixel counts inside a small portion of the detected signal as a function of time with a result

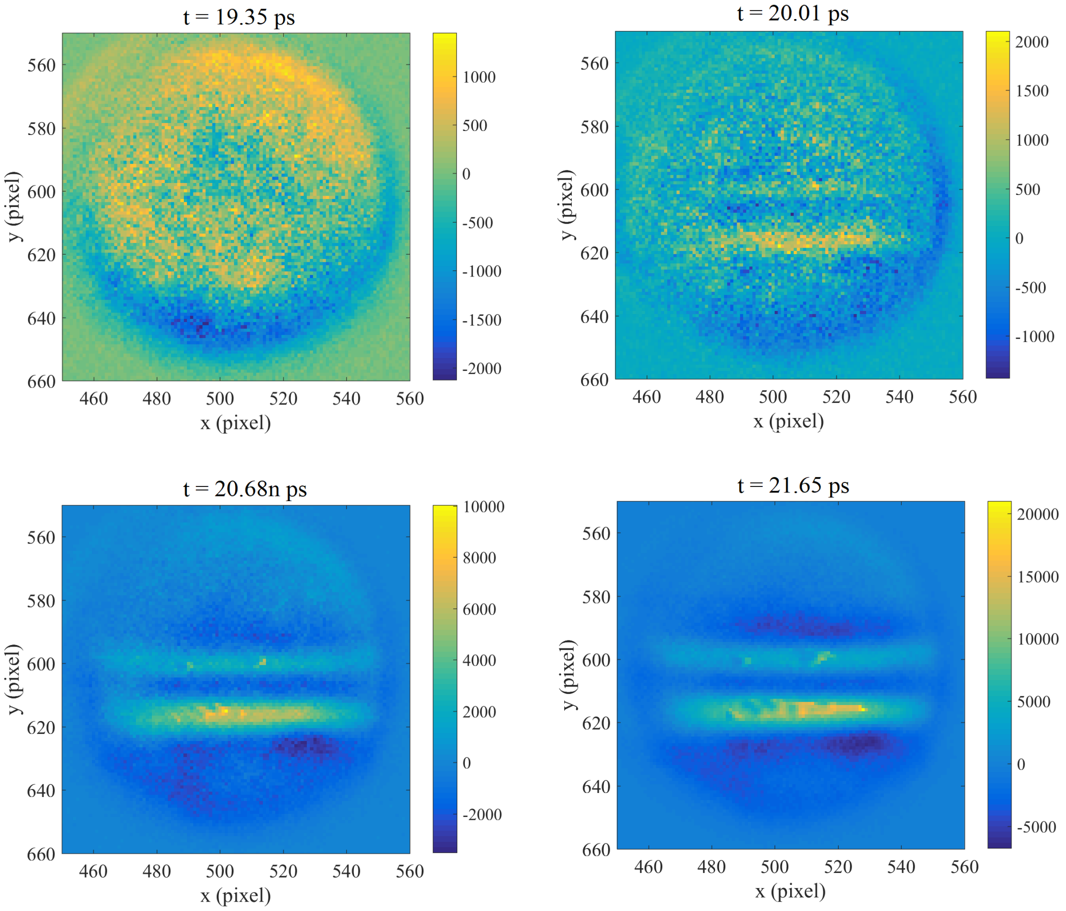

Figure 4.15: The change in the observed electron beam at four different moments caused by the laser multiphoton ionization-induced lensing.

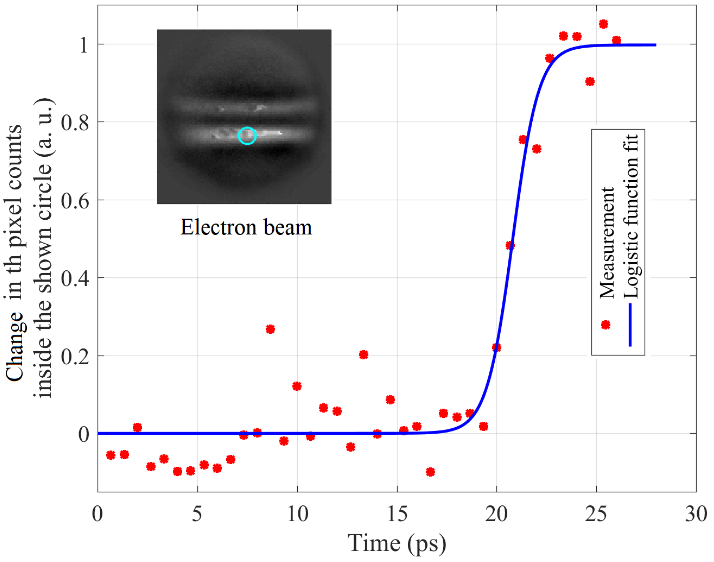

Figure 4.16: The change in the pixel counts in a small circle shown in the electron beam as a function of time. By this figure, the rise time of ionization-induced lensing is determined

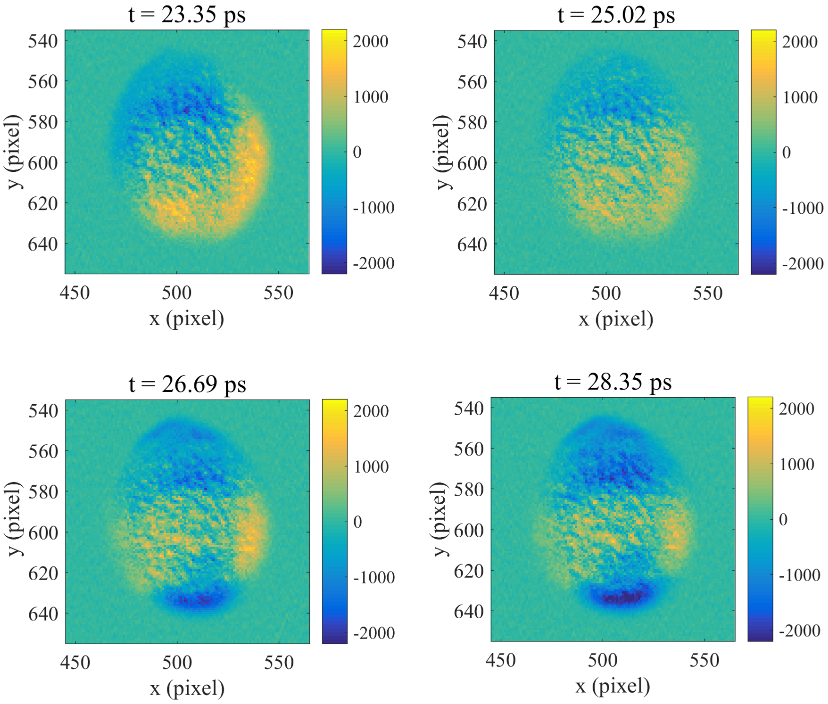

Figure 4.17: The laser hitting the lower edge of the pinhole generates space charge and surface polarization with a time-dependent effect on the electron beam.

shown in Figure 4.18. We determined the 10% to 90% rise time of laser-copper

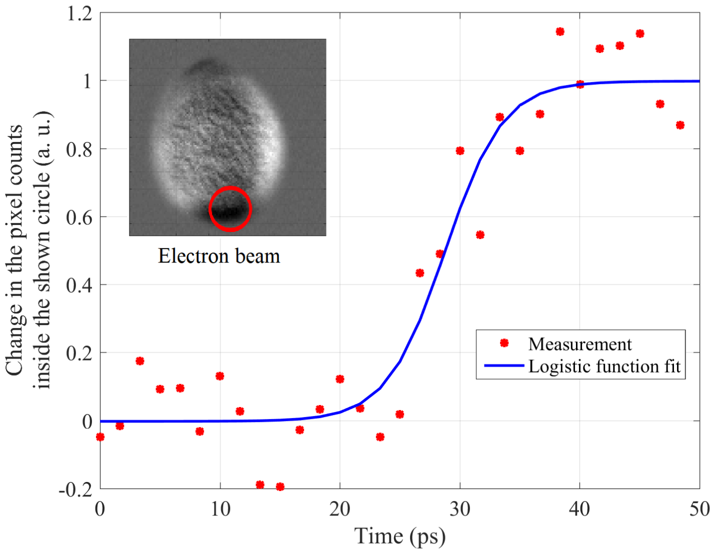

Figure 4.18: The change in the pixel counts in a small circle shown in the electron beam as a function of time. By this figure, the rise time of the laser-copper interaction is obtained.

interaction effect on the electrons by fitting the logistic function in equation (4.18) into the data in Figure 4.18 to be equal to 10.7 ps.

Both of the techniques described here can be used to determine the temporal overlapping of the two beams within at least 2 ps. The lensing technique is, however, more precise since it is possible to employ high intensity laser pulses whilst the same intensity will damage the copper foil. We estimated that the laser intensity is on the order of 10^{10} W/cm^2 on the copper edge.

4.6 Summary

In this chapter, we reviewed the gas injection system and the static diffraction pattern analysis to calibrate the detector. We also provided two methods to synchronize the electron and the laser pulses for both normal and tilted laser intensity fronts.

Chapter 5

Conclusion

This chapter summarizes the structure and the parameters of the apparatus developed in this dissertation. This device delivers electron pulses of femtosecond duration by which ultrafast dynamics induced by femtosecond laser pulses can be observed.

In Chapter 1, we reviewed the quantum theory of high energy electron diffraction from atoms and molecules. We discussed the first Born approximation and its validity in determining the scattering amplitudes from atoms and molecules. Further, a brief history behind the gas phase electron diffraction apparatuses in general, and the time-resolved setups, in particular, mostly from the technology point of view, was included as well.

The elements and the structure of the apparatus was discussed in Chapter 2. In our setup, femtosecond infrared (IR) laser pulses with a maximum power of 10 W and a repetition rate of 5 kHz are used both to generate the electrons and to excite the sample. Around ten percent of the laser output is frequency tripled and used to generate the electron pulses in a one-photon photo-emission process while the rest of the laser power is used to excite the sample. A set of four optical crystals is employed to convert the IR pulses to UV pulses: 1) a BBO crystal generates the second harmonic; 2) a delay plate temporally overlaps the fundamental and the second harmonics; 3) a wave plate matches the polarization of the two harmonics; and 4) a BBO crystal combines the two harmonics to generate an ultraviolet pulse with a wavelength of 267 nm and a photon energy of 4.65 eV. The copper photo-cathode with a work function of 4.7 eV is held at -90 kV with respect to a grounded anode plate in front of it. The electron pulses are accelerated between the cathode and the anode and leave the acceleration stage via a hole in the anode plate. To achieve a stable electron beam, we do not send the UV laser directly to the photo-cathode. We rather truncate the UV beam by a pinhole whose diameter is appreciably smaller than the laser beam diameter and then image the pinhole onto the surface of the cathode. By this technique, at the expense of losing the laser power, fluctuations in the laser beam pointing is compensated, resulting in a stable electron beam. We made a Faraday cup connected to a picoameter to measure the number of electrons per pulse, and showed that electron pulses with millions of electrons were achievable.

Because of the space charge effect, the electron pulses expand in space while traveling from the photo-cathode to the target. As a result, the temporal resolution of the setup decreases. In our setup, we use three magnetic lenses and one radio-frequency (RF) cavity to compress the electron pulses transversely and longitudinally (in time), respectively. It is worth noting that the photo-emission method, by which we generate the electron pulses, results in pulses that are uniformly charged spheroids. An important property of such pulses is that they maintain their profile, i.e. they stay uniformly charged spheroids, although their dimension increases and their charge density decreases because of the space charge effect. The reason is that the Coulomb force inside such a pulse is linear in space at each time. We take advantage of this property to apply a linear force to reverse the electron pulse expansion and compress it at the position of the target. In the longitudinal direction, the electrons move with velocity close to the half of the light speed in vacuum. The time-varying longitudinal electric field of the RF cavity is responsible to apply the linear force to temporally compress the electron pulses. Once the electron pulse enters the RF cavity region, there is force pushing the electrons in its front to its center and the force decreases as the electrons enter the RF cavity further and becomes zero once the center of the pulse enters the field region. Then, the force switches its direction to push the electrons in the back side of the pulse toward its center. Obviously, a proper timing between the RF field and arrival time of the electrons is essential to obtain shortest pulse duration. We achieve an accurate timing by synchronizing the RF field to the laser oscillator by use of a commercial synchronizer.

We built a streak camera that evaluates the performance of the RF compression by measuring the electron pulse duration at the position of the target and it was the topic of Chapter 3. The streak camera is composed of a charged parallel plate capacitor connected in parallel to a GaAs photo-switch. A laser pulse activates the switch and causes a damped harmonic oscillation in the electric field across the capacitor. The electron pulse going through the plates of the capacitor is affected by the time-varying electric field. We send the laser to the photo-switch such that the electrons traverse the capacitor when its electric field is changing sign (crossing zero) for the first time, where the rate of the change in the electric field is maximum. This field deflects the electrons in the back and front parts of the pulse oppositely streaking the electron pulse on the detector. We developed a mathematical method to extract the pulse duration from the streaked patterns of the electrons. With a resolution better than 100 fs, we measured an electron pulse duration as low as 350 fs. The streak camera can also monitor the slow jitters (drifts) in the arrival time of electrons within 70 fs. The major obstacle in achieving a shorter electron pulse duration is the jitter in the timing between the arrival of the electrons and the radio-frequency field. This problem is more severe in gas phase experiments since the data is gathered over many shots, in contrast to the condensed samples, where single shot experiments are feasible.

One other parameter that can severely deteriorates the setup temporal resolution, and was discussed in detail in Chapter 2, is the velocity mismatch between the exciting laser (the pump) and the electrons (the probe). The laser and the electron pulses do not travel with the same velocities; therefore, the target will not be excited and probed at the same time. This will blur the observed signal. We solved this problem by using the laser front tilting technique. The laser was sent to the target with an angle around 60 degrees with respect to the electrons such that its velocity components in the direction of electrons matches the velocity of electrons. We tilted the intensity front of laser pulses by use of an optical grating to match the velocity of the laser pulse to that of the electrons.

As we have explained in Chapter 4, we conducted a diffraction experiment on CF_3I to calibrate the setup detector in the momentum space. We verified the calibration by a diffraction experiment on N_2 that determined its bond length. The beam current was around 70 pA and the experiments were done over 20 s of integration time which is appreciably shorter in comparison with similar setups that do not use electron compression and hence have much lower beam current. We also performed two experiments to determine the temporal overlapping between the laser and the electron pulses. For a laser beam with a normal intensity front, we focused the beam on the gas jet to increase the light intensity and ionize the gas molecules. This process forms a plasma under the nozzle; however, the electrons gain more kinetic energy and leave the area resulting in a cylindrical channel of positive ions that affects the electron beam. For the tilted intensity front laser beam, we cannot focus the beam on the gas jet for the same purpose since the laser pulse duration would be too long at the focus and the laser is not powerful enough to create a plasma. We rather mounted a copper pinhole under the nozzle through which the laser and the electron pulses go. The laser, either by a multiphoton ionization and space charge creation or by a surface induced polarization in the copper, will affect the electrons. Both of these effects have a short rise time which help to determine the temporal overlap within at most two picoseconds.

References

[1] Louis De Broglie. *Recherches sur la théorie des quanta.* PhD thesis, Migration-université en cours d'affectation, 1924.

[2] Richard P Feynman, Albert R Hibbs, and Daniel F Styer. *Quantum mechanics and path integrals.* Courier Corporation, 2010.

[3] J David Jackson. *Electrodynamics.* Wiley Online Library, 1975.

[4] Ta-You Wu and Takashi Ohmura. *Quantum theory of scattering.* Prentice-Hall Inc., 1962.

[5] Roger G Newton. *Scattering theory of waves and particles.* Springer Science & Business Media, 2013.

[6] John R Taylor. *Scattering theory: the quantum theory of nonrelativistic collisions.* Courier Corporation, 2006.

[7] A Jablonski, F Salvat, and CJ Powell. *NIST electron elastic-scattering cross-section database.* National Institute of Standards and Technology, Gaithersburg, MD, 2010.

[8] C Colliex, JM Cowley, SL Dudarev, M Fink, J Gjønnes, R Hilderbrandt, A Howie, DF Lynch, LM Peng, G Ren, et al. Electron diffraction. In *International Tables for Crystallography Volume C: Mathematical, physical and chemical tables*, pages 259–429. Springer, 2006.

[9] Roy Glauber and Verner Schomaker. The theory of electron diffraction. *Physical Review*, 89(4):667, 1953.

[10] HSW Massey and CBO Mohr. The collision of electrons with molecules. *Proceedings of the Royal Society of London. Series A, Containing Papers of a Mathematical and Physical Character*, 135(826):258–275, 1932.

[11] David B Williams and C Barry Carter. The transmission electron microscope. In *Transmission electron microscopy*, page 54. Springer, 1996.

[12] Hua-Chieh Shao and Anthony F Starace. Detecting electron motion in atoms and molecules. *Physical review letters*, 105(26):263201, 2010.

[13] Hua-Chieh Shao and Anthony F Starace. Imaging coherent electronic motion in atoms by ultrafast electron diffraction. *Physical Review A*, 88(6): 062711, 2013.

[14] S Bratos, F Mirloup, R Vuilleumier, and M Wulff. Time-resolved x-ray diffraction: Statistical theory and its application to the photo-physics of molecular iodine. *The Journal of chemical physics*, 116(24):10615–10625, 2002.

[15] Jens Als-Nielsen and Des McMorrow. *Elements of modern X-ray physics*. John Wiley & Sons, 2011.

[16] Gopal Dixit, Oriol Vendrell, and Robin Santra. Imaging electronic quantum motion with light. *Proceedings of the National Academy of Sciences*, 109(29):11636–11640, 2012.

[17] Kochise Bennett, Jason D Biggs, Yu Zhang, Konstantin E Dorfman, and Shaul Mukamel. Time-, frequency-, and wavevector-resolved x-ray diffraction from single molecules. *The Journal of chemical physics*, 140(20): 204311, 2014.

[18] Adam Kirrander, Kenichiro Saita, and Dmitrii V Shalashilin. Ultrafast x-ray scattering from molecules. *Journal of chemical theory and computation*, 12(3):957–967, 2016.

[19] Minas Stefanou, Kenichiro Saita, Dmitrii V Shalashilin, and Adam Kirrander. Comparison of ultrafast electron and x-ray diffraction–a computational study. *Chemical Physics Letters*, 2017.

[20] CG Shull and EO Wollan. X-ray, electron, and neutron disraction. *Science*, 108:70, 1948.

[21] Paul Emma, R Akre, J Arthur, R Bionta, C Bostedt, J Bozek, A Brachmann, P Bucksbaum, Ryan Coffee, F-J Decker, et al. First lasing and operation of an ångstrom-wavelength free-electron laser. *nature photonics*, 4(9):641–647, 2010.

[22] Jochen Küpper, Stephan Stern, Lotte Holmegaard, Frank Filsinger, Arnaud Rouzée, Artem Rudenko, Per Johnsson, Andrew V Martin, Marcus Adolph, Andrew Aquila, et al. X-ray diffraction from isolated and strongly aligned gas-phase molecules with a free-electron laser. *Physical Review Letters*, 112(8):083002, 2014.

[23] JM Glownia, A Natan, JP Cryan, R Hartsock, M Kozina, MP Minitti, S Nelson, J Robinson, T Sato, T van Driel, et al. Self-referenced coherent diffraction x-ray movie of ångstrom-and femtosecond-scale atomic motion. *Physical review letters*, 117(15):153003, 2016.

[24] SM Bennington. The use of neutron scattering in the study of ceramics. *Journal of materials science*, 39(22):6757–6779, 2004.

[25] Herman Mark and Raimund Wierl. Die ermittlung von molekülstrukturen durch beugung von elektronen an einem dampfstrahl. *Berichte der Bunsengesellschaft für physikalische Chemie*, 36(9):675–676, 1930.

[26] Ro Wierl. Elektronenbeugung und molekülbau. *Annalen der Physik*, 400 (5):521–564, 1931.

[27] Lawrence O Brockway and Linus Pauling. The electron-diffraction investigation of the structure of molecules of methyl azide and carbon suboxide. *Proceedings of the National Academy of Sciences*, 19(9):860–867, 1933.

[28] Ralph W Dornte. Electron diffraction and molecular structure: Carbonyl compounds1. *Journal of the American Chemical Society*, 55(10): 4126–4130, 1933.

[29] LO Brockway and Linus Pauling. The determination of the structures of the hexafluorides of sulfur, selenium and tellurium by the electron diffraction method. *Proceedings of the National Academy of Sciences*, 19 (1):68–73, 1933.

[30] St B Hendricks, Louis R Maxwell, VL Mosley, and ME Jefferson. X-ray and electron diffraction of iodine and the diiodobenzenes. *The Journal of Chemical Physics*, 1(8):549–565, 1933.

[31] Ralph W Dornte. The determination of the structures of methane derivatives by the electron diffraction method. *The Journal of Chemical Physics*, 1(9):630–633, 1933.

[32] FL Arnot. The diffraction of electrons in the halogens. *Proceedings of the Royal Society of London. Series A, Containing Papers of a Mathematical and Physical Character*, 144(852):360–377, 1934.

[33] Linus Pauling and LO Brockway. A study of the methods of interpretation of electron-diffraction photographs of gas molecules, with results for benzene and carbon tetrachloride. *The Journal of Chemical Physics*, 2(12): 867–881, 1934.

[34] Louis R Maxwell, VM Mosley, and Lola S Deming. Electron diffraction by the oxides of nitrogen. *The Journal of Chemical Physics*, 2(6):331–336, 1934.

[35] LR Maxwell, SB Hendricks, and VM Mosley. Electron diffraction by gases. *The Journal of Chemical Physics*, 3(11):699–709, 1935.

[36] Lawrence O Brockway. Electron diffraction by gas molecules. *Reviews of Modern Physics*, 8(3):231, 1936.

[37] Philip G Ackermann and Joseph E Mayer. Determination of molecular structure by electron diffraction. *The Journal of Chemical Physics*, 4(6): 377–381, 1936.

[38] LO Brockway. The electron diffraction investigation of the fluorochloromethanes. *Journal of Physical Chemistry*, 41(5):747–762, 1937.

[39] LR Maxwell, SB Hendricks, and VM Mosley. Interatomic distances of the alkali halide molecules by electron diffraction. *Physical Review*, 52(9):968, 1937.

[40] István Hargittai and Magdolna Hargittai. *Stereochemical applications of gas-phase electron diffraction*. VCH, 1988.

[41] FL Arnot. The passage of an electron beam through a field-free enclosure. *Proceedings of the Royal Society of London. Series A, Containing Papers of a Mathematical and Physical Character*, 129(810):361–377, 1930.

[42] Peter Goodman. *Fifty years of electron diffraction: in recognition of fifty years of achievement by the crystallographers and gas diffractionists in the field of electron diffraction*. D Reidel Pub Co, 1981.

[43] FL Arnot. The diffraction of electrons in gases. *Proceedings of the Royal Society of London. Series A, Containing Papers of a Mathematical and Physical Character*, 133(822):615–636, 1931.

[44] P Andersen. An electron diffraction investigation of free radical triphenylmethyl in gas phase. *ACTA CHEMICA SCANDINAVICA*, 19(3): 629, 1965.

[45] Birgit Andersen and Per Andersen. An electron diffraction investigation of the di-t-butylnitroxide free radical. *Transactions of the American Crystallographic Association*, 2:193, 1966.

[46] Robert K Bohn and Simon Harvey Bauer. An electron diffraction study of the structures of nf2 and n2f4. *Inorganic Chemistry*, 6(2):304–309, 1967.

[47] Anthony P Rood and Judith Milledge. Combined flash-photolysis and gas-phase electron-diffraction studies of small molecules. *Journal of the Chemical Society, Faraday Transactions 2: Molecular and Chemical Physics*, 80(9):1145–1153, 1984.

[48] AA Ischenko, VV Golubkov, VP Spiridonov, AV Zgurskii, AS Akhmanov, MG Vabischevich, and VN Bagratashvili. A stroboscopical gas-electron diffraction method for the investigation of short-lived molecular species. *Applied Physics B: Lasers and Optics*, 32(3):161–163, 1983.

[49] JC Williamson, M Dantus, SB Kim, and AH Zewail. Ultrafast diffraction and molecular structure. *Chemical Physics Letters*, 196(6):529–534, 1992.

[50] Marcos Dantus, Scott B Kim, J Charles Williamson, and Ahmed H Zewail. Ultrafast electron diffraction. 5. experimental time resolution and applications. *The Journal of Physical Chemistry*, 98(11):2782–2796, 1994.

[51] Ramesh Srinivasan, Vladimir A Lobastov, Chong-Yu Ruan, and Ahmed H Zewail. Ultrafast electron diffraction (ued). *Helvetica Chimica Acta*, 86(6): 1761–1799, 2003.

[52] J Charles Williamson, Jianming Cao, Hyotcherl Ihee, Hans Frey, and Ahmed H Zewail. Clocking transient chemical changes by ultrafast electron diffraction. *Nature*, 386(6621):159, 1997.

[53] Christopher J Hensley, Jie Yang, and Martin Centurion. Imaging of isolated molecules with ultrafast electron pulses. *Physical review letters*, 109(13):133202, 2012.

[54] Matthew S Robinson, Paul D Lane, and Derek A Wann. A compact electron gun for time-resolved electron diffraction. *Review of Scientific Instruments*, 86(1):013109, 2015.

[55] Wayne E King, Geoffrey H Campbell, Alan Frank, Bryan Reed, John F Schmerge, Bradley J Siwick, Brent C Stuart, and Peter M Weber. Ultrafast electron microscopy in materials science, biology, and chemistry. *Journal of Applied Physics*, 97(11):8, 2005.

[56] JB Hastings, FM Rudakov, DH Dowell, JF Schmerge, JD Cardoza, JM Castro, SM Gierman, H Loos, and PM Weber. Ultrafast time-resolved electron diffraction with megavolt electron beams. *Applied physics letters*, 89(18):184109, 2006.

[57] P Musumeci, JT Moody, CM Scoby, MS Gutierrez, HA Bender, and NS Wilcox. High quality single shot diffraction patterns using ultrashort megaelectron volt electron beams from a radio frequency photoinjector. *Review of Scientific Instruments*, 81(1):013306, 2010.

[58] Jie Yang, Markus Guehr, Theodore Vecchione, Matthew S Robinson, Renkai Li, Nick Hartmann, Xiaozhe Shen, Ryan Coffee, Jeff Corbett, Alan Fry, et al. Diffractive imaging of a rotational wavepacket in nitrogen molecules with femtosecond megaelectronvolt electron pulses. *Nature communications*, 7:11232, 2016.

[59] T Van Oudheusden, EF De Jong, SB Van der Geer, WPEM Op t Root, OJ Luiten, and BJ Siwick. Electron source concept for single-shot sub-100 fs electron diffraction in the 100 kev range. *Journal of Applied Physics*, 102 (9):093501, 2007.

[60] Peter Baum and Ahmed Zewail. Femtosecond diffraction with chirped electron pulses. *Chemical Physics Letters*, 462(1):14–17, 2008.

[61] Yihua Wang and Nuh Gedik. Electron pulse compression with a practical reflectron design for ultrafast electron diffraction. *IEEE Journal of selected topics in quantum electronics*, 18(1):140–147, 2012.

[62] T Van Oudheusden, PLEM Pasmans, SB Van Der Geer, MJ De Loos, MJ Van Der Wiel, and OJ Luiten. Compression of subrelativistic space-charge-dominated electron bunches for single-shot femtosecond electron diffraction. *Physical review letters*, 105(26):264801, 2010.

[63] Robert P Chatelain, Vance R Morrison, Chris Godbout, and Bradley J Siwick. Ultrafast electron diffraction with radio-frequency compressed electron pulses. *Applied Physics Letters*, 101(8):081901, 2012.

[64] GH Kassier, N Erasmus, K Haupt, I Boshoff, R Siegmund, SMM Coelho, and H Schwoerer. Photo-triggered pulsed cavity compressor for bright electron bunches in ultrafast electron diffraction. *Applied Physics B*, 109 (2):249–257, 2012.

[65] Meng Gao, Cheng Lu, Hubert Jean-Ruel, Lai Chung Liu, Alexander Marx, Ken Onda, Shin-ya Koshihara, Yoshiaki Nakano, Xiangfeng Shao, Takaaki Hiramatsu, et al. Mapping molecular motions leading to charge delocalization with ultrabright electrons. *Nature*, 496(7445):343, 2013.

[66] Omid Zandi, Kyle J Wilkin, Yanwei Xiong, and Martin Centurion. High current table-top setup for femtosecond gas electron diffraction. *Structural Dynamics*, 4(4):044022, 2017.

[67] J Charles Williamson and Ahmed H Zewail. Ultrafast electron diffraction. velocity mismatch and temporal resolution in crossed-beam experiments. *Chemical physics letters*, 209(1-2):10–16, 1993.

[68] Peter Baum and Ahmed H Zewail. Breaking resolution limits in ultrafast electron diffraction and microscopy. *Proceedings of the National Academy of Sciences*, 103(44):16105–16110, 2006.

[69] Ping Zhang, Jie Yang, and Martin Centurion. Tilted femtosecond pulses for velocity matching in gas-phase ultrafast electron diffraction. *New Journal of Physics*, 16(8):083008, 2014.

[70] SP Weathersby, G Brown, Martin Centurion, TF Chase, Ryan Coffee, Jeff Corbett, JP Eichner, JC Frisch, AR Fry, M Gühr, et al. Mega-electron-volt ultrafast electron diffraction at slac national accelerator laboratory. *Review of Scientific Instruments*, 86(7):073702, 2015.

[71] Jie Yang, Markus Guehr, Theodore Vecchione, Matthew S Robinson, Renkai Li, Nick Hartmann, Xiaozhe Shen, Ryan Coffee, Jeff Corbett, Alan Fry, et al. Femtosecond gas phase electron diffraction with mev electrons. *Faraday discussions*, 194:563–581, 2016.

[72] Jie Yang, Markus Guehr, Xiaozhe Shen, Renkai Li, Theodore Vecchione, Ryan Coffee, Jeff Corbett, Alan Fry, Nick Hartmann, Carsten Hast, et al. Diffractive imaging of coherent nuclear motion in isolated molecules. *Physical review letters*, 117(15):153002, 2016.

[73] Jie Yang, Joshua Beck, Cornelis J Uiterwaal, and Martin Centurion. Imaging of alignment and structural changes of carbon disulfide molecules using ultrafast electron diffraction. *Nature communications*, 6:8172, 2015.

[74] Germán Sciaini and RJ Dwayne Miller. Femtosecond electron diffraction: heralding the era of atomically resolved dynamics. *Reports on Progress in Physics*, 74(9):096101, 2011.

[75] Giulia Fulvia Mancini, Barbara Mansart, Saverio Pagano, Bas Van Der Geer, Marieke De Loos, and Fabrizio Carbone. Design and implementation of a flexible beamline for fs electron diffraction

experiments. *Nuclear Instruments and Methods in Physics Research Section A: Accelerators, Spectrometers, Detectors and Associated Equipment*, 691:113–122, 2012.

[76] Vance R Morrison, Robert P Chatelain, Kunal L Tiwari, Ali Hendaoui, Andrew Bruhács, Mohamed Chaker, and Bradley J Siwick. A photoinduced metal-like phase of monoclinic vo2 revealed by ultrafast electron diffraction. *Science*, 346(6208):445–448, 2014.

[77] Robert P Chatelain, Vance R Morrison, Bart LM Klarenaar, and Bradley J Siwick. Coherent and incoherent electron-phonon coupling in graphite observed with radio-frequency compressed ultrafast electron diffraction. *Physical review letters*, 113(23):235502, 2014.

[78] Thijs van Oudheusden. *Electron source for sub-relativistic single-shot femtosecond diffraction.* PhD thesis, Ph. D. thesis, Technische Universiteit Eindhoven, 2010.

[79] Omid Zandi, Kyle J Wilkin, Alice J DeSimone, Jie Yang, and Martin Centurion. Femtosecond electron pulse generation and measurement for diffractive imaging of isolated molecules. In *SPIE Optical Engineering+ Applications*, pages 995602–995602. International Society for Optics and Photonics, 2016.

[80] OJ Luiten, SB Van der Geer, MJ De Loos, FB Kiewiet, and MJ Van Der Wiel. How to realize uniform three-dimensional ellipsoidal electron bunches. *Physical review letters*, 93(9):094802, 2004.

[81] Lev Davidovich Landau. *The classical theory of fields*, volume 2. Elsevier, 2013.

[82] M Grech, R Nuter, A Mikaberidze, P Di Cintio, L Gremillet, E Lefebvre, U Saalmann, JM Rost, and S Skupin. Coulomb explosion of uniformly charged spheroids. *Physical Review E*, 84(5):056404, 2011.

[83] Jie Yang, Omid Zandi, Ping Zhang, and Martin Centurion. Imaging of molecules in the gas phase with ultrafast electron diffraction. In *SPIE Optical Engineering+ Applications*, pages 91980N–91980N. International Society for Optics and Photonics, 2014.

[84] Stanley Humphries. *Principles of charged particle acceleration.* Courier Corporation, 2013.

[85] Peter A Rizzi. *Microwave engineering: passive circuits.* Prentice Hall, 1988.

[86] PLEM Pasmans, GB van den Ham, SFP Dal Conte, SB van der Geer, and OJ Luiten. Microwave tm 010 cavities as versatile 4d electron optical elements. *Ultramicroscopy*, 127:19–24, 2013.

[87] FB Kiewiet, AH Kemper, OJ Luiten, GJH Brussaard, and MJ van der Wiel. Femtosecond synchronization of a 3ghz rf oscillator to a mode-locked ti: sapphire laser. *Nuclear Instruments and Methods in Physics Research*

Section A: Accelerators, Spectrometers, Detectors and Associated Equipment, 484(1):619–624, 2002.

[88] SB Van der Geer, MJ de Loos, EJD Vredenbregt, and OJ Luiten. Ultracold electron source for single-shot, ultrafast electron diffraction. *Microscopy and Microanalysis*, 15(4):282–289, 2009.

[89] Francesco Pennacchio, Giovanni M Vanacore, Giulia F Mancini, Malte Oppermann, Rajeswari Jayaraman, Pietro Musumeci, Peter Baum, and Fabrizio Carbone. Design and implementation of an optimal laser pulse front tilting scheme for ultrafast electron diffraction in reflection geometry with high temporal resolution. *Structural Dynamics*, 4(4):044032, 2017.

[90] Oscar Eduardo Martinez. Pulse distortions in tilted pulse schemes for ultrashort pulses. *Optics communications*, 59(3):229–232, 1986.

[91] Daniel Kreier and Peter Baum. Avoiding temporal distortions in tilted pulses. *Optics letters*, 37(12):2373–2375, 2012.

[92] A Skinner. Versatile high speed rotating mirror cameras. *Journal of Scientific Instruments*, 39(7):336, 1962.

[93] Alexander Horn. *Ultra-fast material metrology*. John Wiley & Sons, 2009.

[94] DJ Bradley, B Liddy, and WE Sleat. Direct linear measurement of ultrashort light pulses with a picosecond streak camera. *Optics Communications*, 2(8):391–395, 1971.

[95] DJ Bradley and GEOFFREY HC New. Ultrashort pulse measurements. *Proceedings of the IEEE*, 62(3):313–345, 1974.

[96] G Mourou and W Knox. A picosecond jitter streak camera. *Applied Physics Letters*, 36(8):623–626, 1980.

[97] Wayne Knox and Gerard Mourou. A simple jitter-free picosecond streak camera. *Optics Communications*, 37(3):203–206, 1981.

[98] V Guidi and AV Novokhatsky. A proposal for a radio-frequency-based streak camera with time resolution less than 100 fs. *Measurement Science and Technology*, 6(11):1555, 1995.

[99] Z Chang, A Rundquist, J Zhou, MM Murnane, HC Kapteyn, X Liu, B Shan, J Liu, L Niu, M Gong, et al. Demonstration of a sub-picosecond x-ray streak camera. *Applied physics letters*, 69(1):133–135, 1996.

[100] Anatoly Maksimchuk, M Kim, J Workman, G Korn, J Squier, D Du, Donald Umstadter, G Mourou, and M Bouvier. Signal averaging x-ray streak camera with picosecond jitter. *Review of scientific instruments*, 67 (3):697–699, 1996.

[101] J Larsson, Z Chang, E Judd, PJ Schuck, RW Falcone, PA Heimann, HA Padmore, HC Kapteyn, PH Bucksbaum, MM Murnane, et al. Ultrafast x-ray diffraction using a streak-camera detector in averaging mode. *Optics letters*, 22(13):1012–1014, 1997.

[102] DX Wang, GA Krafft, and CK Sinclair. Measurement of femtosecond electron bunches using a rf zero-phasing method. *Physical Review E*, 57(2): 2283, 1998.

[103] AV Aleksandrov, NS Dikansky, V Guidi, GV Lamanna, PV Logatchov, SV Shiyankov, and L Tecchio. Setting up and time-resolution measurement of a radio-frequency-based streak camera. *Review of scientific instruments*, 70(6):2622–2626, 1999.

[104] C Belzile, JC Kieffer, CY Cote, T Oksenhendler, and D Kaplan. Jitter-free subpicosecond streak cameras. *Review of scientific instruments*, 73(3): 1617–1620, 2002.

[105] Jinyuan Liu, Jin Wang, Bing Shan, Chun Wang, and Zenghu Chang. An accumulative x-ray streak camera with sub-600-fs temporal resolution and 50-fs timing jitter. *Applied physics letters*, 82(20):3553–3555, 2003.

[106] Mahendra Man Shakya and Zenghu Chang. An accumulative x-ray streak camera with 280-fs resolution. In *Proceedings of SPIE*, volume 5534, page 125, 2004.

[107] Chi H Lee. Picosecond optoelectronic switching in gaas. *Applied Physics Letters*, 30(2):84–86, 1977.

[108] T van Oudheusden, JR Nohlmans, WSC Roelofs, WPEM Opt Root, and OJ Luiten. 3 ghz rf streak camera for diagnosis of sub-100 fs, 100 kev electron bunches. In *Ultrafast Phenomena XVI*, pages 938–940. Springer, 2009.

[109] Christoph T Hebeisen, Ralph Ernstorfer, Maher Harb, Thibault Dartigalongue, Robert E Jordan, and RJ Dwayne Miller. Femtosecond electron pulse characterization using laser ponderomotive scattering. *Optics letters*, 31(23):3517–3519, 2006.

[110] Christoph T Hebeisen, German Sciaini, Maher Harb, Ralph Ernstorfer, Thibault Dartigalongue, Sergei G Kruglik, and RJ Dwayne Miller. Grating enhanced ponderomotive scattering for visualization and full characterization of femtosecond electron pulses. *Optics express*, 16(5): 3334–3341, 2008.

[111] Meng Gao, Hubert Jean-Ruel, Ryan R Cooney, Jonathan Stampe, Mark de Jong, Maher Harb, German Sciaini, Gustavo Moriena, and RJ Dwayne Miller. Full characterization of rf compressed femtosecond electron pulses using ponderomotive scattering. *Optics express*, 20(11):12048–12058, 2012.

[112] Gunther Horst Kassier, K Haupt, N Erasmus, EG Rohwer, HM Von Bergmann, H Schwoerer, Sergio MM Coelho, and Francois Danie Auret. A compact streak camera for 150 fs time resolved measurement of bright pulses in ultrafast electron diffraction. *Review of Scientific Instruments*, 81(10):105103, 2010.

[113] Meng Gao, Yifeng Jiang, Gunther H Kassier, and RJ Dwayne Miller. Single shot time stamping of ultrabright radio frequency compressed electron pulses. *Applied Physics Letters*, 103(3):033503, 2013.

[114] O Zandi, KJ Wilkin, and M Centurion. Implementation and modeling of a femtosecond laser-activated streak camera. *Review of Scientific Instruments*, 88(6):063305, 2017.

[115] Justyna Fabiańska, Günther Kassier, and Thomas Feurer. Split ring resonator based thz-driven electron streak camera featuring femtosecond resolution. *Scientific reports*, 4, 2014.

[116] C Kealhofer, Waldemar Schneider, Dominik Ehberger, A Ryabov, Ferenc Krausz, and Peter Baum. All-optical control and metrology of electron pulses. *Science*, 352(6284):429–433, 2016.

[117] Chi H Lee. *Picosecond optoelectronic devices*. Elsevier, 2012.

[118] HR Philipp and Ha Ehrenreich. Optical properties of semiconductors. *Physical Review*, 129(4):1550, 1963.

[119] Michael Schall and Peter Uhd Jepsen. Photoexcited gaas surfaces studied by transient terahertz time-domain spectroscopy. *Optics letters*, 25(1): 13–15, 2000.

[120] Bijay Sultanian. *Fluid Mechanics: An Intermediate Approach*. CRC Press, 2015.

[121] KL Gallaher and SH Bauer. On the thermochemical state of gaseous electron diffraction samples. *The Journal of Physical Chemistry*, 78(23): 2380–2389, 1974.

[122] Quang Shen and Kenneth Hedberg. Investigation of the equilibrium n2o4 2no2 by electron diffraction: Molecular structures and effective temperature and pressure of the expanding gas with implications for studies of other dimer- monomer equilibria. *The Journal of Physical Chemistry A*, 102(32):6470–6476, 1998.

[123] Robert H Nunn. *Intermediate fluid mechanics*. CRC Press, 1989.

[124] Richard Courant and Kurt Otto Friedrichs. *Supersonic flow and shock waves*, volume 21. Springer Science & Business Media, 1999.

[125] Ethirajan Rathakrishnan. *Applied gas dynamics*. John Wiley & Sons, 2010.

[126] AR Faruqi and HN Andrews. Cooled ccd camera with tapered fibre optics for electron microscopy. *Nuclear Instruments and Methods in Physics Research Section A: Accelerators, Spectrometers, Detectors and Associated Equipment*, 392(1-3):233–236, 1997.

[127] AR Faruqi, R Henderson, and S Subramaniam. Cooled ccd detector with tapered fibre optics for recording electron diffraction patterns. *Ultramicroscopy*, 75(4):235–250, 1999.

[128] AR Faruqi, HN Andrews, and R Henderson. A high sensitivity imaging detector for electron microscopy. *Nuclear Instruments and Methods in Physics Research Section A: Accelerators, Spectrometers, Detectors and Associated Equipment*, 367(1-3):408–412, 1995.

[129] AR Faruqi and Sriram Subramaniam. Ccd detectors in high-resolution biological electron microscopy. *Quarterly reviews of biophysics*, 33(1):1–27, 2000.

[130] Leon A Bosch. Dynamic uses of image intensifiers.

[131] Paul Hoess and Karlheinz Fleder. Time-integrated phosphor behavior in gated image intensifier tubes. In *International Symposium on Optical Science and Technology*, pages 23–28. International Society for Optics and Photonics, 2000.

[132] William E Flynt. Characterization of some common crt phosphors. In *33rd Annual Techincal Symposium*, pages 123–130. International Society for Optics and Photonics, 1990.

[133] AR Faruqi and GC Tyrell. Evaluation of gadolinium oxy-sulphide (p43) phosphor used in ccd detectors for electron microscopy. *Ultramicroscopy*, 76(1):69–75, 1999.

[134] Martin Nikl. Scintillation detectors for x-rays. *Measurement Science and Technology*, 17(4):R37, 2006.

[135] P-C Wang and GS Cargill III. Optimization of phosphor screens for charge coupled device based detectors and 7–34 kev x-rays. *Journal of applied physics*, 81(3):1031–1041, 1997.

[136] Glenn C Tyrrell. Phosphors and scintillators in radiation imaging detectors. *Nuclear Instruments and Methods in Physics Research Section A: Accelerators, Spectrometers, Detectors and Associated Equipment*, 546 (1):180–187, 2005.

[137] Gad Shani. *Radiation dosimetry instrumentation and methods.* CRC Press, 2000.

[138] Ford Kalil, WG Stone, HH Hubbell Jr, and RD Birkhoff. Stopping power of thin aluminum foils for 12 to 127 kev electrons. Technical report, Oak Ridge National Lab., Tenn., 1959.

[139] Anshu Saxena, Hemlata Singh, Priyanka Agrawal, SK Rathi, and AS Verma. Stopping power of electrons and positrons for c, al, cu, ag, au, pb, fe, u, ge, si and mo. *Applied Physics Research*, 2(2):176, 2010.

[140] G Hass and JE Waylonis. Optical constants and reflectance and transmittance of evaporated aluminum in the visible and ultraviolet. *JOSA*, 51(7):719–722, 1961.

[141] GW Ludwig and JS Prener. Evaluation of gd2o2s: Tb as a phosphor for the input screen of x-ray image intensifier. *IEEE Transactions on Nuclear Science*, 19(4):3–8, 1972.

[142] Hyotcherl Ihee, Boyd M Goodson, Ramesh Srinivasan, Vladimir A Lobastov, and Ahmed H Zewail. Ultrafast electron diffraction and structural dynamics: transient intermediates in the elimination reaction of c2f4i2. *The Journal of Physical Chemistry A*, 106(16):4087–4103, 2002.

[143] H Park, Z Hao, X Wang, S Nie, R Clinite, and J Cao. Synchronization of femtosecond laser and electron pulses with subpicosecond precision. *Review of scientific instruments*, 76(8):083905, 2005.

[144] Gy Farkas and Cs Toth. Energy spectrum of photoelectrons produced by picosecond laser-induced surface multiphoton photoeffect. *Physical Review A*, 41(7):4123, 1990.

[145] Gyozo Farkas, Csaba Toth, and Ambrus Kohazi-Kis. Above-threshold multiphoton photoelectric effect of a gold surface. *Optical Engineering*, 32 (10):2476–2480, 1993.

[146] S Varró and F Ehlotzky. High-order multiphoton ionization at metal surfaces by laser fields of moderate power. *Physical Review A*, 57(1):663, 1998.

APPENDIX A

Pulse delayer and stretcher circuit

In this appendix, we review the pulse delayer and extender device we constructed and introduced in section . Figure A.1 shows the block diagram of the device. The input signal is a 6μs TTL pulse coming from the laser Delay an Synchronization Unit. The output signal is a TTL pulse with a delay and duration adjusted by resistors R_1 and R_2, respectively. The signal flow in the circuit is shown in figure A.2.

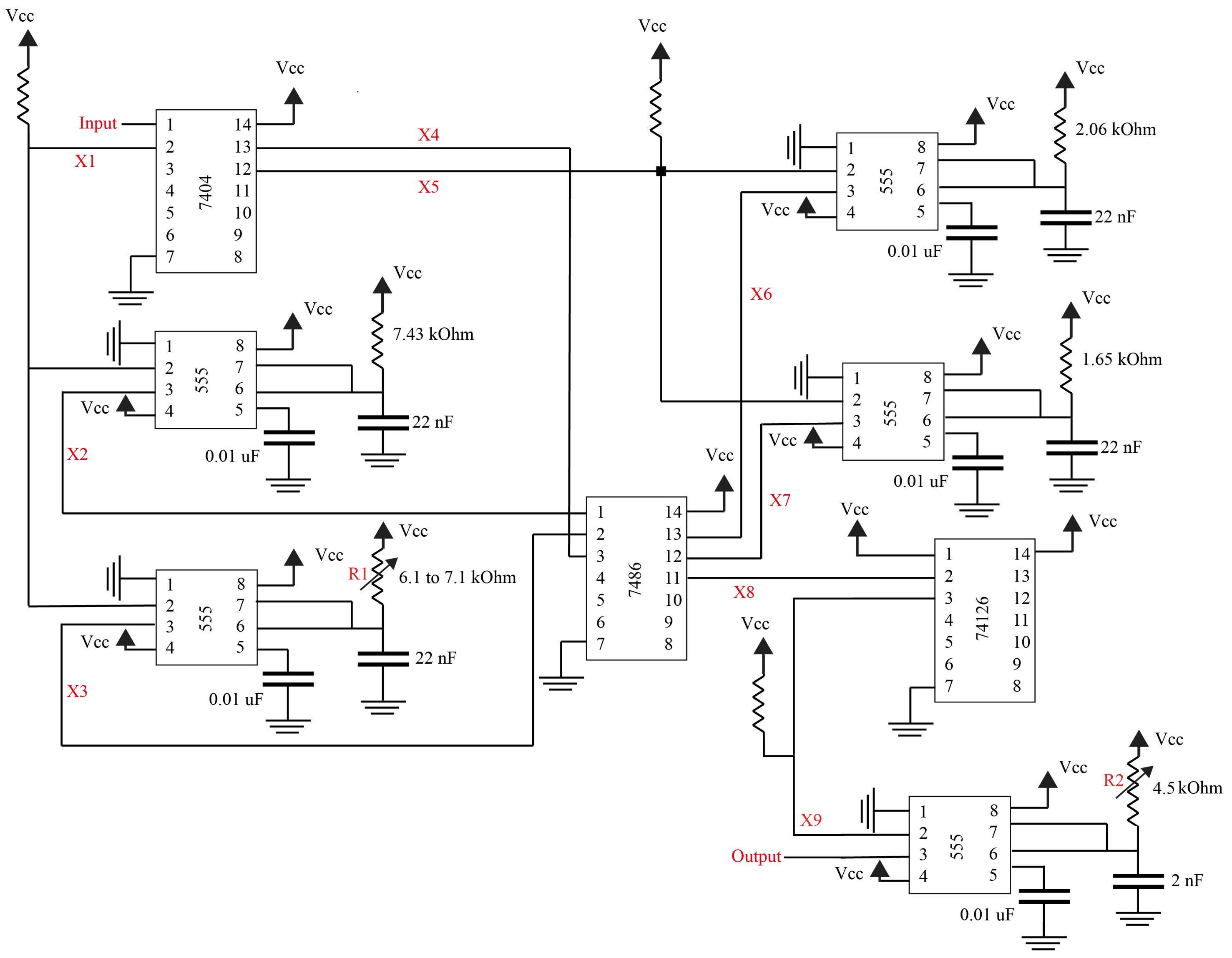

Figure A.1: Block diagram of the the delay generator and pulse stretcher.

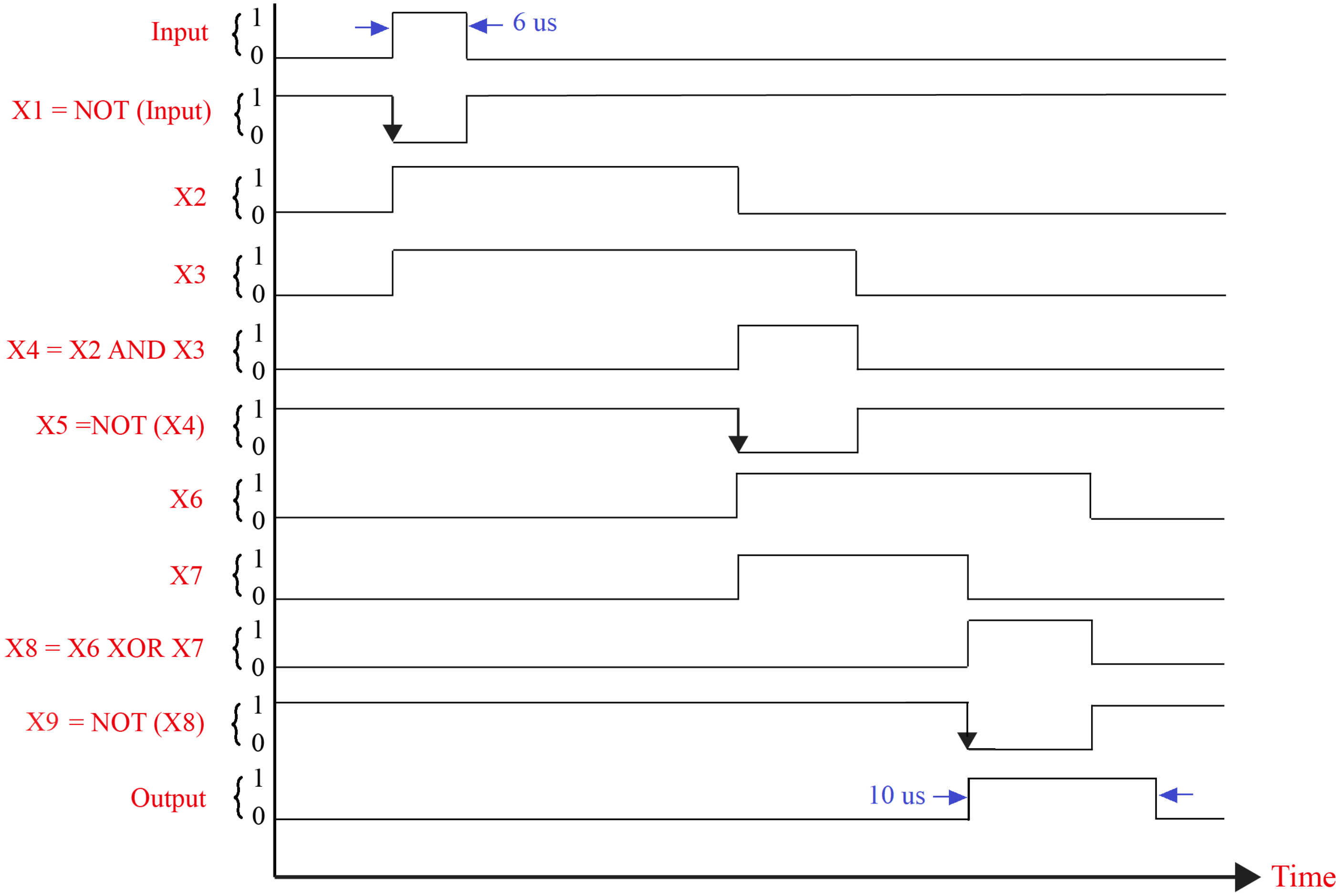

Figure A.2: Signal flow in the circuit in figure A.1.

APPENDIX B

Diffraction center and azimuthal average

The following Matlab code finds the center of diffraction pattern and then takes azimuthal average of the pattern by the method explained in section 4.4.1. The code divides the area around the beam block in four non-overlapping sectors as are shown by the numbers in Figure B.1. Then, it finds the intersection point (e.g. point C) for two lines drawn from two points (e.g. pixels A and B) in adjacent sectors, whose slopes are determined by the gradient of the image. This process is repeated for all of the points in the adjacent sectors. We obtain a set of intersection points and do a statistical analysis to pick up a point that is most likely the center of diffraction.

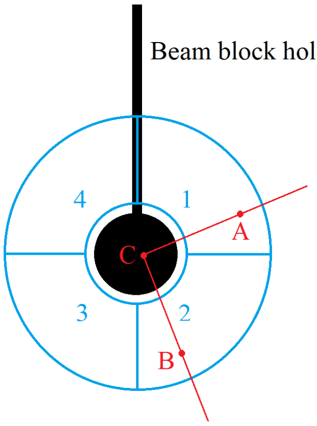

Figure B.1: Finding the center of the diffraction pattern by use of the image gradient. Two lines passing through points A and B, in two adjacent sectors, intersect at point C. The slopes of the lines are determined by the gradient of the image; therefore, point C should represent the center of diffraction.

```
% This function takes a diffraction pattern (Image)
% and the center of the beamblock (bBlock_cent) as an array and the
% beam block radius. None of these values need to be accurate.
% It returns the center of the diffractio pattern (where the center
% of the electron beam would be on the detector). It also returns
% the azimuthal average of the beam.

function  [Cxx, Cyy, AzAve] = BeamCenter(Image,bBlock_cent,bBlock_r)
J = Image;

% Apply one or more of the following filters to smooth
% the diffraction pattern:
h = ones(5,5) / 25;
J = imfilter(J,h);
J = medfilt2(J, [5 5]);
J = wiener2(J,[5 5]);

% Calculate the image gradient
[Gx,Gy] = imgradientxy(J,'prewitt');


Cx=round(bBlock_cent(2));
Cy=round(bBlock_cent(1));
r = round(bBlock_r)+1;

clear n1 m1 n2 m2

saveXBeam = [];
saveYBeam = [];

% Divide the diffraction pattern into four areas around the
% beam block. Find the the center from the intersection of
% mutually orthogonal lines.
% Below, delta is the radius range around the beam block where
% the calculations take place. The user may change this range.
for delta = 20:40
    % #1 right bottom and top
    for n1 = Cx:1:Cx+r+delta
        m1 = Cy+round(sqrt((r+delta)^2-(n1-Cx).^2));
        %         J(n1,m1) = 10;
        n2 = n1-(r+delta);
        m2 = Cy+round(sqrt((r+delta)^2-(n2-Cx).^2));
        %         J(n2,m2) = -10;

        x_beam1(n1-Cx+1) = (m2-m1+Gx(n1,m1)/Gy(n1,m1)*...
            n1-Gx(n2,m2)/Gy(n2,m2)*n2)/(Gx(n1,m1)/...
            Gy(n1,m1)-Gx(n2,m2)/Gy(n2,m2));
        y_beam1(n1-Cx+1) = m1+Gx(n1,m1)/Gy(n1,m1)*...
            (x_beam1(n1-Cx+1)-n1);

    end
    x_beam1(isnan(x_beam1)) = [];
    y_beam1(isnan(y_beam1)) = [];


    clear n1 m1 n2 m2
    % #2 Left Bottom and top
```

```
for n1 = Cx:1:Cx+r+delta
    m1 = Cy-round(sqrt((r+delta)^2-(n1-Cx).^2));
    %             J(n1,m1) = 1;
    n2 = n1-(r+delta);
    m2 = Cy-round(sqrt((r+delta)^2-(n2-Cx).^2));
    %             J(n2,m2) = -1;
    x_beam2(n1-Cx+1) = (m2-m1+Gx(n1,m1)/Gy(n1,m1)*...
        n1-Gx(n2,m2)/Gy(n2,m2)*n2)/(Gx(n1,m1)...
        /Gy(n1,m1)-Gx(n2,m2)/Gy(n2,m2));
    y_beam2(n1-Cx+1) = m1+Gx(n1,m1)/Gy(n1,m1)*...
        (x_beam2(n1-Cx+1)-n1);


end
x_beam2(isnan(x_beam2)) = [];
y_beam2(isnan(y_beam2)) = [];

clear n1 m1 n2 m2
% #3 Top right and left
for n1 = Cx-r-delta:1:Cx
    m1 = Cy+round(sqrt((r+delta)^2-(n1-Cx).^2));
    %         J(n1,m1) = 3;
    n2 = -n1+2*Cx-(r+delta);
    m2 = Cy-round(sqrt((r+delta)^2-(n2-Cx).^2));
    %         J(n2,m2) = -3;
    x_beam3(n1-(Cx-r-delta)+1) = (m2-m1+Gx(n1,m1)/...
        Gy(n1,m1)*n1-Gx(n2,m2)/Gy(n2,m2)*n2)/...
        (Gx(n1,m1)/Gy(n1,m1)-Gx(n2,m2)/Gy(n2,m2));
    y_beam3(n1-(Cx-r-delta)+1) = m1+Gx(n1,m1)/Gy(n1,m1)*...
        (x_beam3(n1-(Cx-r-delta)+1)-n1);

end
x_beam3(isnan(x_beam3)) = [];
y_beam3(isnan(y_beam3)) = [];

clear n1 m1 n2 m2
%
% #4 Bottom right and top left
for n1 = Cx:1:Cx+r+delta
    m1 = Cy+round(sqrt((r+delta)^2-(n1-Cx).^2));
    %         I(n1,m1) = 10;
    n2 = n1-(r+delta);
    m2 = Cy-round(sqrt((r+delta)^2-(n2-Cx).^2));
    %         I(n2,m2) = -10;
    x_beam4(n1-Cx+1) = (m2-m1+Gx(n1,m1)/Gy(n1,m1)*n1-...
        Gx(n2,m2)/Gy(n2,m2)*n2)/(Gx(n1,m1)/Gy(n1,m1)-...
        Gx(n2,m2)/Gy(n2,m2));
    y_beam4(n1-Cx+1) = m1+Gx(n1,m1)/Gy(n1,m1)*...
        (x_beam4(n1-Cx+1)-n1);

end
x_beam4(isnan(x_beam4)) = [];
y_beam4(isnan(y_beam4)) = [];
clear n1 m1 n2 m2
% #5 Bottom left and top right
for n1 = Cx:1:Cx+r+delta
    m1 = Cy-round(sqrt((r+delta)^2-(n1-Cx).^2));
```

```
        %          I(n1,m1) = 10;
        n2 = n1-(r+delta);
        m2 = Cy+round(sqrt((r+delta)^2-(n2-Cx).^2));
        %          I(n2,m2) = -10;
        x_beam5(n1-Cx+1) = (m2-m1+Gx(n1,m1)/Gy(n1,m1)*...
            n1-Gx(n2,m2)/Gy(n2,m2)*n2)/(Gx(n1,m1)/...
            Gy(n1,m1)-Gx(n2,m2)/Gy(n2,m2));
        y_beam5(n1-Cx+1) = m1+Gx(n1,m1)/Gy(n1,m1)*...
            (x_beam5(n1-Cx+1)-n1);

    end
    x_beam5(isnan(x_beam5)) = [];
    y_beam5(isnan(y_beam5)) = [];
    %
    clear n1 m1 n2 m2
    % #6 Bottom right and left
    for n1 = Cx:1:Cx+r+delta
        m1 = Cy+round(sqrt((r+delta)^2-(n1-Cx).^2));
        %      I(n1,m1) = 10;
        n2 = 2*Cx-(n1-(r+delta));
        m2 = Cy-round(sqrt((r+delta)^2-(Cx-n2).^2));
        %      I(n2,m2) = -10;

        x_beam6(n1-Cx+1) = (m2-m1+Gx(n1,m1)/Gy(n1,m1)*...
            n1-Gx(n2,m2)/Gy(n2,m2)*n2)/(Gx(n1,m1)/...
            Gy(n1,m1)-Gx(n2,m2)/Gy(n2,m2));
        y_beam6(n1-Cx+1) = m1+Gx(n1,m1)/Gy(n1,m1)*...
            (x_beam6(n1-Cx+1)-n1);

    end
    x_beam6(isnan(x_beam6)) = [];
    y_beam6(isnan(y_beam6)) = [];

    %
    x_beam = [x_beam1 x_beam2 x_beam3 x_beam4 x_beam5 x_beam6];
    y_beam = [y_beam1 y_beam2 y_beam3 y_beam4 y_beam5 y_beam6];
    %% Remove Outliers
    x1 = quantile(x_beam,0.25);
    x3 = quantile(x_beam,0.75);
    range_x = x3-x1;
    lower_limit_x = x1-1.5*range_x;
    upper_limit_x = x3+1.5*range_x;
    x_beam(x_beam > upper_limit_x) = [];
    x_beam(x_beam < lower_limit_x) = [];

    y1 = quantile(y_beam,0.25);
    y3 = quantile(y_beam,0.75);
    range_y = y3-y1;
    lower_limit_y = y1-1.5*range_y;
    upper_limit_y = y3+1.5*range_y;
    y_beam(y_beam > upper_limit_y) = [];
    y_beam(y_beam < lower_limit_y) = [];
    %%

    saveXBeam = [saveXBeam, x_beam];
    saveYBeam = [saveYBeam, y_beam];
end
```

```
%%%%%%%%%%%%%%%%%%%%%%%%%%%%%%%%%
%%%%%%%%%%%%%%%%%%%%%%%%%%%%%%%%%
% The diffraction center is at
Cx=round(mean(saveXBeam));
Cy=round(mean(saveYBeam));
% We use these values to repeat the diffraction center
% finding as a new initial point.
clear n1 m1 n2 m2 delta

saveXBeam = [];
saveYBeam = [];

% Divide the diffraction pattern into four areas around
% the beam block. Find the the center from the intersection
% of mutually orthogonal lines.
for delta = 1:20
    % #1 right bottom and top
    for n1 = Cx:1:Cx+r+delta
        m1 = Cy+round(sqrt((r+delta)^2-(n1-Cx).^2));
        %         J(n1,m1) = 10;
        n2 = n1-(r+delta);
        m2 = Cy+round(sqrt((r+delta)^2-(n2-Cx).^2));
        %         J(n2,m2) = -10;

        x_beam1(n1-Cx+1) = (m2-m1+Gx(n1,m1)/Gy(n1,m1)...
            *n1-Gx(n2,m2)/Gy(n2,m2)*n2)/(Gx(n1,m1)...
            /Gy(n1,m1)-Gx(n2,m2)/Gy(n2,m2));
        y_beam1(n1-Cx+1) = m1+Gx(n1,m1)/Gy(n1,m1)*...
            (x_beam1(n1-Cx+1)-n1);

    end
    x_beam1(isnan(x_beam1)) = [];
    y_beam1(isnan(y_beam1)) = [];


    clear n1 m1 n2 m2
    % #2 Left Bottom and top
    for n1 = Cx:1:Cx+r+delta
        m1 = Cy-round(sqrt((r+delta)^2-(n1-Cx).^2));
        %             J(n1,m1) = 1;
        n2 = n1-(r+delta);
        m2 = Cy-round(sqrt((r+delta)^2-(n2-Cx).^2));
        %             J(n2,m2) = -1;
        x_beam2(n1-Cx+1) = (m2-m1+Gx(n1,m1)/Gy(n1,m1)*...
            n1-Gx(n2,m2)/Gy(n2,m2)*n2)/(Gx(n1,m1)/...
            Gy(n1,m1)-Gx(n2,m2)/Gy(n2,m2));
        y_beam2(n1-Cx+1) = m1+Gx(n1,m1)/Gy(n1,m1)*...
            (x_beam2(n1-Cx+1)-n1);


    end
    x_beam2(isnan(x_beam2)) = [];
    y_beam2(isnan(y_beam2)) = [];

    clear n1 m1 n2 m2
    % #3 Top right and left
```

```
for n1 = Cx-r-delta:1:Cx
    m1 = Cy+round(sqrt((r+delta)^2-(n1-Cx).^2));
    %         J(n1,m1) = 3;
    n2 = -n1+2*Cx-(r+delta);
    m2 = Cy-round(sqrt((r+delta)^2-(n2-Cx).^2));
    %         J(n2,m2) = -3;
    x_beam3(n1-(Cx-r-delta)+1) = (m2-m1+Gx(n1,m1)/Gy(n1,m1)...
        *n1-Gx(n2,m2)/Gy(n2,m2)*n2)/(Gx(n1,m1)/Gy(n1,m1)...
        -Gx(n2,m2)/Gy(n2,m2));
    y_beam3(n1-(Cx-r-delta)+1) = m1+Gx(n1,m1)/Gy(n1,m1)...
        *(x_beam3(n1-(Cx-r-delta)+1)-n1);

end
x_beam3(isnan(x_beam3)) = [];
y_beam3(isnan(y_beam3)) = [];

clear n1 m1 n2 m2
%
% #4 Bottom right and top left
for n1 = Cx:1:Cx+r+delta
    m1 = Cy+round(sqrt((r+delta)^2-(n1-Cx).^2));
    %         I(n1,m1) = 10;
    n2 = n1-(r+delta);
    m2 = Cy-round(sqrt((r+delta)^2-(n2-Cx).^2));
    %         I(n2,m2) = -10;
    x_beam4(n1-Cx+1) = (m2-m1+Gx(n1,m1)/Gy(n1,m1)...
        *n1-Gx(n2,m2)/Gy(n2,m2)*n2)/(Gx(n1,m1)...
        /Gy(n1,m1)-Gx(n2,m2)/Gy(n2,m2));
    y_beam4(n1-Cx+1) = m1+Gx(n1,m1)/Gy(n1,m1)*...
        (x_beam4(n1-Cx+1)-n1);

end
x_beam4(isnan(x_beam4)) = [];
y_beam4(isnan(y_beam4)) = [];
clear n1 m1 n2 m2
% #5 Bottom left and top right
for n1 = Cx:1:Cx+r+delta
    m1 = Cy-round(sqrt((r+delta)^2-(n1-Cx).^2));
    %         I(n1,m1) = 10;
    n2 = n1-(r+delta);
    m2 = Cy+round(sqrt((r+delta)^2-(n2-Cx).^2));
    %         I(n2,m2) = -10;
    x_beam5(n1-Cx+1) = (m2-m1+Gx(n1,m1)/Gy(n1,m1)...
        *n1-Gx(n2,m2)/Gy(n2,m2)*n2)/(Gx(n1,m1)/...
        Gy(n1,m1)-Gx(n2,m2)/Gy(n2,m2));
    y_beam5(n1-Cx+1) = m1+Gx(n1,m1)/Gy(n1,m1)...
        *(x_beam5(n1-Cx+1)-n1);

end
x_beam5(isnan(x_beam5)) = [];
y_beam5(isnan(y_beam5)) = [];
%
clear n1 m1 n2 m2
% #6 Bottom right and left
for n1 = Cx:1:Cx+r+delta
    m1 = Cy+round(sqrt((r+delta)^2-(n1-Cx).^2));
    %     I(n1,m1) = 10;
```

```
        n2 = 2*Cx-(n1-(r+delta));
        m2 = Cy-round(sqrt((r+delta)^2-(Cx-n2).^2));
        %     I(n2,m2) = -10;

        x_beam6(n1-Cx+1) = (m2-m1+Gx(n1,m1)/Gy(n1,m1)*...
            n1-Gx(n2,m2)/Gy(n2,m2)*n2)/(Gx(n1,m1)/...
            Gy(n1,m1)-Gx(n2,m2)/Gy(n2,m2));
        y_beam6(n1-Cx+1) = m1+Gx(n1,m1)/Gy(n1,m1)*...
            (x_beam6(n1-Cx+1)-n1);

    end
    x_beam6(isnan(x_beam6)) = [];
    y_beam6(isnan(y_beam6)) = [];

    %
    x_beam = [x_beam1 x_beam2 x_beam3 x_beam4 x_beam5 x_beam6];
    y_beam = [y_beam1 y_beam2 y_beam3 y_beam4 y_beam5 y_beam6];
    %% Remove Outliers
    x1 = quantile(x_beam,0.25);
    x3 = quantile(x_beam,0.75);
    range_x = x3-x1;
    lower_limit_x = x1-1.5*range_x;
    upper_limit_x = x3+1.5*range_x;
    x_beam(x_beam > upper_limit_x) = [];
    x_beam(x_beam < lower_limit_x) = [];

    y1 = quantile(y_beam,0.25);
    y3 = quantile(y_beam,0.75);
    range_y = y3-y1;
    lower_limit_y = y1-1.5*range_y;
    upper_limit_y = y3+1.5*range_y;
    y_beam(y_beam > upper_limit_y) = [];
    y_beam(y_beam < lower_limit_y) = [];
    %%

    saveXBeam = [saveXBeam, x_beam];
    saveYBeam = [saveYBeam, y_beam];
end
% Display the output
disp(['The beam center is at (',num2str(round(mean(saveXBeam))),...
    setstr(177),num2str(std(saveXBeam)/sqrt(length(saveXBeam)))...
    ,',',num2str(round(mean(saveYBeam))),setstr(177)...
    ,num2str(std(saveYBeam)/sqrt(length(saveYBeam))),')'])

 Cxx = mean(saveXBeam);
 Cyy = mean(saveYBeam);
figure
imagesc(J)
figure
subplot(2,1,1)
histogram(saveXBeam);
histfit(saveXBeam,50,'Normal');
xlabel('pixels')
ylabel('Distribution of found peaks in x')

subplot(2,1,2)
histogram(saveYBeam);
```

```
histfit(saveYBeam,50,'Normal');
xlabel('pixels')
ylabel('Distribution of found peaks in y')

%%%%%%%%%%%%%%%%%%%%%%%%%%%%%%%%%%%%%%
%%%%%%%%%%%%%%%%%%%%%%%%%%%%%%%%%%%%%%

%Azimuthal average
Dim = size(Image);

x = 1:Dim(1);
y = 1:Dim(2);
[X,Y] = meshgrid (x,y);

% Distance function:
d = sqrt((X'-Cxx).^2+(Y'-Cyy).^2);
% Flatten the distance function and the image:
d_Linear = round(d(:));
Im_Linear = Image(:);
for n = min(d_Linear)+1:max(d_Linear)+1
    R = Im_Linear(d_Linear == n-1);
    %% Remove Outliers
    x1 = quantile(R,0.4);
    x3 = quantile(R,0.6);
    range_x = x3-x1;
    lower_limit_x = x1-1.5*range_x;
    upper_limit_x = x3+1.5*range_x;
    R(R > upper_limit_x) = [];
    R(R < lower_limit_x) = [];
    AzAve(n) = mean(R);
end
figure;plot(AzAve)
end
```